INFORMATION TO USERS

This manuscript has been reproduced from the microfilm master. UMI films the text directly from the original or copy submitted. Thus, some thesis and dissertation copies are in typewriter face, while others may be from any type of computer printer.

The quality of this reproduction is dependent upon the quality of the copy submitted. Broken or indistinct print, colored or poor quality illustrations and photographs, print bleedthrough, substandard margins, and improper alignment can adversely affect reproduction.

In the unlikely event that the author did not send UMI a complete manuscript and there are missing pages, these will be noted. Also, if unauthorized copyright material had to be removed, a note will indicate the deletion.

Oversize materials (e.g., maps, drawings, charts) are reproduced by sectioning the original, beginning at the upper left-hand corner and continuing from left to right in equal sections with small overlaps. Each original is also photographed in one exposure and is included in reduced form at the back of the book.

Photographs included in the original manuscript have been reproduced xerographically in this copy. Higher quality 6" x 9" black and white photographic prints are available for any photographs or illustrations appearing in this copy for an additional charge. Contact UMI directly to order.

WAVE SCATTERING AND DIFFRACTION TOMOGRAPHY IN COMPLEX MEDIA

A DISSERTATION

SUBMITTED TO THE DEPARTMENT OF GEOPHYSICS

AND THE COMMITTEE ON GRADUATE STUDIES

OF STANFORD UNIVERSITY

IN PARTIAL FULFILLMENT OF THE REQUIREMENTS

FOR THE DEGREE OF

DOCTOR OF PHILOSOPHY

By

Guan Yong Wang

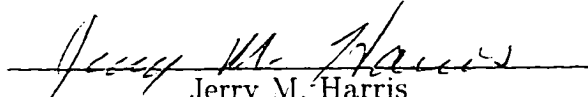August, 1997

UMI Number: 9810226
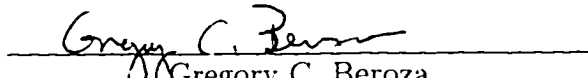
UMI

300 North Zeeb Road
Ann Arbor, MI 48103

ii

I certify that I have read this dissertation and that in my opinion it is fully adequate, in scope and in quality, as a dissertation for the degree of Doctor of Philosophy.

Jerry M. Harris
(Principal Advisor)

I certify that I have read this dissertation and that in my opinion it is fully adequate, in scope and in quality, as a dissertation for the degree of Doctor of Philosophy.

Gregory C. Beroza

I certify that I have read this dissertation and that in my opinion it is fully adequate, in scope and in quality, as a dissertation for the degree of Doctor of Philosophy.

Jon F. Claerbout
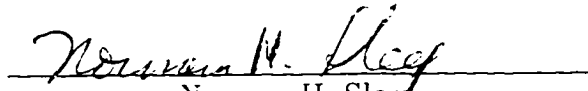
I certify that I have read this dissertation and that in my opinion it is fully adequate, in scope and in quality, as a dissertation for the degree of Doctor of Philosophy.

Norman H. Sleep

Approved for the University Committee on Graduate Studies:

Thomas Wasow

iii

Abstract

The essential part of "reservoir geophysics" is to be able to obtain high resolution images of small scale structures in a heterogeneous medium. Diffraction tomography has a resolution comparable to the wavelength and has been studied extensively within the first Born or Rytov approximations. These approximations linearized the problem and lend to the computational advantages of the Fourier transformation. Computational efficiency and algorithmic simplicity, however, are accompanied by limitations on the ranges of validity for these methods. The objective of this study is to develop tomographic inversion algorithms that preserve the efficiency and simplicity of the linear approximations but have less limitation in real applications where media are not just slightly inhomogeneous. By expressing the scattering equations in operator forms, an array of inversion methods are derived. The essence of these methods is renormalization or rescaling, i.e. the effects of strong and multiple scattering are taken into account by modifying or rescaling the primary wave field.

The developed methods can be classified as renormalizations in the spatial domain, wavenumber domain, and wave asymptotic domain where spatial and wavenumber domains are superimposed. The spatial domain renormalization technique is used to effectively sum the divergent terms of the Born-Neumann expansion and to decompose the original nonlinear problem into two cascaded linear problems. The Wavenumber domain renormalization is used to obtain individual diffraction projections independently by wavefield backpropagation; the inverse problem is then solved by assembling the individual projections and performing inverse Fourier transform. With the wave asymptotic renormalization, the rescaled scattered field is related to the spectrum of the inhomogeneity function via the asymptotic Fourier transform.

iv

When the distribution of the small scale inhomogeneities is too complicated to resolve, they may be treated as random. Beyond the conventional approaches of the effective medium, the full wave representation in random media is used to invert second order statistical properties of the medium. The estimated statistical quantities may be used to identify, for example, fracture scales and orientations, or to facilitate other reservoir simulation modalities.

Acknowledgments

I would like to thank the students, faculty and sponsors of Stanford's Seismic Tomography Project who contributed in various ways to the work presented in this thesis.

I thank my advisor Jerry M. Harris for providing stimulating research and exceptional educational environments and for the encouragement he always gives to me. From him I have had the opportunity to learn about the theory of wave and fields. Jerry has influenced every aspect of this thesis, both in spirit and in content and many of his ideas appear within it.

I thank Jesse Costa for enlightening discussions on many subjects, particularly for his explorations into Maslov ray theory. The conversations between us not only were on science but life as a whole.

I thank Dimitri Bevc for being a great friend who was always available when I needed help and advice. Thanks go to Ann Wiley, Leiwei Mo, Mark Van Shaack, Nicholas Smalley, Ricardo Castellani and Youli Quan, who have been great fellow students. Their friendship and help made my study at Stanford an enjoyable experience. Also thanks to Claudia Magalhaes for her help and enthusiasm in sharing research ideas.

I would like to thank Greg Beroza, Jon Claerbout, George Papanicolaou and Norman Sleep for reading this thesis.

Finally, the years at Stanford wouldn't have enriched my life as much as they did without the love, encouragement and patience of my family. Their understanding and support gave me the strength to complete this work.

Contents

vii

List of Figures

x

xi

xii

Chapter 1

Introduction

The subject of this thesis is to understand how the complexity of the earth's subsurface is transferred to the scattered acoustic wavefield and, vice versa, whether the recorded scattered wavefield is capable of describing the medium's heterogeneity. Given the variety of scales and strong inhomogeneity of the earth's medium encountered in geophysics, I believe it is necessary to use efficient approximations to study wave phenomena. For inverse scattering problems the approximate methods are especially appropriate.

Wave scattering problems deal with the phenomena that occur when a specified wave, assuming a source whose field "when isolated" is known, interacts with the scatterers or the inhomogeneities of finite dimensions in a medium. As one illustration, an electromagnetic "primary wave" induces charges and currents in the objects, and these generate the "secondary waves" that constitute the scattered field. The scattered field includes the waves reflected by the illuminated side of the objects, the waves which cancel the incident field in the shadow zone, as well as the waves diffracted into the shadow zone. It is convenient to express the total field as a sum of incident and scattered fields in order to obtain the integral representation which is essential in inverse scattering problems. Because a background medium and heterogeneity relative to the background are involved, scattering theory can be viewed as a branch of perturbation theory.

Inverse scattering poses the problem the other way around. It determines the

1

sources of the scattered fields or medium properties by analyzing the measured scattered field, i.e., the transmissions, reflections and diffractions of a probing wave propagating through the media. The inverse scattering problem has a wide range of applications in geophysics and other imaging sciences.

1.1   Goal of the thesis

Given the variety of scales and strong inhomogeneity of the earth's medium, traveltime tomography, diffraction tomography, and well-logs are combined to image the subsurface. Traveltime tomography is used to image the large scale inhomogeneity while diffraction tomography is used to the intermediate scale inhomogeneity with traveltime tomgrams as background. For the scales too fine to image using tomography, their statistical properties are estimated and the well log is used to condition the probability distribution. Figure 1.1 illustrates the scales of the above mentioned methods.

In its common form the inverse scattering problem, or diffraction tomography, is formulated as an inversion of the Helmholtz equation with a spatially varying coefficient. Solutions to inverse scattering problems are often mathematically intractable. The techniques for constructing solutions of inverse scattering problems have been studied with linear approximations, such as Born[1] or Rytov solutions. These techniques substantially simplify the inversion problem and lend themselves to the computational advantages of the fast Fourier transformation. Computational efficiency and algorithmic simplicity, however, are accompanied by limitations on the ranges

---

[1] Max Born was born in Breslau in 1882 into a Polish Jewish family. He worked in the Physics Department at Gottingen University and later became its Director. Despite his pacifism, chronic asthma and bronchial problems, he was required to serve in the German army on no fewer than 3 occasions. He prudently left Germany for Cambridge in 1933 in order to avoid the Nazi scourge. Following this, he spent a time at Bangalore University prior to settling in Edinburgh as Tait Professor of Natural Philosophy. He retired to a German spa town in 1953 shortly before receiving the Nobel Prize for fundamental work on Quantum mechanics and for his statistical interpretation of the wave function. Born also introduced a useful technique, known as the Born approximation, for solving problems concerning the scattering of atomic particles. His tombstone bears the gnomic inscription $pq - qp = ih/2\pi$ (Encyclopedia Britannica, Internet edition, 1997).
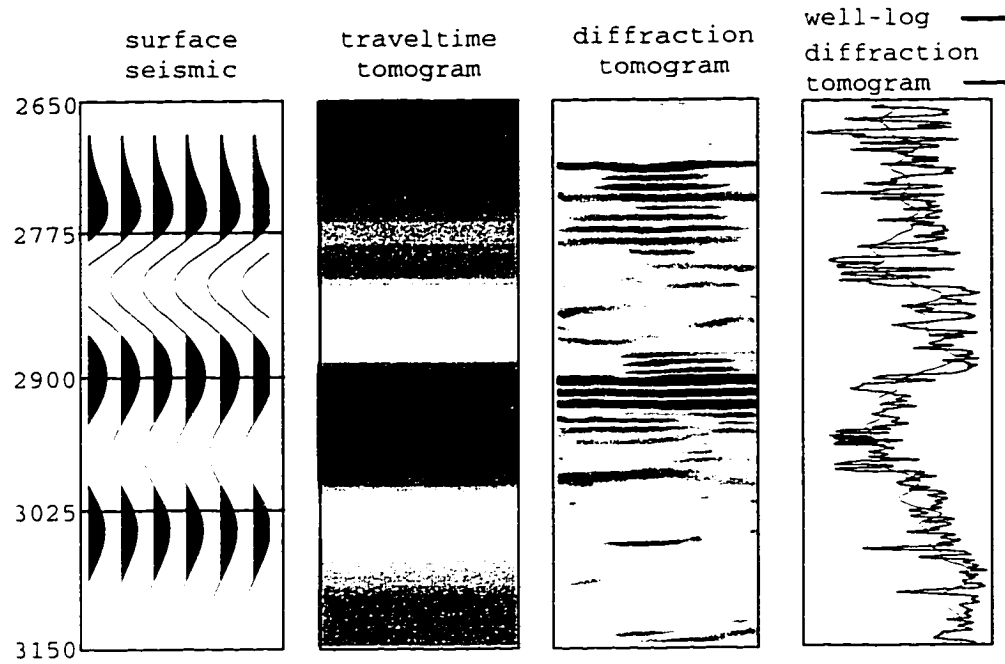
Figure 1.1: Multi scales imaging of the earth's medium: The left panel is the seismic profile corresponding to the area of the crosswell imaging; the middle left panel is a traveltime tomogram; the middle right panel a diffraction tomogram; and the right panel is the well-log and a profile from the diffraction tomogram.

of validity for these methods. since they may not provide sufficiently accurate representations of the underlying physics. The goal in this thesis is to develop diffraction tomographic inversion algorithms that preserve the efficiency and simplicity of conventional diffraction tomography. but have fewer limitations in real applications where media are not just slightly inhomogeneous. By expressing the scattering equations into operator forms. new insight into the inversion problem is obtained. This leads to various approximations to the scattering operators. resulting in an array of inversion methods.

It has become a fundamental task. in geophysical exploration. to predict and monitor the fluid flow in the subsurface. The techniques developed in this thesis can be used to image fine scale structures in the subsurface with a higher degree of resolution and accuracy which are impossible to achieve using traditional methods. While the algorithms are formulated for seismic (scalar and tensor) waves. they are

equally applicable to electromagnetic waves. This is significant, since electromagnetic methods are becoming progressively popular in the characterization subsurface fluids as more sophisticated instruments are developed.

1.2 Previous work

The work of Mueller et al. (1979) was responsible for focusing the interest of many researchers on diffraction tomography, although the technique can be traced back to the classic paper by Wolf (1969). Diffraction tomography was introduced to geophysical application by Devaney (1984), and reformulated for cylindrical incident waves by Harris (1987) and Wu et al. (1987). In the early treatment of diffraction tomography, Born and Rytov approximations were applied for constant background media. The inversion algorithms were based on the so-called generalized projection-slice theorem that holds within these approximations (Muller, et. al., 1979; Devaney, 1982, 1985, 1986). The spectrum of heterogeneity can be related to the measurement of the acoustic field scattered from it by the Fourier [2] transform. Its application is successful only if the scattering is weak, e.g., the heterogeneities are small deviations from the background or if the correlation lengths of the deviations are small compared to a wavelength. The small perturbation approximations that are used for developing the diffraction tomography algorithms have been discussed, e.g., by Ishimaru (1978).

A discussion of the theories of the Born and the Rytov approximations was presented by Chernov (1960). A comparison of Born and Rytov approximations is presented in Kak and Slaney (1988). The issues relating to uniqueness and stability of inverse scattering solutions are addressed in Backus and Gilbert (1968) and Devaney (1989). The mathematics of solving integral equations for inverse scattering problems is described in Colton (1983).

---

[2]Joseph Fourier was born in 1768 and became a personal friend of Napoleon Bonaparte, accompanying him on his invasion of Egypt in 1788. The desert heat made a lasting impression on Fourier, who believed it to be the ideal climate. Consequently, he swaddled himself in thick clothing and worked in over-heated rooms. The series which bears his name was formulated in connection with his studies of heat conduction in 1822. He died in 1830 (Encyclopedia Britannica, Internet edition, 1997).

The filtered back-propagation algorithm for diffraction tomography was first advanced by Devaney (1982). More recently, Kak and Slaney (1987) showed that by using frequency domain interpolation followed by direct Fourier inversion, reconstructions of quality comparable to that produced by the filtered back-propagation algorithm can be obtained. Interpolation based algorithms were first studied by Mueller et al., (1979). An extensive review is given by Kak and Slaney (1987).

Due to the limitations of conventional diffraction tomography, recent works have attempted to extend the applicability and interpretation of these methods to include stronger scattering effects. One approach bases reconstruction algorithms on the distorted wave Born and Rytov approximations, in which it is assumed that a prior estimate for all but a weakly scattered component of the heterogeneity is available, for example, for small heterogeneities of velocities superimposed on large 1D stratified variation. Various signal processing scenarios based on a layered background model have been extensively studied. One such method uses slant stacks to pre-process and map tomographic data with a layered background into an equivalent constant reference background data set, and then applies the conventional diffraction tomography algorithm to the pre-processed data (Devaney and Zhang, 1991). Another applies a WKBJ solution for the Green's [3] function to simplify propagation, thereby extending the constant background back-propagation algorithm to smooth background variations (Huan and Wu, 1992; Williamson, 1993). Yet another decomposes the wave fields of the layered host medium into vertical eigenstates and numerically reformulates the problem (Pai, 1990; Dickens, 1994; Harris and Wang, 1996). These

---

[3]George Green was born near Nottingham in 1793 and is a remarkable example of being a self-taught mathematician. After attending school for one year, he left at the age of nine to work in his father's bakery and later became a miller. No firm details about his education or development exist until he reached the age of 35, when he published (at his own expense) 'An Essay on the Application of Mathematical Analysis to the Theories of Electricity and Magnetism'. This remarkable work introduced the theorems bearing Green's name, the technique of using Green's functions to solve nonhomogeneous boundary value problems, and also established the concept of the 'potential' in electricity and magnetism. At the age of 40, he went to Cambridge to obtain a formal mathematical training, later to become a Fellow of Caius College. Despite siring 7 children, he never married the mother, possibly to enable his election to a Fellowship at Caius (which required the recipient to be celibate). Green died of influenza at his mill in Nottingham in 1841 (Encyclopedia Britannica, Internet edition, 1997).

algorithms offer different approaches either in data space or model space and indicate that more and more effort is being made to utilize diffraction tomography in practical applications.

Besides the linearized approaches, there are also well developed nonlinear methods to the solution of the inverse scattering problem. Iterative diffraction tomography methods which calculate the higher order terms in the Born series (Vainberg, 1988) and the nonlinear solver using base functions (Chew, 1990, Thompson, 1994) are examples. Although those nonlinear methods have not entered geophysical application in a wide sense, a generalized least-square method is gaining popularity for surface seismic data (Tarantola, 1984). However, the application of these nonlinear methods to practical problems requires extremely intensive computation, which is not yet practical for real problems.

1.3   Organization

The mathematical methods used to solve inverse scattering problems can be classified according to the frequency of the wave and the scale of the detectable inhomogeneity. The parameter ka distinguishes different theoretical regimes, where k is the wavenumber and a is a characteristic dimension of the scatterer. The so-called Rayleigh[4] scattering and high frequency scattering correspond to the regime where $ka << 1$ and $ka >> 1$. These two regimes allow approximations to be made which render the inversion of the scattered field more tractable. For the case of $ka << 1$, one can make assumptions about the nature of the field within the inhomogeneous region, e.g. that the scattering is weak and the phase of the field inside the scattering medium is not too different from what would occur if no scatterer were present. When $ka >> 1$ one can adopt wave asymptotics, or ray-like models. The reconstruction methods developed in this thesis follow this classification and are presented in the

---

[4]John William Stutt, 3rd. Lord Rayleigh was born in 1842. He became a student of Routh at Cambridge, but after studying at university he returned to his country estate to perform experiments and formulate theories. Among these were his explanation of why the sky is blue and the discovery of the gas Argon, for which he won the Nobel Prize for physics in 1904 (Encyclopedia Britannica, Internet edition, 1997).

four subsequent chapters.

1.3.1 Wave scattering operators, imaging, and resolution

Following this introduction, Chapter 2 briefly describes the mathematics of the scattering theory and defines the symbols and terminology used throughout the thesis. The scattering integral equations are expressed into operator forms. These scattering operators can be formally analyzed and lead to various nonlinear approximations and an array of tomographic inversion methods for complex media. The equations describing the resolving power of the resultant inverse operators are formulated. and the analysis is consistent with the assessment that diffraction tomography has a resolution comparable to the wavelength of the probing wavefield (transmission tomography has a resolution comparable to the Fresnel [5] zone).

1.3.2 Inversion of strong scattering using renormalizations

To extend the first Born approximation in real space, Chapter 3 utilizes the fact that the dominant contribution to the scattering integral comes from the points in the vicinity of singularity of the Green's function. While the total field is approximated by the incident field in the first Born approximation, in this chapter. the total field is replaced by the renormalized or rescaled incident field. The advantage of the approach is that analytic Green's functions can be used in the computation. The nonlinear inverse problem is then solved in two steps, in each of which a linear problem is solved.

In the spectrum domain, the total field in the integral kernel is estimated by back-propagating the field at the boundary, in an attempt to overcome the limitations of the linearized solutions. Individual diffracted projections for a fixed incident wave vector, which is independent from other projections with different incident wave vector, is obtained by solving a Toeplitz recursive system. Once the spectrum of the

---

[5]Augustin Jean Fresnel, the French physicist, was born in 1788. Before embarking on his studies in optics he trained as a mathematician and civil engineer. While being responsible for the first mathematical treatment of diffraction he also concerned himself with engineering problems such as design of low mass lenses for use in lighthouses, (Encyclopedia Britannica, Internet edition. 1997).

perturbation function is obtained, the perturbation function representing medium inhomogeneity is reconstructed by the inverse Fourier transformation.

A stratified background of the media may be determined from well logs or transmission tomography and, according to the normal mode solution to the wave equation, the determined background can be used to rescale the incident field in order to maintain the perturbation small relative to the background. The perturbation function in each layer is sorted out from spatial Fourier spectrum of the scattered fields using the selection rule described in the last section of chapter 3.

1.3.3   Inversion of strong scattering using wave asymptotics

Chapter 4 describes wave phenomena using a ray model and the incident field is renormalized to a variable background medium. The Green's function is constructed using traveltimes from raytracing according to Hamilton's principle and the amplitude from the paraxial approximation. In the neighborhood of caustics, where the formal asymptotic solution does not exist, one may find the asymptotic solution in phase space and then return to real space (Maslov, 1988). The inverse problem is reformulated according to pseudodifferential operator theory. The resultant algorithm is similar to that of the Kirchoff migration, which is simple to implement. The synthetic and field data inversions demonstrate that the method is flexible and effective in applications to real problems.[6]

1.3.4   Inversion of random media

The basic difficulty of the inverse problem is to determine unknown Earth properties by analyzing the waves propagating through the media. When the distribution of the small scale inhomogeneities is too complicated to describe deterministically, we may treat them as random. Although Earth science data sets are not random usually, they are merely complicated and, essentially, deterministic. Nevertheless, the

---

[6]Sir William Roman Hamilton had in 1827 the remarkable distinction of being appointed Professor of Astronomy at Trinity College, Dublin, while he was still an undergraduate there (Encyclopedia Britannica, Internet edition, 1997).

random model works in practice and is an effective tool. Chapter 5 does not consider conventional approaches of effective medium, but uses the full wave representations of random media to invert the second order statistical properties of the media. The diffraction tomographic inversion procedure is used to recover the correlations of heterogeneity in the complex media. The resolved statistical quantities can be used to identify, e.g., fracture scales and orientations or to facilitate geostatistical simulations.

Numerical results based on the approach are presented for various situations encountered in practice. Notice that the recovered correlation function of the medium is multi-dimensional and may not necessary be a simple analytic form, such as Gaussian[7] as often assumed in geostatistical simulations.

---

[7]Karl Friedrich Gauss (1777-1855), was a German mathematician, astronomer and all round genius. His father was a bricklayer and expected Gauss to follow the same trade. His school teachers, however spotted his precocious talents and urged him to attend the university. For his doctoral thesis, he proved the fundamental theory of algebra and was also responsible for prime number theorem and the foundations of non-Euclidean geometry. His abilities were not confined to just mathematics. He designed many surveying instruments, was one of the inventors the electric telegraph and was the first to use paraxial ray approximation in optics. He was appointed professor of astronomy at Gottingen at the age of 30, but strongly discouraged students from attending his lectures. He published surprisingly little of his work, preferring to keep most of it in his drawers. Jacobi recounts visiting Gauss on a number of occasions to show him his latest work, only to have Gauss fish out some papers containing the same results (Encyclopedia Britannica, Internet edition, 1997).

Chapter 2

Wave Scattering Operators, Imaging, and Resolution

The essence of inverse scattering or diffraction tomography is to relate scattered wavefields to inhomogeneity or perturbations of the medium. By expressing the scattering integral equations in operator forms, new insight into the inversion problem is obtained. This approach leads to an array of tomographic inversion methods developed in subsequent chapters of the thesis. This chapter discusses scattering theory, diffraction tomography, and the resolution of the imaging operators. The first section describes the theory and formalism of wave scattering and defines the notation and terminology used throughout the thesis. The second section presents the scattering operators corresponding to various approximations to the scattering integral. The final section assesses the resolving power of the scattering operators.

2.1 Theory of wave scattering

Although scattering problems are most frequently formulated in the form of boundary-value problems for the wave or Helmholtz equations, it is also customary and useful to employ representation theory of wave fields to reformulate the problem as integrals over the scattering volume. These integral representations are central tools in inverse scattering.

10

2.1.1   Scalar waves

Let $c(\mathbf{x})$ denote the local velocity of propagation. The scalar wave equation for a fixed source position $\mathbf{s}$ can be written as,

$$\frac{1}{c^2(x)}\partial_t^2 u(\mathbf{x},\mathbf{s},t) - u_{,jj}(\mathbf{x},\mathbf{s},t) = f(\mathbf{s},t), \tag{2.1}$$

where

$$
\begin{aligned}
\mathbf{x}, t &= \text{spatial and time coordinates respectively.} \\
u &= \text{scalar wave field.} \\
c(\mathbf{x}) &= \text{local wave propagation velocity,} \\
(\cdot)_{,jj} &= \text{second order spatial partial derivative.} \\
\partial_t^2 &= \text{second order time derivative,} \\
f(\mathbf{s},t) &= \text{volume source density function.}
\end{aligned}
$$

In (2.1) the summation is implied over repeated indices and $j = 1, 2, 3$.

One can decompose the medium property, e.g. local velocity, as components of the background and perturbation, i.e., $1/c^2(\mathbf{x}) = 1/c_0^2(\mathbf{x})(1 - o(\mathbf{x}))$, where $c_0(\mathbf{x})$ is the background velocity and $o(\mathbf{x}) = (1 - c_0^2(\mathbf{x})/c^2(\mathbf{x}))$ with a bounded support is called the object function and represents inhomogeneity or perturbation of the subsurface medium. One can also decompose the total wave field u as a summation of the background field u_0 and scattered field u^s. They correspond to the wavefield in a medium without and with the presence of inhomogeneity, i.e.,

$$u(\mathbf{x},\mathbf{s},t) = u_0(\mathbf{x},\mathbf{s},t) + u^s(\mathbf{x},\mathbf{s},t).$$

The scattered field u^s satisfies the equation (see appendix A):

$$\frac{1}{c_0^2(\mathbf{x})}\partial_t^2 u^s(\mathbf{x},\mathbf{s},t) - u^s_{,jj}(\mathbf{x},\mathbf{s},t) = \frac{o(\mathbf{x})}{c_0^2(\mathbf{x})}\partial_t^2 u(\mathbf{x},\mathbf{s},t). \tag{2.2}$$

The term on the right hand of equation (2.2) may be interpreted as equivalent sources resulting from interactions between the wave field u and inhomogeneity of the medium $o(\mathbf{x})$.

Let $G = G(\mathbf{r}, \mathbf{x}, t)$ be the Green's function of (2.2) which propagates waves from point $\mathbf{x}$ to receiver location $\mathbf{r}$. G satisfies the following equation:

$$\frac{1}{c_0^2(x)}\partial_t^2 G - G_{,jj} = \delta(t)\delta(\mathbf{x} - \mathbf{r}), \tag{2.3}$$

where $G_{,jj}$ denotes $\partial^2 G/\partial^2 x_j$. Utilizing Green's theorem (Aki and Richards, 1980), one obtains

$$u^s(\mathbf{r}, \mathbf{s}, t) = \int_V \frac{o(\mathbf{x})}{c_0^2(\mathbf{x})}\partial_t^2 u(\mathbf{x}, \mathbf{s}, t) *_t G(\mathbf{r}, \mathbf{x}, t)dx, \tag{2.4}$$

which is the integral representation of scattered fields. The symbol $*_t$ is used to denote the convolution with time. The integration domain V is the support of $o(x)$ and is called scattering volume. The frequency domain equation (2.4) can be written as a Fredholm integral equation of the first kind:

$$u^s(\mathbf{r}, \mathbf{s}, \omega) = -\int_V m(\mathbf{x})u(\mathbf{x}, \mathbf{s}, \omega)G(\mathbf{r}, \mathbf{x}, \omega)dx, \tag{2.5}$$

where $m(\mathbf{x}) = \omega^2 o(\mathbf{x})/c_0^2(\mathbf{x})$ is denoted as the reduced model parameter and ω is angular frequency. The physical interpretation of equation (2.5) is depicted in figure 2.1.

2.1.2   Elastic waves

As in the case of scalar waves, we convert the differential wave equation into its integral representation. The elastic wave equation can be written as

$$\rho\partial_t^2 u_{jl} - (c_{lmpq}u_{jp,q})_{,m} = f_j. \tag{2.6}$$
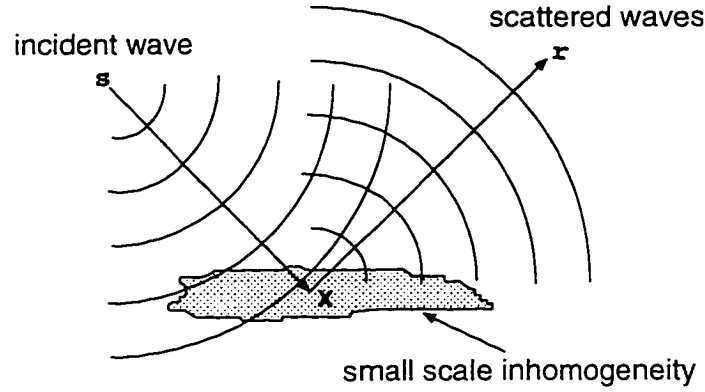
Figure 2.1: An inhomogeneity is characterized by a distribution of velocity perturbation in the host medium. An incident wave is launched from a source location s towards the inhomogeneity centered at x from which it is scattered to receiver locations r.

where

$$f_j \quad = \quad \text{the volume source density function,}$$

$$\rho \quad = \quad \rho(\mathbf{x}), \text{ the density,}$$

$$c_{lmpq} \quad = \quad c_{lmpq}(\mathbf{x}), \text{ elastic constants of the medium,}$$

$$u_{jl} \quad = \quad u_{jl}(\mathbf{x}, t), \text{ l-component of the wave field due to } f_j.$$

For an isotropic solid, the general tensor c_{lmpq} is simplified as

$$c_{lmpq} = \lambda \delta_{lm} \delta_{pq} + \mu(\delta_{lp}\delta_{mq} + \delta_{lq}\delta_{mp}), \tag{2.7}$$

where λ and μ are the two Lamé constants and δ_{lm} is the Kronecker symbol. Suppose the density and Lamé constants can be written as

$$\rho = \rho^0 + \rho', \quad \lambda = \lambda^0 + \lambda', \quad \mu = \mu^0 + \mu'.$$

where ρ^0, λ^0, and μ^0 are the background density and Lamé constants, and ρ', λ', and μ' their perturbations. As in the case of scalar waves, the scattered field u_{jl}^s is the

solution of the equation

$$\rho^0 \partial_t^2 u_{jl}^s - (c_{lmpq}^0 u_{jp,q}^s)_{,m} = -\rho' \partial_t^2 u_{jl} + (c_{lmpq}' u_{jp,q})_{,m} . \tag{2.8}$$

Let $\hat{G}_{kl} = \hat{G}_{kl}(\mathbf{r}, \mathbf{x}, t)$ be Green's tensor that satisfies the equation:

$$\rho^0 \partial_t^2 \hat{G}_{kl} - (c_{lmpq}^0 \hat{G}_{kp,q})_{,m} = \delta_{kl}\delta(t)\delta(\mathbf{r} - \mathbf{x}), \tag{2.9}$$

and utilizing Betti's Theorem (the vector equivalent of Green's Theorem for scalars). the integral representation of the scattered wave field u_{jk}^s can be obtained as

$$u_{jk}^s(\mathbf{s}, \mathbf{r}, t) = -\int_V [\rho' \partial_t^2 u_{jl} *_t \hat{G}_{kl} + c_{lmpq}' u_{jp,q} *_t \hat{G}_{kl,m}]d\mathbf{x}. \tag{2.10}$$

where $\hat{G}_{kl}$ is Green's function from point $\mathbf{x}$ to receiver location $\mathbf{r}$. $\hat{G}_{kl,m}$ is the spatial derivative of $\hat{G}_{kl}$. Notice that the second term on the right is obtained via integrating by parts and the boundary term vanishes because the perturbations c_{lmpq}' are zero on the boundary ∂V (see Appendix B). Again, the symbol $*_t$ is used to denote the convolution over time. In the frequency domain, (2.10) resumes following form

$$u_{jk}^s(\mathbf{s}, \mathbf{r}, \omega) = \int_V [\rho' \omega^2 u_{jl} \hat{G}_{kl} - c_{lmpq}' u_{jp,q} \hat{G}_{kl,m}]d\mathbf{x}. \tag{2.11}$$

2.1.3 Wave scattering formalism

One might consider the measured wave field u as the elements of the data matrix $\mathcal{D}$. The model parameters m of the media can be represented as elements of model parameter matrix $\mathcal{M}$. The data and model parameter matrices are related by the following implicit equation

$$\mathbf{f}(\mathcal{D}, \mathcal{M}) = 0,$$

where $\mathbf{f}$ is a functional relating the data set $\mathcal{D}$ to model parameter set $\mathcal{M}$. Obviously. for a forward problem, functional $\mathbf{f}$ maps a set of model parameters onto the set of data, provided that $\mathbf{f}$ and the parameter set are known. For an inverse problem, on

the other hand, **f** constructs the parameter set from the data set, provided **f** and the data set are known. These mappings are shown schematically in figure 2.2. [1]

forward mapping

f (D, M)

inverse mapping

Parameter set M Data set D
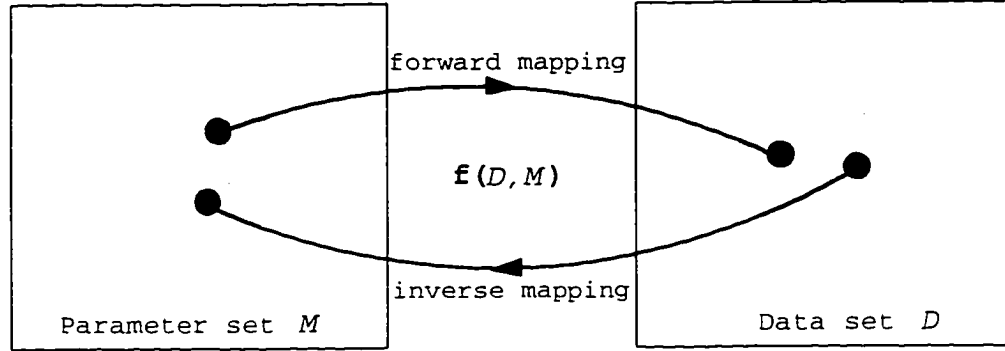
Figure 2.2: Illustrating the forward and inverse scattering processes as mappings between parameter and data sets M and D via functional $\mathbf{f}(\mathcal{D}, \mathcal{M})$.

In order to get an explicit description of functional **f**, we write integral equation (2.5) or (2.11) into operator forms. For example, equation (2.5) in the interior scattering volume can be written as

$$u(\mathbf{x}, \mathbf{x}') = u_0(\mathbf{x}, \mathbf{x}') + \int_V u(\mathbf{y}, \mathbf{x}') m(\mathbf{y}) G(\mathbf{x}, \mathbf{y}) d\mathbf{y}, \qquad (2.12)$$

in which $u = u_0 + u^s$ is used. The source location **s** and receiver location **r** are generalized to any position within the domain V. The variable ω is omitted without confusion. Within the domain V, the wave field $u(\mathbf{x}, \mathbf{x}')$ has two indices, one associated with the observer **x** and the other one associated with the source $\mathbf{x}'$, i.e., u may be regarded as a matrix. Similarly, G is also a matrix, and $m(\mathbf{y})$ is a diagonal matrix.

---

[1]Note that if these general concepts are related to a real scattering experiment, then the complicated relationship between the mapping and the respective sets soon becomes apparent. The parameter set is unlikely to represent a complete description of the medium, being deficient of specific parameters which may contribute to the scattered field, or of geometrical constraints which modify the effect these parameters may have. This limitation is due to the facts that inverse problems are generally ill-posed and therefore the noise affecting the data may have produced arbitrarily large errors in the solution. As a consequence one can only estimate an approximated solution.

Consequently, equation (2.12) may be written in operator form:

$$\mathcal{U} = \mathcal{U}_0 + \mathcal{G}\mathcal{M}\mathcal{U}, \tag{2.13}$$

where the calligraphic symbols

$$\mathcal{U} \quad = \quad \text{operator corresponding to total field } u.$$

$$\mathcal{U}_0 \quad = \quad \text{operator corresponding to incident field field } u_0.$$

$$\mathcal{G} \quad = \quad \text{operator corresponding to Green's function } G.$$

$$\mathcal{M} \quad = \quad \text{operator corresponding to object function } m.$$

The ordering of the operation is important and cannot be altered at will. the operator equation (2.13) is a form independent of linear vector spaces, which is valid regardless of. e.g., whether $\mathcal{U}, \mathcal{G}$ and $\mathcal{M}$ are in spatial or wavenumber domain representation. Using operator equation (2.13), the functional **f** can be expressed explicitly as

$$\mathbf{f}(\mathcal{D}, \mathcal{M}) = \mathcal{D} - \mathcal{G}\mathcal{M}\mathcal{U} = 0, \tag{2.14}$$

where $\mathcal{D} = \mathcal{U} - \mathcal{U}_0$. Furthermore, one can find the solution to equation (2.13) in the operator sense. By solving for $\mathcal{U}$, one obtains

$$\mathcal{U} = (\mathcal{I} - \mathcal{G}\mathcal{M})^{-1}\mathcal{U}_0. \tag{2.15}$$

By substituting equation (2.15) back into (2.13), one has

$$\mathcal{U} = \mathcal{U}_0 + \mathcal{G}\mathcal{M}(\mathcal{I} - \mathcal{G}\mathcal{M})^{-1}\mathcal{U}_0. \tag{2.16}$$

From the structure of equation (2.16), we can see that the scattered field which is the second term on the right hand of equation (2.16) is nonlinearly dependent on the operator $\mathcal{M}$. The operator $(\mathcal{I} - \mathcal{G}\mathcal{M})^{-1}$ is accounts to multiple scattering. This

becomes obvious if it is expanded in a geometrical series, i.e.

$$\mathcal{U} = \mathcal{U}_0 + \mathcal{G}\mathcal{M}\mathcal{U}_0 + \mathcal{G}\mathcal{M}\mathcal{G}\mathcal{M}\mathcal{U}_0 + ... \tag{2.17}$$

The n-th term in the above series corresponds to the incident field being scattered n times. Although the above operator equations do not solve new problems. they provide new insights to the scattering equation in coordinate representation and facilitate solving inverse scattering problems.

2.2   Scattering operators

Obviously, the relation (2.14) is nonlinear and approximations have to be made in order to apply to inverse problems. For the purpose of implementation. equation (2.14) can be written as the following matrix form:

$$\mathbf{d} - \mathcal{A}\mathbf{m} = 0.$$

where $\mathbf{d}$ and $\mathbf{m}$ are the vectors of data (scattered field) and the model parameter (inhomogeneity of the media) respectively. The matrix $\mathcal{A}$ is the data kernel [2] of equation (2.13) and called the scattering operator. In the following sections we present the various scattering operators resulting from the approximations to operator equation (2.14) from the perspective of linearization either with respect to the model parameters or data.

2.2.1   Single scattering

The series (2.17) may or may not be convergent depending on the strength and size of the inhomogeneity. A homogeneous background medium is considered in the following. Under favorable conditions (Kelley, 1958), the series (2.17) can be truncated

---

[2]In the theory of integral equations, the data kernel is the kernel function of a integral equation. Here. $\mathbf{d} - \mathcal{A}\mathbf{m}$ is analogy to $d(\mathbf{y}) = \int A(\mathbf{y}, \mathbf{x})m(\mathbf{x})d\mathbf{x}$ (see equation (2.12)).

and considered as single scattering:

$$\mathcal{U} \approx \mathcal{U}_0 + \mathcal{G}\mathcal{M}\mathcal{U}_0, \tag{2.18}$$

or in matrix form

$$\mathbf{d} - \mathcal{A}_b \mathbf{m} = 0, \tag{2.19}$$

where data $\mathbf{d} = \mathbf{u} - \mathbf{u}_0$ and $\mathbf{m}$ are the model parameters. The matrix $\mathcal{A}_b$, the data kernel of (2.18) is called the single scattering operator which relates the scattered field and model parameters linearly. The equation (2.18) constitutes the first-order Born approximation or single scattering approximation, one of the most widely used solutions for inverse scattering problems. The relation (2.19) is linear in both data and model parameters. It can be evaluated with a Fourier transformation. We summarize the Born or Rytov[3] approximations and diffraction tomography in Appendix A. Assuming single scattering, conventional diffraction tomographic inversion requires that the perturbation function to the background be small. This is a strong restriction in applications.

2.2.2 Renormalized scattering

From equation (2.15), one can see that the total field operator is a product of the multiple scattering operator and incident field operator. Based on equation (2.15), we propose an approximation (see Chapter 3), in which the unknown total field is simplified as a modified incident field, i.e.,

$$u(\mathbf{x}) \approx u_\gamma(\mathbf{x}) = \Gamma(\mathbf{x})u_0(\mathbf{x}) \tag{2.20}$$

---

[3]During the course of his investigations into the diffraction of light by ultrasound, Rytov employed an approximation which is now frequently used in many scattering problems. Although the Rytov approximation results in a simplification of the wave equation and leads to simple solutions of the direct scattering problem, it is also another of those rare schemes which facilitates an inverse solution in closed form.

where u is the total wave field, u_0 is the incident field, and $\Gamma(\mathbf{x})$ is the Rayleigh normalization factor accounting for multiple scattering effects, i.e.,

$$\Gamma(\mathbf{x}) = (1 - \int_V m(\mathbf{x}')G(\mathbf{x}, \mathbf{x}')d\mathbf{x}')^{-1}. \tag{2.21}$$

Substituting the approximation $\mathcal{U} \approx \mathcal{U}_\gamma$, where $\mathcal{U}_\gamma$ is an operator corresponding to the approximated total wave field u_γ, into the right hand of the operator equation (2.13). one has

$$\mathcal{U} \approx \mathcal{U}_0 + \mathcal{G}\mathcal{M}\mathcal{U}_\gamma. \tag{2.22}$$

Equation (2.20) can also be rearranged into

$$\mathcal{U} \approx \mathcal{U}_0 + \mathcal{G}\dot{\mathcal{M}}\mathcal{U}_0. \tag{2.23}$$

where $\dot{\mathcal{M}}$ is the operator corresponding to the combined function $\Gamma(\mathbf{x})m(\mathbf{x})$. Therefore, equation (2.19) can still be applied in this approximation but for the combined parameters $\dot{\mathbf{m}} = \Gamma(\mathbf{x})\mathbf{m}(\mathbf{x})$, i.e.

$$\mathbf{d} - \mathcal{A}_b\dot{\mathbf{m}} = 0, \tag{2.24}$$

Equation (2.24) is linear for data but still nonlinear in the model parameters through the parameter $\dot{\mathbf{m}}$. We can use the procedure of single scattering to invert $\dot{\mathbf{m}}$ first and solve $m(\mathbf{x})$ using equation (2.21) (see Chapter 3).

2.2.3   Wave field back-propagation

In the above sections we approximate the unknown total field in the spatial domain. Now, we want to estimate the total field in the data kernel from the spectrum of the observation. If we replace unknown $\mathcal{U}$ on the right hand equation (2.13) by the Fourier extrapolation of the observed wave field, one can obtain a similar result to

that of the Rayleigh renormalization (see Chapter 3). That is

$$\mathcal{U} \approx \mathcal{U}_0 + \mathcal{G}\mathcal{M}\mathcal{U}_e, \qquad (2.25)$$

where the operator $\mathcal{U}$, corresponding to the total wave field on the right hand of equation (2.12), is replaced by the operator $\mathcal{U}_e$ corresponding to the extrapolated wave field u_e from the observed field at the boundary:

$$u_e(\mathbf{x}, k_s) = \int_{D_k} u(k_s, k_g) e^{i(\gamma_g x + k_g z)} dk_g, \qquad (2.26)$$

where $u(k_s, k_g)$ is the spectrum of the received wavefield, k_g and k_s are the wavenumbers along the receiver array and source array respectively, $\gamma_g = \sqrt{k_0^2 - k_g^2}$, and D_k is the integrating domain defined by the receiver aperture. This extrapolation assumes a constant velocity, as in the case of the Fourier phase migration. Under this scenario, the corresponding matrix equation is:

$$\mathbf{d} - \mathcal{A}_e \mathbf{m} = 0, \qquad (2.27)$$

where the matrix $\mathcal{A}_e$ is the data kernel of equation (2.25) and is called the extrapolated scattering operator. Equation (2.27) is linear for the model parameters but still nonlinear in the data through operator $\mathcal{A}_e$. The diffraction projections of $\mathbf{m}$ are obtained by solving the above system numerically. The model parameter $\mathbf{m}$ is obtained by taking the inverse Fourier transforms of the projections (Chapter 3).

2.2.4 Distorted single scattering

In the distorted single scattering, the incident field u_0 of a homogeneous background is replaced by the distorted field of a variable background. The background medium is chosen such that the strength of inhomogeneity against the variable background is small. Therefore, the Born series is insured to converge rapidly. The corresponding

operator equation can be written as

$$\mathcal{U} = \mathcal{U}_d + \mathcal{G}_d \delta \mathcal{M} \mathcal{U}, \qquad (2.28)$$

where $\mathcal{U}$ is the operator corresponding to total wave field u, $\mathcal{U}_d$ is the operator corresponding to the background field, $\mathcal{G}_d$ is the operator corresponding to the Green's function of variable background medium, and $\delta \mathcal{M}$ is used to denote the operator corresponding to the model parameter perturbation with regard to the variable background medium. For inverse scattering problems, $\delta \mathcal{M}$ is unknown and to be sought.

As in the case of the Born approximation, one may replace $\mathcal{U}$ by $\mathcal{U}_d$ on the right hand of equation (2.28), i.e.,

$$\mathcal{U} = \mathcal{U}_d + \mathcal{G}_d \delta \mathcal{M} \mathcal{U}_d. \qquad (2.29)$$

This approximation is called the distorted wave approximation and the corresponding matrix equation is:

$$\mathbf{d} - \mathcal{A}_d \delta \mathbf{m} = 0, \qquad (2.30)$$

where data $\mathbf{d} = \mathbf{u} - \mathbf{u}_d$ are scattered fields and the matrix $\mathcal{A}_d$ is the data kernel of equation (2.29). Equation (2.30) is linear both in data $\mathbf{d}$ and $\delta \mathbf{m}$, but matrix $\mathcal{A}_d$ depends on prior knowledge of the variable background medium. This approach is appropriate in the case of a high frequency scattering regime where the Green's function of variable background medium can be constructed by the WKB ray method (see Chapter 4). The matrix $\mathcal{A}_d$ is called the asymptotic scattering operator.

2.3 Resolution of the scattering operators

The spatial resolution is the detection limit of the size of heterogeneities in an artifact free image, which is determined by the aperture of the source, the focal spot, and the aperture of the receivers. Recall that, for traveltime imaging, the lateral resolution of the slowness image is proportional to the first Fresnel zone (Claerbout, 1984)

depicted in figure 2.3 (Woodward, 1989).   The goal of diffraction tomography is
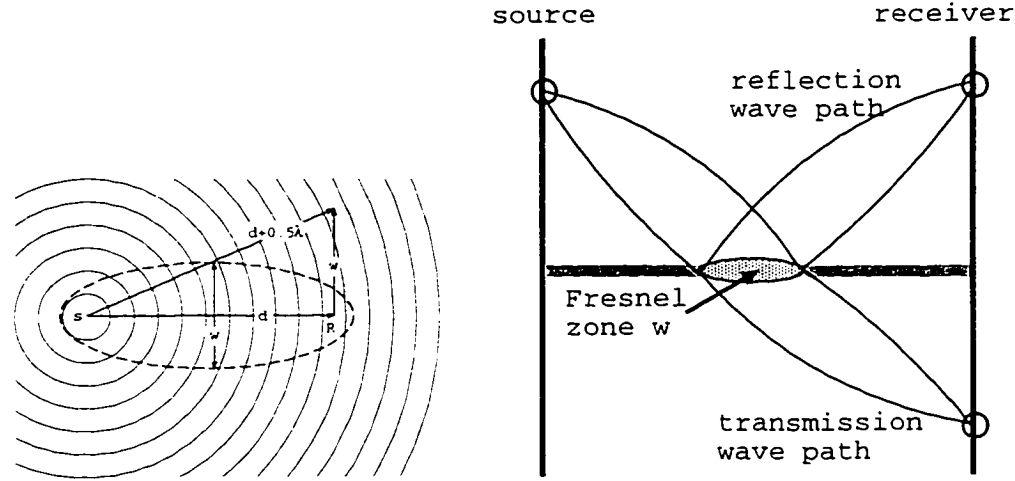
Figure 2.3: The lateral resolution of traveltime tomography is in the order of the first Fresnel zone. Left panel shows the estimation of the Fresnel zone: $w \sim \sqrt{d\lambda}$, since $d^2 + w^2 = (d + 0.5\lambda)^2$. S and R are source and receiver locations respectively, d is the source-receiver separation, and λ is the dominant source wavelength. Right panel shows the zone affecting lateral resolution of traveltime imaging.

to sample the spectrum of object function then invert it to yield the object image. The resolution of the image is determined by the temporal bandwidth of the probing wavefield and the spatial bandwidth of the observation system. Figure 2.4 shows a scattering experiment and the projections in the wave number domain under the single scattering approximation. The spatial bandwidth is achieved with the combination of the multifrequency or multiple source-receiver views. It can be proven that the horizontal resolution is generally proportional to the wavelength of incident waves, and vertical resolution depends on the sampling interval of the source and receiver apertures (see Appendix A).

In the following subsections, I examine the resolution attainable through the scattering operators obtained in the previous section by analyzing the model resolution matrix [4] and the image of point targets. Some factors that affect resolution also are

---

[4]Suppose that data **d** and model parameters **m** are related by $\mathbf{d} = \mathcal{A}\mathbf{m}$. Model parameters can be inverted as $\dot{m} = \mathcal{A}^{-1}\mathbf{d}$, or $\dot{\mathbf{m}} = \mathcal{R}\mathbf{m}$ where $\mathcal{R} \equiv \mathcal{A}^{-1}\mathcal{A}$ is called model resolution matrix. If $\mathcal{R} = \mathcal{I}$, model parameters are perfectly resolved. In terms of integral operator
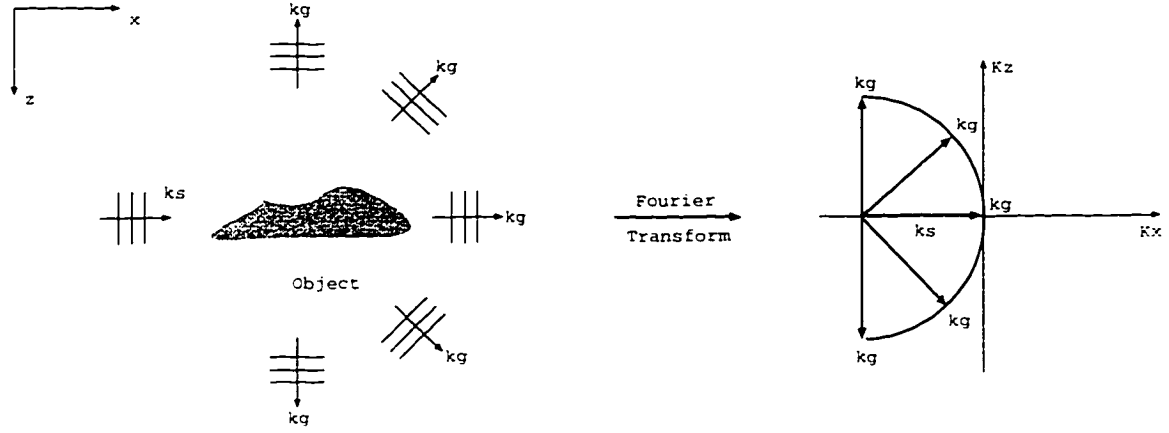
Figure 2.4: Plane wave scattering (left panel) and the information it carries on the object in the wavenumber domain (k_x, k_z) (right panel). k_s and k_g are the propagation vectors of the incident wave and scattered wave respectively.

analyzed.

2.3.1   Case of the single scattering operator

The model resolution matrix of the single scattering operator is defined as

$$\mathcal{R}_b \equiv \mathcal{A}_b^{-1} \mathcal{A}_b.$$

Notice that $\mathcal{A}_b$ is linear both for data and model parameters. In general, it can be evaluated through Fourier analysis. For a two dimensional problem, the model resolution matrix has the analytic form:

$$\mathcal{R}_b = 4 K_x^{\max} K_z^{\max} \text{sinc}(K_x^{\max}(x - x'))\text{sinc}(k_z^{\max}(z - z')) \qquad (2.31)$$

where $K_x^{\max}$ and $K_z^{\max}$ are the wavenumber bandwidths in the horizontal and vertical directions respectively, and function $\text{sinc}(x) = \sin(x)/x$. In the case of the cross well survey, $K_x^{\max} = k_0$ where $K_0 = \omega/c_0$ and $K_z^{\max} = \pi/\Delta$, and Δ is the sampling interval of the receiver aperture. One can see that to provide sufficient resolving power,

---

$\mathcal{R}(\mathbf{x}, \mathbf{x}') \equiv \int_D A^{-1}(\mathbf{y}, \mathbf{x}') A(\mathbf{y}, \mathbf{x}) d\mathbf{y}.$

the bandwidth of sampled wavenumber K_x and K_z should overlap the wavenumber spectrum of the heterogeneity being imaged. The resolution is approximately 1λ in x and 0.5λ in z, independent of target location.
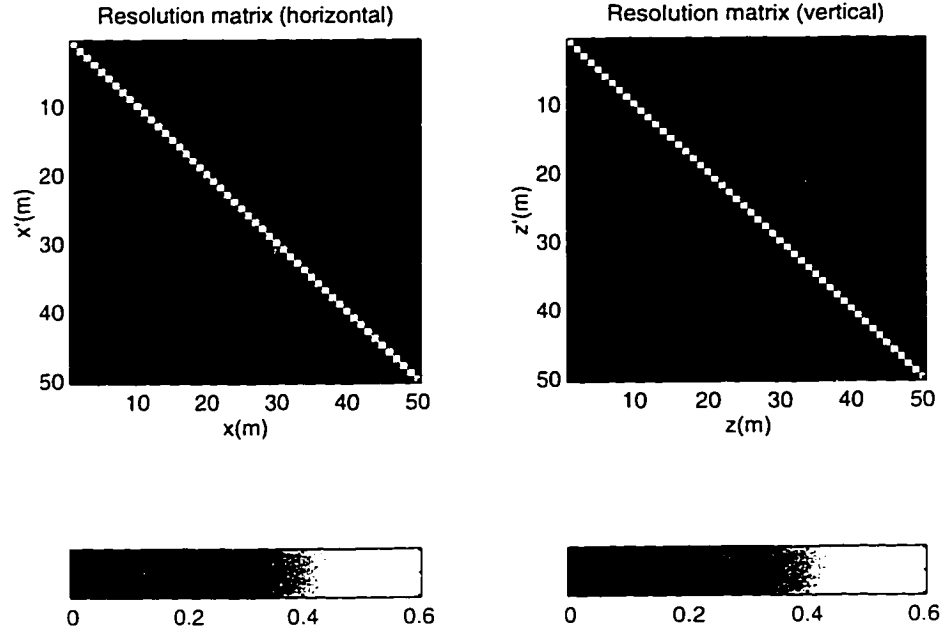
Figure 2.5: The resolution matrices of a single scattering operator. Sampling interval along the receiver aperture is 1 m, background velocity is 4000 m/s, and temporal frequency of incident wave is 500 Hz. The resolution matrix in regard to horizontal and vertical directions are displayed in the left and right panel respectively. Note that the maximum value of the images is zoomed at 0.6 from 1 for the purpose of display.

In figure 2.5 the model resolution matrices in the horizontal and vertical directions are displayed. One can see that the model resolution in the vertical direction is closer to the identity matrix. Notice that the model resolution matrix only represents the maximum resolution achievable through the scattering operator $\mathcal{A}_b$. The quality of images reconstructed using diffraction tomography are also dependent on the specific sampling geometry. The wavenumber coverage is restricted by the sampling geometry of the survey (see appendix A). In figure 2.6, the wavenumber coverage of the crosswell survey geometry is displayed. The left and right panels of figure 2.6 are multi-view at a single frequency and multi-view with multi-frequency coverage respectively. The horizontal coverage is limited and therefore horizontal resolution is reduced. The
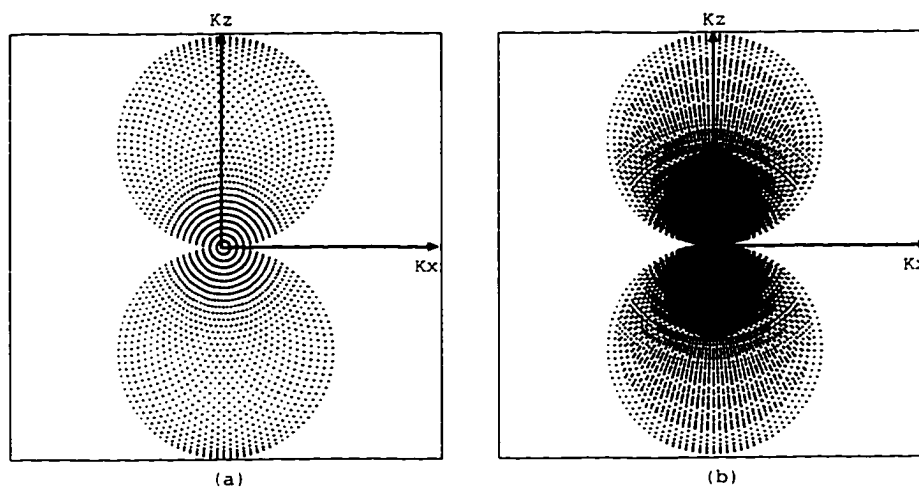
Figure 2.6: Fourier coverage for crosswell seismic profiling of a infinity long source and receiver aperture. The background velocity is $3000m/sec$. (a) depicts the the multi-view coverage of a single frequency at 1000 Hz and (b) shows the multi-view coverage of the multi-frequencies from 10 to 1000 Hz.
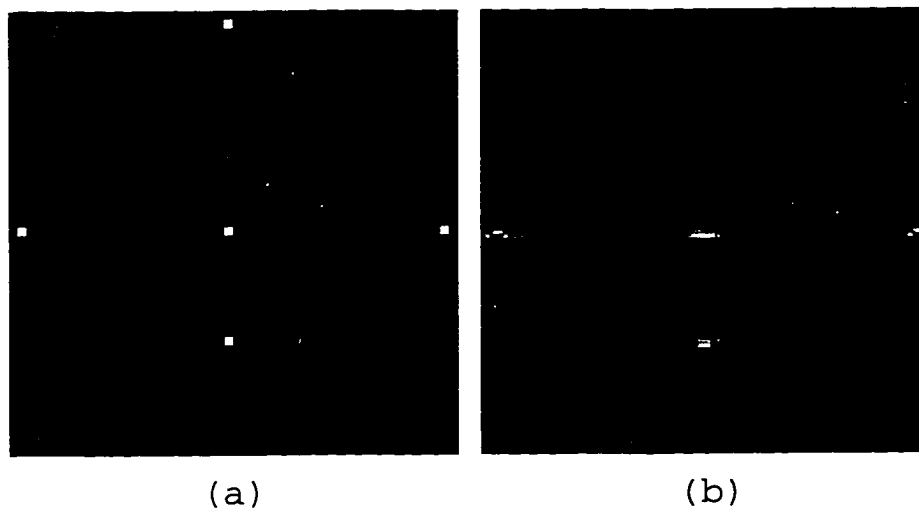
Figure 2.7: The inversion of a diffractor model with the single scattering approximation. Background velocity is 3500 m/s, velocity of diffractor is 5000 m/s, and temporal frequency is 500 Hz. (a) depicts the model and (b) shows the first Born approximation reconstruction from crosswell synthetic data.

coverage can be improved by using multiple frequencies. Figure 2.7 shows an image of point targets at four locations, for a crosswell experiment with 128 source and 128 receivers. The pixel spacing in the image is $\lambda/4$. The point target scattered data were generated by the method of moments. As expected, the resolution is significantly poorer in the horizontal direction because of poor coverage in K_x.

2.3.2   Case of the renormalized scattering operator

The analysis in the previous section is based on a linear system which results in the single scattering approximation in a homogeneous background medium. However, if multiple scattering is taken into account, the above analysis becomes invalid because a nonlinear system is involved. The operator $\mathcal{A}_e$ is linear for model parameters but nonlinear for data; i.e. $\mathcal{A}_e$ is data dependent. By extending the work of Berryman. (1994). we define a generalized resolution matrix, e.g. for renormalized scattering operator $\mathcal{A}_e$:

$$\mathcal{R}_e \equiv \mathcal{I} - e^{-n\mathcal{A}_e^T \mathcal{A}_e}. \tag{2.32}$$

where $\mathcal{R}_e$ is the generalized resolution matrix, $\mathcal{I}$ is the identity operator. $\mathcal{A}_e^T$ is the transpose of $\mathcal{A}_e$, and n is the number of iterations.[5]   The generalized resolution

---

[5]Suppose equation $\mathcal{A}_e \mathbf{v} = \mathbf{d}$ is solved iteratively starting with a initial model $\mathbf{v}^0$, i.e.,

$$\mathcal{A}_e^0 \mathbf{v}^0 = \mathbf{d}, \quad \mathcal{A}_e^1 \mathbf{v}^1 = \mathbf{d} - \mathcal{A}_e \mathbf{v}^0, \quad ...$$

For the nth iteration, it can be written, formally, as

$$\mathcal{A}_e^n \mathbf{v}^n = (\mathcal{I} - \mathcal{A}_e \mathcal{X}(n))\mathbf{d},$$

where $\mathcal{X}$ is an unknown inverse of $\mathcal{A}^{(n-1)}$. We want the residual $\Delta \mathbf{d} = ||(\mathcal{I} - \mathcal{A}_e \mathcal{X})\mathbf{d}||$ as small as possible to produce an optimal solution. To minimize $\Delta \mathbf{d}$, a sufficient condition is

$$\frac{\partial \mathcal{X}}{\partial n} = \mathcal{A}_e^T (\mathcal{I} - \mathcal{A}_e \mathcal{X}),$$

(Berryman, 1994). Following conventional definition, the effective resolution matrix is defined as $\mathcal{R}_e \equiv \mathcal{X} \mathcal{A}_e$. Obviously,

$$\frac{\partial \mathcal{R}_e}{\partial n} = \frac{\partial \mathcal{X}}{\partial n} \mathcal{A}_e, \quad or \quad \frac{\partial \mathcal{R}_e}{\partial n} = \mathcal{A}_e^T \mathcal{A}_e (\mathcal{I} - \mathcal{R}_e).$$

matrices with different iterations are displayed in figure 2.8. The data (total wave field spectrum) is generated using the moment method for a five diffractor model. One can see, as expected, that as the number of iterations increased, the resolution matrix is closer to the identity matrix. The generalized matrix is also useful when the system is solved with iteration methods such as the conjugate gradient method. Iteration methods demand less computer memory compared to, e.g., the singular value decomposition (SVD) method.
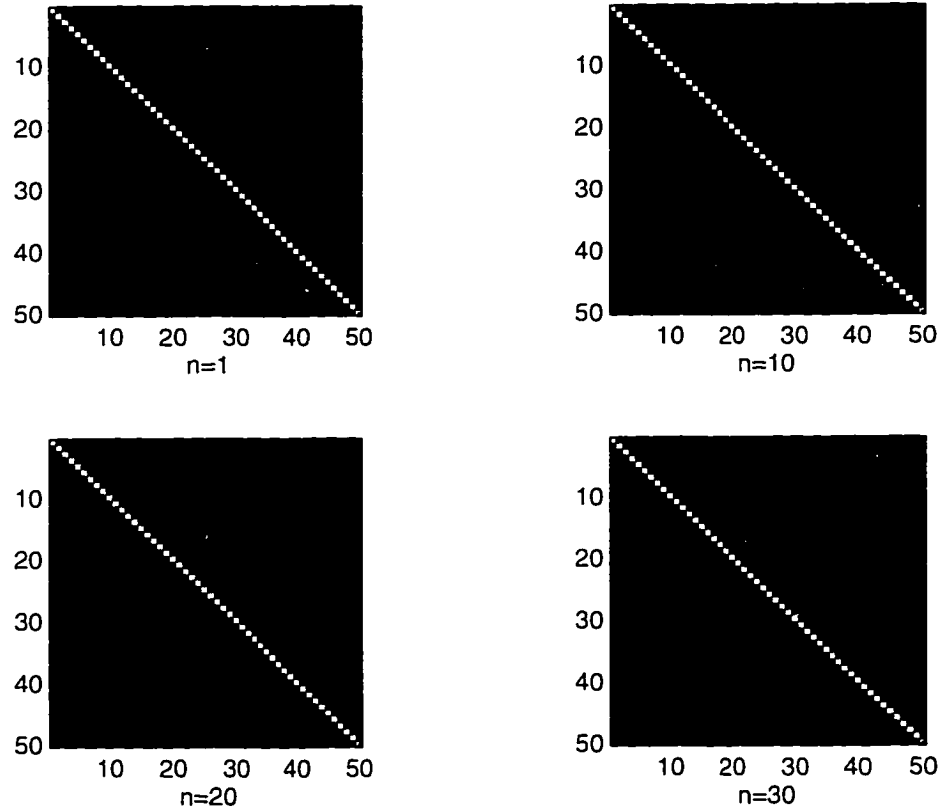
Figure 2.8: The generalized resolution matrices of the extrapolated scattering operator. The displayed matrices are for horizontal resolution. The background velocity is 3500 m/s, and temporal frequency of incident wave is 500 Hz. The wave field spectrum embedded in the operator $\mathcal{A}_e$ is the synthetic data of a diffractor model. n is the iteration number.

If system $\mathbf{d} = \mathcal{A}_e \mathbf{m}$ is solved by SVD, it is also possible to analyze the model

from which $\mathcal{R}_e$ can be solved in terms of $\mathcal{A}_e^T \mathcal{A}_e$ and number of iterations.

resolution by examining the diagonal matrix Λ matrix [6] of SVD. Figure 2.9 compares the singular value distributions of the operator $\mathcal{A}_e$ of a diffractor model with that of the single scattering operator $\mathcal{A}_b$. We can see that the distribution of the singular value from the extrapolated scattering operator is flatter than that of single scattering operator, and, therefore, has better resolution.
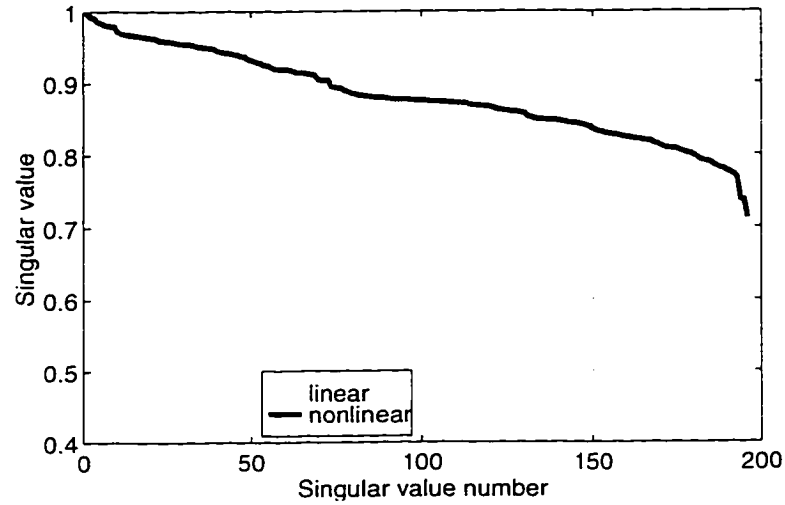
Figure 2.9: The singular value distribution of scattering operators: the extrapolated scattering operator versus the single scattering operator.

We invert the diffractors from the synthetic data to demonstrate how good the resolving power of the operator $\mathcal{A}_e$ is compared to that of the single scattering operator $\mathcal{A}_b$. For the forward modeling, both source and receiver lines are $200m$, respectively. and the spatial sampling interval along the source and receiver aperture is $2m$. The background velocity is $3500m/s$, velocity of the diffractors is $5000m/s$, and frequency of incident wave is 500 Hz. The reconstructions are displayed in figure 2.10. One can see that the overall quality of the reconstruction from operator $\mathcal{A}_e$ is better than that

---

[6]The number of significant singular values as well as their distribution, i.e. the rate that the eigenvalues of $\mathcal{A}_e$ approach 0, demonstrates the influence of the data structure which is determined by the survey geometry and bandwidth. The number of singular values that fall below the cutoff value and are set to zero measures the amount of information lost in pseudoinverse. Often this cutoff value is chosen to be percentage of largest singular value based on up the knowledge of the signal-to-noise ratio. The value of the largest singular value is dependent upon the the spacing of the original samples.

from operator $\mathcal{A}_b$, especially in the magnitude. But the resolutions of the operator $\mathcal{A}_e$ and $\mathcal{A}_b$ are, more less, the same. This confirms that, usually, resolution analysis with linear approximation is good enough since the main factors to influence the resolution are spatial and temporal frequency bandwidth given an observation geometry. The

(a)   (b)   (c)
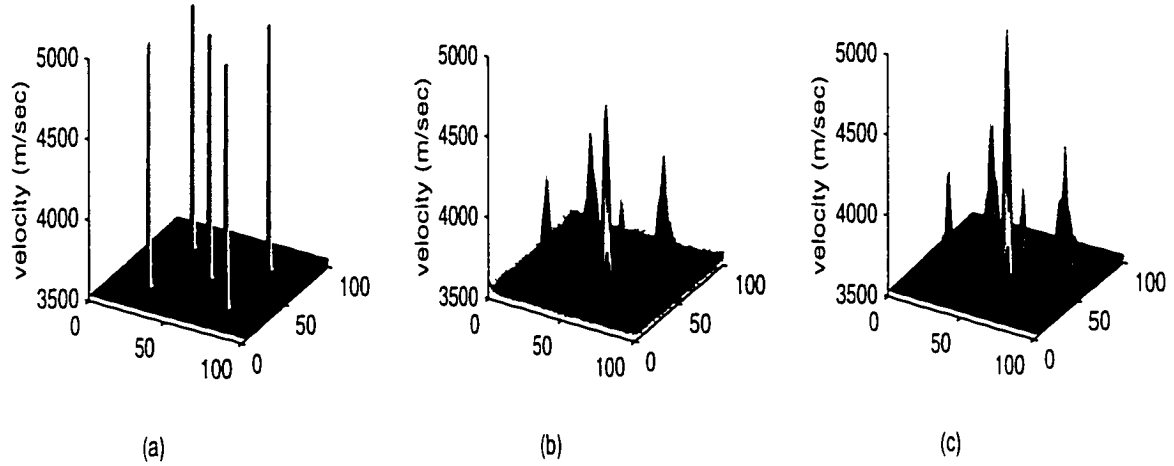
Figure 2.10: The comparison of the resolution of a diffractor model using single and extrapolated scattering operators: Spatial sampling interval along the source and receiver aperture is $2m$, the background velocity is $3500m/s$, velocity of diffractor is $5000m/s$, and temporal frequency is $500Hz$. (a) is the model of five diffractors, (b) is the reconstruction from the single scattering operator $\mathcal{A}_b$, and (c) is the reconstruction from the renormalized scattering operator $\mathcal{A}_e$. The average absolute differences are 21.3 between (a) and (b), and 6.7 between (a) and (c).

average absolute differences between the model and reconstructions, i.e., $error = E(|x - y|)$, are calculated. The difference between the model and reconstruction using the single scattering operator $\mathcal{A}_b$ is 21.3, while the difference between the model and the reconstruction using the renormalized scattering operator $\mathcal{A}_e$ is 6.7. This demonstrates that one can image better using the renormalized scattering operator.

2.3.3   Case of the asymptotic scattering operator

The model resolution matrix of the asymptotic scattering operator $\mathcal{A}_d$ is defined as

$$\mathcal{R}_d \equiv \mathcal{A}_d^{-1}\mathcal{A}_d \qquad (2.33)$$

As with the single scattering, the resolution matrix $\mathcal{R}_d$ can be expressed analytically (Chapter 4):

$$R_d(\mathbf{x}, \mathbf{x}') = \int |J(\mathbf{k}; \mathbf{r}, \mathbf{s})| e^{\imath k_j (x'_j - x_j)} d\mathbf{r} d\mathbf{s}, \qquad (2.34)$$

where $k_j(\mathbf{x}) = \omega(\tilde{\phi}_j(\mathbf{x}, \mathbf{s}) + \hat{\phi}_j(\mathbf{x}, \mathbf{r}))$, and $j = 1, 2, 3$. Notice that $\tilde{\phi}$ and $\hat{\phi}$ are eikonal functions from the source to the image point and from the image point to the receiver respectively. The Jacobian transformation is

$$J(\mathbf{k}; \mathbf{r}, \mathbf{s}) = k_0^2(\mathbf{x}) sin\theta(\mathbf{g}, \mathbf{s}) \frac{\partial\theta(\mathbf{x}, \mathbf{s})}{\partial s} \frac{\partial\theta(\mathbf{g}, \mathbf{x})}{\partial g}. \qquad (2.35)$$

where $\theta(\mathbf{x}, \mathbf{s})$ and $\theta(\mathbf{g}, \mathbf{x})$ are the incident angle and scattering angle at the location $\mathbf{x}$, respectively; $\theta(\mathbf{g}, \mathbf{s})$ is the difference between $\theta(\mathbf{x}, \mathbf{s})$ and $\theta(\mathbf{g}, \mathbf{x})$. This form is derived, under the distorted single scattering approximation, using pseudodifferential operator theory (Appendix B). The resolution matrix $\mathcal{R}$, a function of frequency, background velocity, and survey geometry, provides insight into how these factors influence the resolution of the operator $\mathcal{A}_d$. Certainly, the temporal and spatial bandwidth play the same roles as demonstrated in previous sections.

Instead of using the procedure of SVD to analyze the eigenvalues of $\mathcal{R}_d$, we invert the diffractor model to assess directly the resolving power of the operator $\mathcal{A}_d$. Figure 2.11 shows an image of diffractors at five locations, for the crosswell experiment with 128 source and receivers. The pixel spacing in the image is $\lambda/2$. The diffractor scattering data were generated by the moment method.
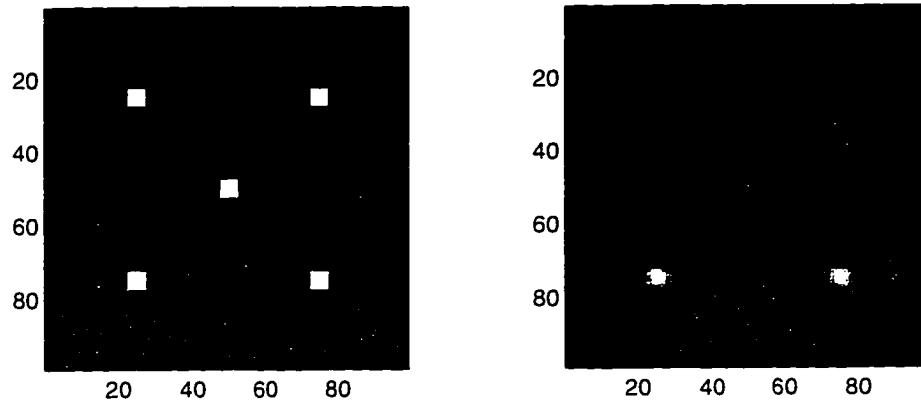
Figure 2.11: Reconstructed diffractor model using the distorted single scattering operator $\mathcal{A}_d$: the left panel is a model of five diffractors in a two layer background; the right panel is the reconstruction.

Effects of irregular sampling

In order to show the effects of irregular sampling along source/receiver aperture. singular value decomposition is applied to $\mathcal{R}_d$. In figure 2.12. 10 different versions of sampling schemes are displayed. The singular values of the ten different $\mathcal{R}_d$ matrices corresponding to ten different receiver apertures are plotted in figure 2.13. One can see that as irregularity increases from curve 1 to curve 10 of the aperture, the first singular value of the resolution matrix increases and the drop-off of the singular values becomes steeper.

2.4 A remark on migration and inverse scattering

Seismic imaging techniques can be subdivided in migration and inverse scattering. The object functions for inversion and migration are, respectively, the medium perturbation parameters and reflectivity. The perturbation describes the difference between the medium parameters of the actual medium and the background medium while the reflectivity is proportional to the discontinuity in the actual medium.

Migration can be viewed as either backprojection (diffraction-stack) or backpropagation. i.e., the recorded waves are extrapolated either downward in space or backward in time and the image extracted from the extrapolated wavefield by an imaging
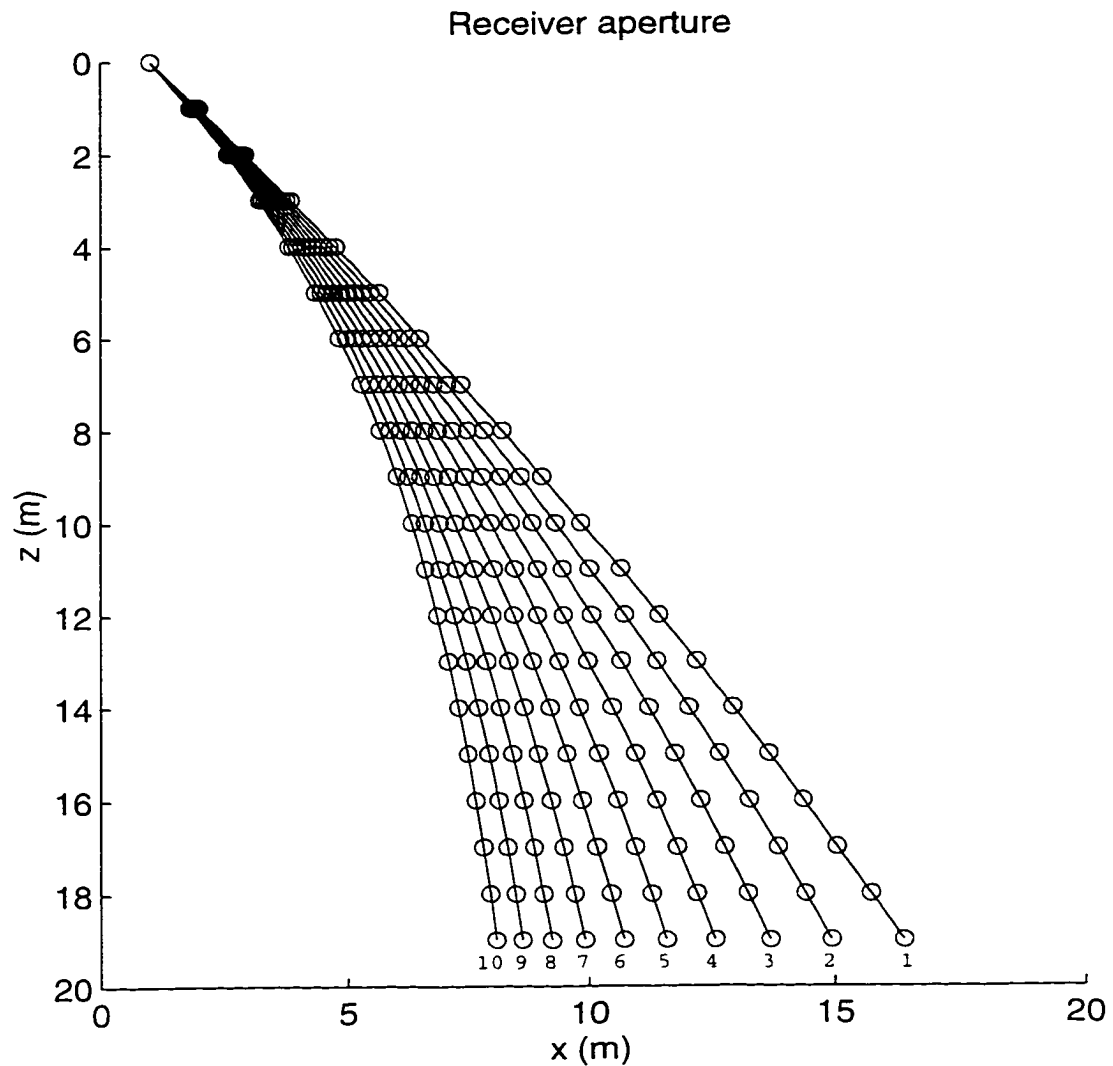
Figure 2.12: Illustration of different deviated receiver apertures: Ten different receiver apertures are used to simulate deviated wells. The sampling interval is irregular due to the deviations as indicated from curve 1 to curve 10. Circle symbols represent receiver positions.
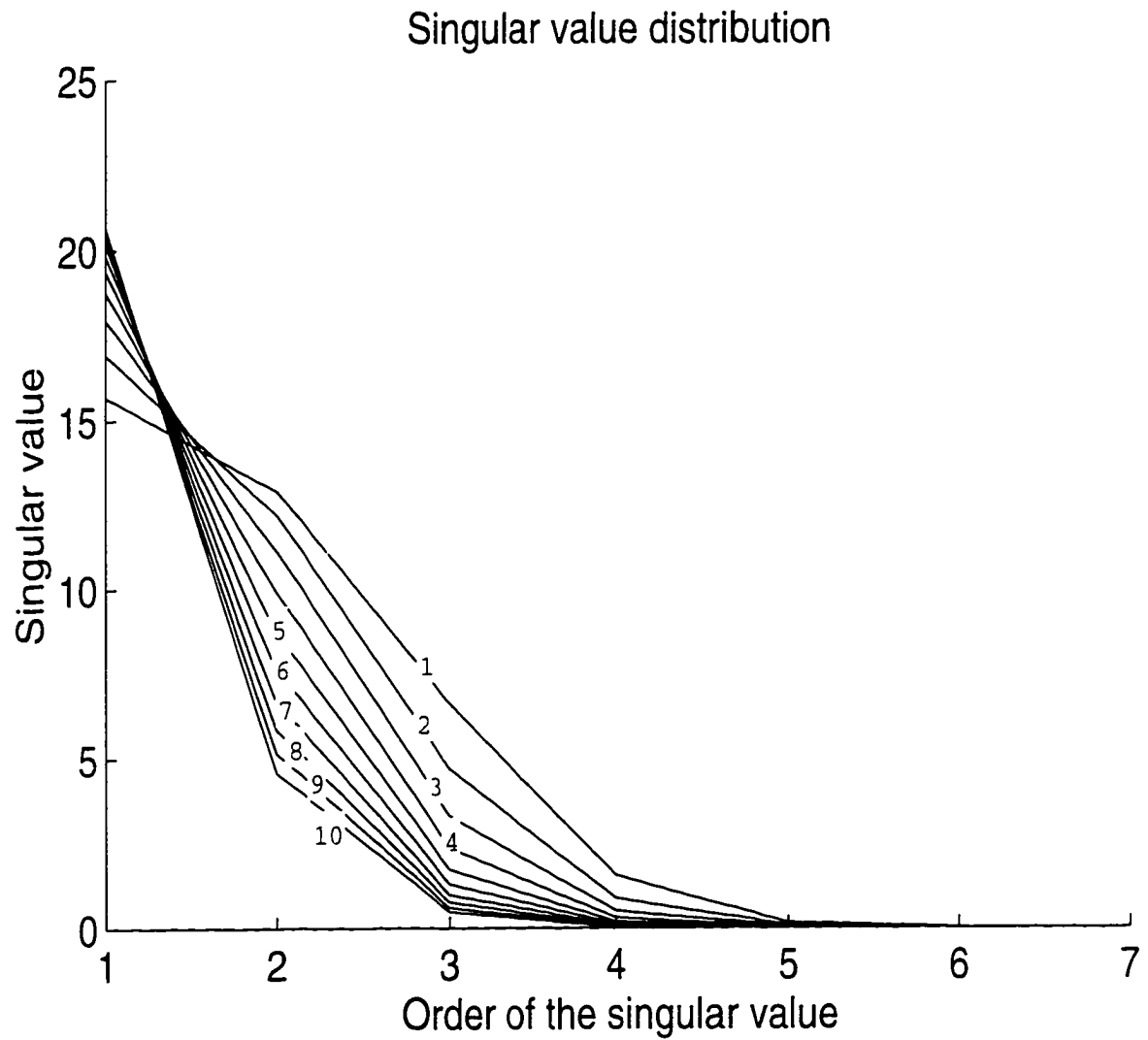
Figure 2.13: Effects of irregular receiver aperture on model resolution: the distribution of the normalized singular values of operator $\mathcal{R}_d$. The first singular value of the resolution matrix increases and the drop-off of the singular values becomes steeper (from curve 1 to curve 10).

condition. With the introduction of wave equation methods by Claerbout (1971), the backprojection methods were largely replaced by backpropagation methods.

With multidimensional linearized inversion (Born inversion), the imaging problem is recast from that of extrapolating a scattered wavefield to one of recovering the perturbations of medium parameters that gave rise to the scattered field. The ability to separate incident field and scattered field enables the inverse scattering problem to have a unique solution given complete measured data and complete angular spectrum of incident wave (Hoenders, 1978). Uniqueness is also obtained when the incident field has a complete set of frequencies (causality requirement).

Addition to the complete measurement, migration or inverse scattering has a unique solution if and on if all evanescent components of the wavefield are zero (or known). The fundamental "problem" caused by the evanescent wavefield is that they do not produce fields which contribute to the measured data, i.e., evanescent field represent a component that can be added to the source term in the wave equation without a corresponding alternation to the fields.

A relationship between the migration and asymptotic inverse scattering is derived in Chapter 4 in which the multifrequency diffraction tomography and migration are essentially the same algorithm.

2.5 Conclusions

The developed scattering operator can be classified as renormalizations in the spatial domain, Fourier domain, and wave asymptotic domain where spatial and Fourier domains are superimposed. The renormalized scattering operator is used to effectively sum the the Born expansion and enable one to decompose the original nonlinear problem into two cascaded linear problems. The extrapolated scattering operator is used to obtain individual diffraction projections independently and then perform the inverse Fourier transformation to obtain the image. The distorted single scattering operator relates scattering data to the spectrum of the inhomogeneity function via asymptotic Fourier transform. The quality of the image reconstructed using a given scattering operator is quantified by means of the temporal and spatial bandwidths

that relate to the size of the smallest details that can be recovered. The resolution also depends on the type of approximation methods applied.

Chapter 3

Inversion of Strong Scattering Media Using Renormalizations

A number of previously intractable problems in several very different areas of physics have been successfully solved using renormalization techniques. Renormalization theory is a broad concept whose content can be understood from various perspectives. It can be viewed as a device that eliminates infinite results in quantum electrodynamics, an up scaling theory in statistical mechanics, or as a regularizing principle in the inverse problems.

To calculate wavefield in the media with strong fluctuations, the first Born approximation is not valid. Rayleigh (1917) designed a renormalization method to generalize the scattering from a thin slab to the scattering from many slabs. This chapter extends the first Born approximation by replacing the total fields in the scattering integral with the renormalized or rescaled incident field. This can be achieved either in spatial domain or in wave spectral domain. These algorithms can be applied to wave field modeling with reasonable accuracy and to inversion of the complex media with the same efficiency as that of conventional diffraction tomography using the first Born approximation.

36

3.1 Wavefield renormalization

In this section, starting from the scattering formalism, I explore the renormalization or rescaling schemes to simplify the scattered wavefield modeling and inversion. The integral representation of the scalar wave equation is expressed as

$$\mathcal{U} = \mathcal{U}_0 + \mathcal{G}\mathcal{M}\mathcal{U}, \tag{3.1}$$

where the symbols $\mathcal{U}$, $\mathcal{U}_0$, $\mathcal{G}$ and $\mathcal{M}$ stand for the total field, incident field, Green's function and medium perturbation function operators (e.g., matrices), respectively. Their ordering is important and cannot be altered at will (see Chapter 2). In the operator notation, Equation (3.1) is valid regardless of whether $\mathcal{U}$, $\mathcal{G}$ and $\mathcal{M}$ are in the spatial domain representation or in the spectral domain representation.

The exact solution to equation (3.1) is intractable for it has hardly any rigorous mathematical foundations. The appropriate method, for practical purposes, is to treat the multiple scattering, i.e., the nonlinear terms, as a perturbation and look for a power series expansion in terms of the perturbation function $\mathcal{M}$ that represents the inhomogeneity in the media. That is

$$\mathcal{U} = \mathcal{U}_0 + \mathcal{G}\mathcal{M}\mathcal{U}_0 + \mathcal{G}\mathcal{M}\mathcal{G}\mathcal{M}\mathcal{U}_0 + \dots . \tag{3.2}$$

which is obtained by iterating on $\mathcal{U}$. For the small perturbation, i.e., for low frequency and weak contrast, expansion (3.2) converges in low orders. For strong fluctuations, however, when the strength of the expansion parameter $\mathcal{M}$ is of an order larger than one, the expansion does not converge at all. Physically, those secular terms of the expansion, represent highly Intuitively, we may rescale or renormalize the incident field such that some of the effects of the multiple scattering are included in the renormalized incident field. In terms of rescaled incident wave, wave field modeling and inversion in a strong inhomogeneity medium are simplified.

Formally, we can express the concept of the renormalization as

$$\mathcal{U} = (\mathcal{I} - \mathcal{G}\mathcal{M})^{-1}\mathcal{U}_0, \tag{3.3}$$

which is an alternate form of equation (3.1). This means that the total field is expressed as a rescaled incident field. The effects of nonlinearity resulting from strong scattering are included in the modified incident field. To actually achieve such renormalization, approximations have to be made to decouple the quantities involved in equation (3.1).

Before proceeding to the renormalization techniques, some explanation should given why the equation (3.1) or (3.2) is not convergent in general and there are two reasons for this. The equation (3.2) may not satisfied the causality condition in a general situation and it may divergent even without the expansion. The second source of the divergent of the equation (3.2) is because of the the expansion in terms of the power of the perturbation function m or multiple scattering. For a causal time waveform initiated at $t = 0$, its spectral characteristics must meet certain requirements so that complete time cancellation occurs for $t < 0$. The requirements are 1) the spectral are square-integrable along the real axis, 2) the spectral are analytic on the upper half-plane and their real and imaginary parts are related by Hilbert transforms (Titchmarsh, 1948). For some simple models[1] the Kramers-Kronig relation is strictly

---

[1] Consider a scattering by a spherical target of radius a
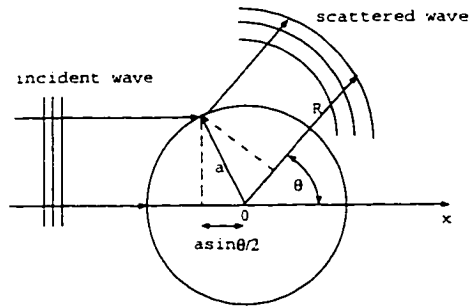
The total wavefield can be written as

$$u = u^p(t - x/v) + u^s(t - R/v) = \int U^p(\omega)e^{-i\omega(t-x/v)}d\omega + \int U^s(\omega)\frac{e^{-i\omega(t-R/v)}}{R}d\omega$$

The causality implies that the scattered wave front can not reach the distance R until $vt \geq R - 2a\sin\theta/2$. The term $-2a\sin\theta/2$ is present because the shortest path for the scattered wave to reach the radial distance R is $2a\sin\theta/2$ shorter that the path going through the center as illustrated in the figure. In terms of the Fourier transforms, the statement of causality becomes that $U^p(\omega)$ is analytic

held and the relation between the real and imaginary parts of the wavefield spectral can be determined. Consequently, the causality is guaranteed. However, for the scattering of general inhomogeneities the causality condition in frequency may be weaken and even broken. This is primarily due to the fact that the incident and scattered wave are complicated functions of ω and this could result the divergence of (3.1).

Another source of the divergence of (3.1) is due to the mathematical technique to solve the Fredholm integral equation of the second kind. It can be proven, the series (3.2) is convergent only on the condition of small perturbation assuming the causal condition is satisfied. For example, the integral equation (3.1) can be solved using the method of successive approximations, as shown in (3.1). [2] The error by taking only the linear term of the λ, i.e., the single scattering approximation, is is given in Appendix A. In later sections, we will present the algorithms derived using specific approximations.

3.2 Localized approximation

To decouple the nonlinearity involving the field and the medium perturbation function, we first consider a single scatterer or a localized scatterer cluster. Under the

---

on the upper half ω-plane implies that $U^s(\omega)e^{2ia\omega/v\sin\theta/2}$, for fixed θ, is analytic on the upper half ω-plane. For $\theta = 0$ Kramers-Kronig relation reduces to the forward dispersion relation which gives the real part of the forward scattered field in terms of the imaginary part. For $\theta \neq 0$, the dispersion relation becomes less useful since the real and imaginary parts of $U^s(\omega, \theta)$ will be mixed due to the exponential factor. This can be considered as a weakening of the causality condition.

[2]Substituting this series in equation (3.1) and equating the coefficients of powers of λ, one obtains

$$U_1(\mathbf{y}) = \int m(\mathbf{x})G(\mathbf{x},\mathbf{y})U_0(\mathbf{x})d\mathbf{x}$$

$$U_2(\mathbf{y}) = \int m(\mathbf{x})G(\mathbf{x},\mathbf{y})U_1(\mathbf{x})d\mathbf{x}$$

$$\vdots$$

$$U_n(\mathbf{y}) = \int m(\mathbf{x})G(\mathbf{x},\mathbf{y})U_{n-1}(\mathbf{x})d\mathbf{x}$$

From these equations there may successively be determined all the function $U_1, U_2, ...$, explicitly. It can be proved the series will be uniformly convergent for the integral kernel $m(\mathbf{x})G(\mathbf{x},\mathbf{y}) \leq M$, where M is a bound, if λ satisfies $|\lambda| < 1/(MD)$ where D is the diameter of the scattering volume.

first Born approximation, the total field at the vicinity of the scattering center can be written as

$$u(\mathbf{x}, \mathbf{s}) = u_0(\mathbf{x}, \mathbf{s}) + u_0(\mathbf{x}, \mathbf{s}) \int_v m(\mathbf{y}) G(\mathbf{x}, \mathbf{y}) d\mathbf{y} \qquad (3.4)$$

where u and u_0 are the total field and incident field respectively; $m(\mathbf{x})$ is the reduced perturbation function representing the scatter (see Chapter 2); G is the Green's function; and v is the volume of the scatterer or scatterer cluster. An argument in favor of this approximation is that, with the singular nature of $G(\mathbf{x}, \mathbf{y})$ at $\mathbf{x} = \mathbf{y}$, the dominant contribution to the integral comes from points in the vicinity of $\mathbf{x} = \mathbf{y}$. Therefore, the error of the approximation

$$\int_v m(\mathbf{y}) G(\mathbf{x}, \mathbf{y})(u_0(\mathbf{x}, \mathbf{s}) - u_0(\mathbf{y}, \mathbf{s})) d\mathbf{y}.$$

is small and can be ignored. The validity of the local nonlinear approximation is shown in figure 3.1.
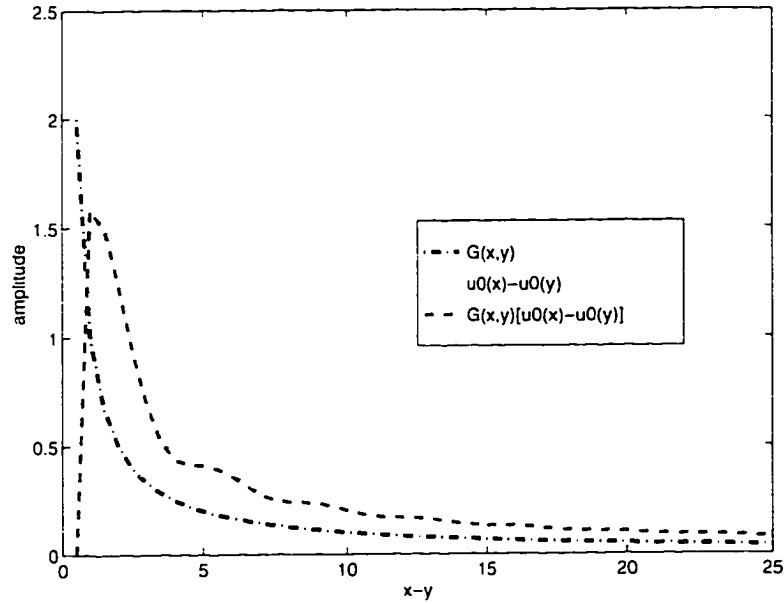

Figure 3.1: The validity of local nonlinear approximation: the dominant contribution to the scattering integral comes from points in the vicinity of singularity of the Green's function.

For a problem involving many scatterers, the contributions of the multiple scattering may be significant and cannot be neglected. Analogous to Rayleigh's renormalization [3], we recast equation (3.4) into the following form.

$$u(\mathbf{x}, \mathbf{s}) \equiv \frac{u_0(\mathbf{x}, \mathbf{s})}{1 - \mathcal{L}}, \tag{3.5}$$

where $\mathcal{L} = \int_s m(\mathbf{y}) G(\mathbf{x}, \mathbf{y}) d\mathbf{y}$. The rationale to recast equation (3.4) in such a form is that the secular terms of the divergent series, or, high order terms representing multiple scattering,

$$(1 + \mathcal{L} + \mathcal{L}\mathcal{L} + ...) u_0,$$

can be effectively summed. Notice that the above divergent series is similar to the divergent series

$$(\mathcal{I} + \mathcal{G}\mathcal{M} + \mathcal{G}\mathcal{M}\mathcal{G}\mathcal{M} + ...) \mathcal{U}_0,$$

except that the latter involves operators and has its coupling embedded.

Substituting the approximated total field into the scattering integral, the scattering problem can be modified as

$$U(\mathbf{s}, \mathbf{r}) \approx \int m(\mathbf{x}) R(\mathbf{x}) G(\mathbf{x}, \mathbf{s}) G(\mathbf{r}, \mathbf{x}) d\mathbf{x}, \tag{3.6}$$

where $R(\mathbf{x}) = (1 - \mathcal{L}(\mathbf{x}))^{-1}$ is called the renormalization function, and the incident field is replaced by the Green's function G. While in the first Born approximation the total field u is replaced by the incident field u_0, here the total field is approximated with a rescaled or renormalized incident field $u_0 R$. The improved approximation has less limitation in terms of strength of the scattering since some of the multiple scattering is taken into account by the renormalization function R, as sketched in figure 3.2. This technique is appropriate for the localized inhomogeneity. For arbitrary inho-

---

[3]Rayleigh developed a renormalization scheme to generalize the scattering from a thin slab to scattering from many slabs. He obtained an expansion of the form $u = e^{ik_0 x}(1 + ik_0 n x)$ for the first scattering from one slab, where $k_0 n x \ll 1$ and n is refraction index. To obtain a solution valid for many slabs, he recasted this expansion into an exponential form, i.e., $u = e^{i(k_0 + k_0 n)x}$. In this manner he effectively summed the sequence $\sum_{m=1}^{\infty} (ik_0 n x)^m / m!$.
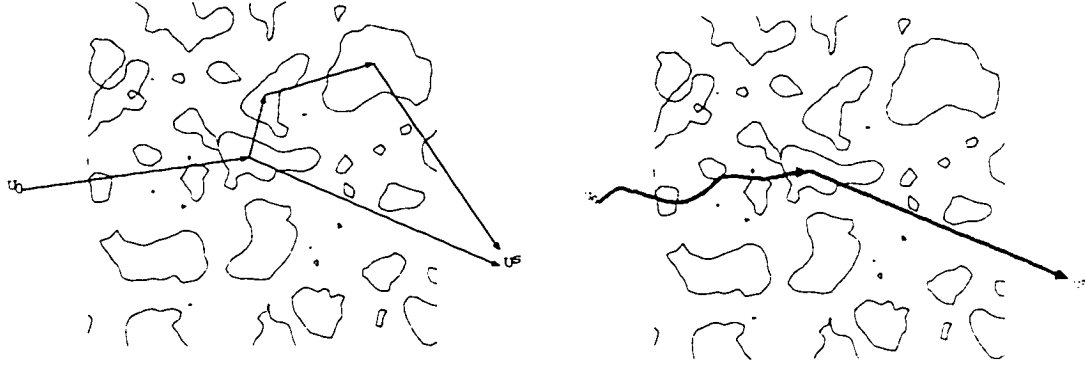
Figure 3.2: Illustration of renormalization: the left panel show intractable multiple scattering; and the right panel depicts that some of the multiple scattering can be taken into account by modified incident waves.

mogeneities, further approximations are necessary, such as the static approximation. (Habashy, 1992).[4]

3.2.1 Application to the wavefield modeling

A well defined disk model is used to demonstrate the validity of the renormalization algorithm in terms of the contrast of the inhomogeneity, and the frequency of the wavefield. Usually, these two factors are the sources that cause the first Born approximation to fail. The background velocity of the model is kept constant at $3500m/s$, frequency at $350Hz$, while the velocity of the sphere is varied. The distance between the source and receiver is $100m$. A disk of $10m$ in diameter is located between the source and receiver. The wave field of a disk model is calculated by using the first Born approximation, the renormalization algorithm and the moment method,[5] respectively. In Figure 3.3, we compare the results of three different methods. One can see that the renormalization method provides acceptable estimations compared

---

[4]Assuming the total field is static, Habashy obtained

$$u(\mathbf{x},\mathbf{s}) = u_0(\mathbf{x},\mathbf{s}) + u(\mathbf{x},\mathbf{s}) \int m(\mathbf{y})G(\mathbf{x},\mathbf{y})dy$$

It can be rearranged such that $u(\mathbf{x},\mathbf{s}) = (1 - \int m(\mathbf{y})G(\mathbf{x},\mathbf{y})dy)^{-1} u_0(\mathbf{x},\mathbf{s})$.

[5]The moment method is often applied in calculation of the scattered field. The scattering region is divided into N square cells and wavefield and the inhomogeneity are represented as a summation

to the solution achieved by the moment method regardless of the velocity contrast. The Born approximation, on the other hand, is invalid except when the velocity perturbation is within ten percent.

Figure 3.3: Comparison of wavefield amplitudes calculated using the moment method, the first Born approximation and renormalization over a sphere model with different velocity contrast.

The accuracy of wavefield modeling using the renormalization method with regard to frequency variations is examined. The model is the same as in the previous example. The velocity perturbation is fixed at 50 percent of the background. Figure 3.4 shows that the amplitude calculated using the renormalization method is consistent with the solution by the moment method regardless the the range of the frequency variations, while the result of the first Born approximation is only acceptable at lower end of the frequency range and begins to break down at $200Hz$.

---

of basis functions over the N cells, i.e.,

$$m(r) = \sum_{i,j} e(r_{ij})b_{ij}; \quad u(r) = \sum_{i,j} a(r_{ij})b_{ij}$$

where b_{ij} is the basis function, e_{ij} and a_{ij} represent the coefficients describing the inhomogeneity function and wavefield over the basis function. Usually a pulse basis function is chosen (Chew, 1990) and the scattering integral can be written as a linear algebra system.
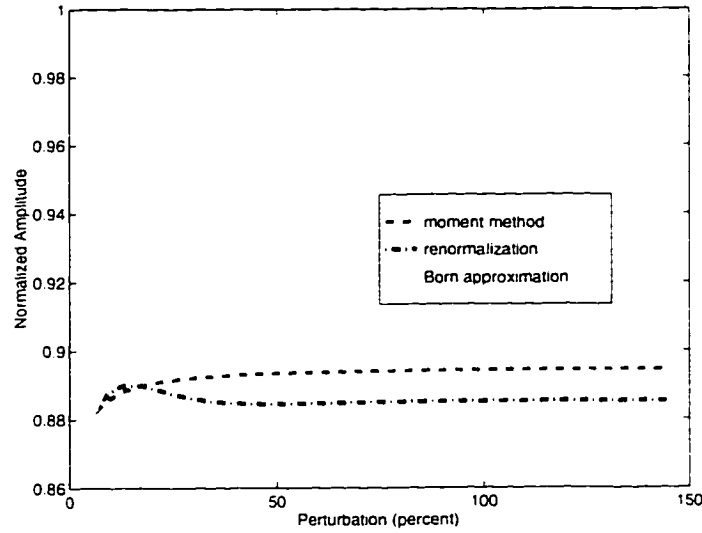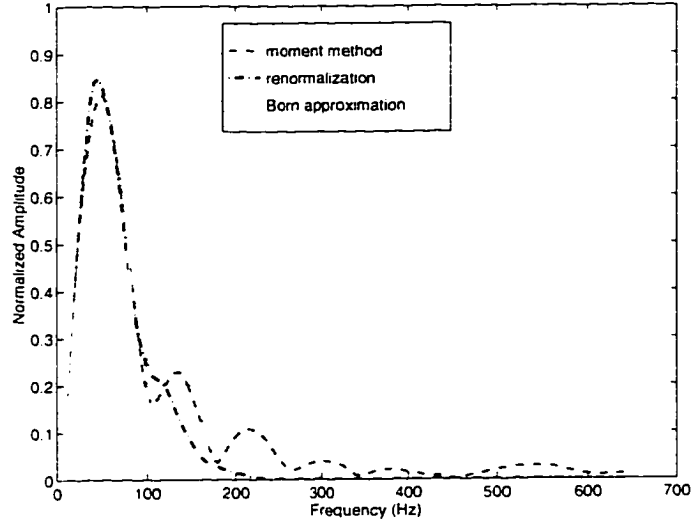
Figure 3.4: Comparison of wavefields calculated using the moment method, the first Born approximation and renormalization over a sphere model with frequency variations, the perturbation contrast is fixed at 50 percent.

In figure 3.5, we show time sections of the wavefield over a two layer model. Again the calculations are carried out using the moment method, renormalization and the first Born approximation and renormalization. Through this comparison, we can see that the amplitudes of the scattered field by the moment method and renormalization are stronger than that achieved by the first Born approximation.

3.2.2 Application to the inversion

If the combination $m(\mathbf{x})R(\mathbf{x})$ is treated as a new variable $D(\mathbf{x})$, then the conventional diffraction tomographic procedure can be applied to invert the variable $D(\mathbf{x})$ as described in Appendix A. The perturbation function itself can be evaluated through equation

$$D(\mathbf{x}) = m(\mathbf{x})(1 - \int m(\mathbf{y})G(\mathbf{x},\mathbf{y})d\mathbf{y})^{-1}. \tag{3.7}$$

To test the algorithm, the first example is to invert a simple model of five diffractors. The scattering field is calculated using the moment method. The model and
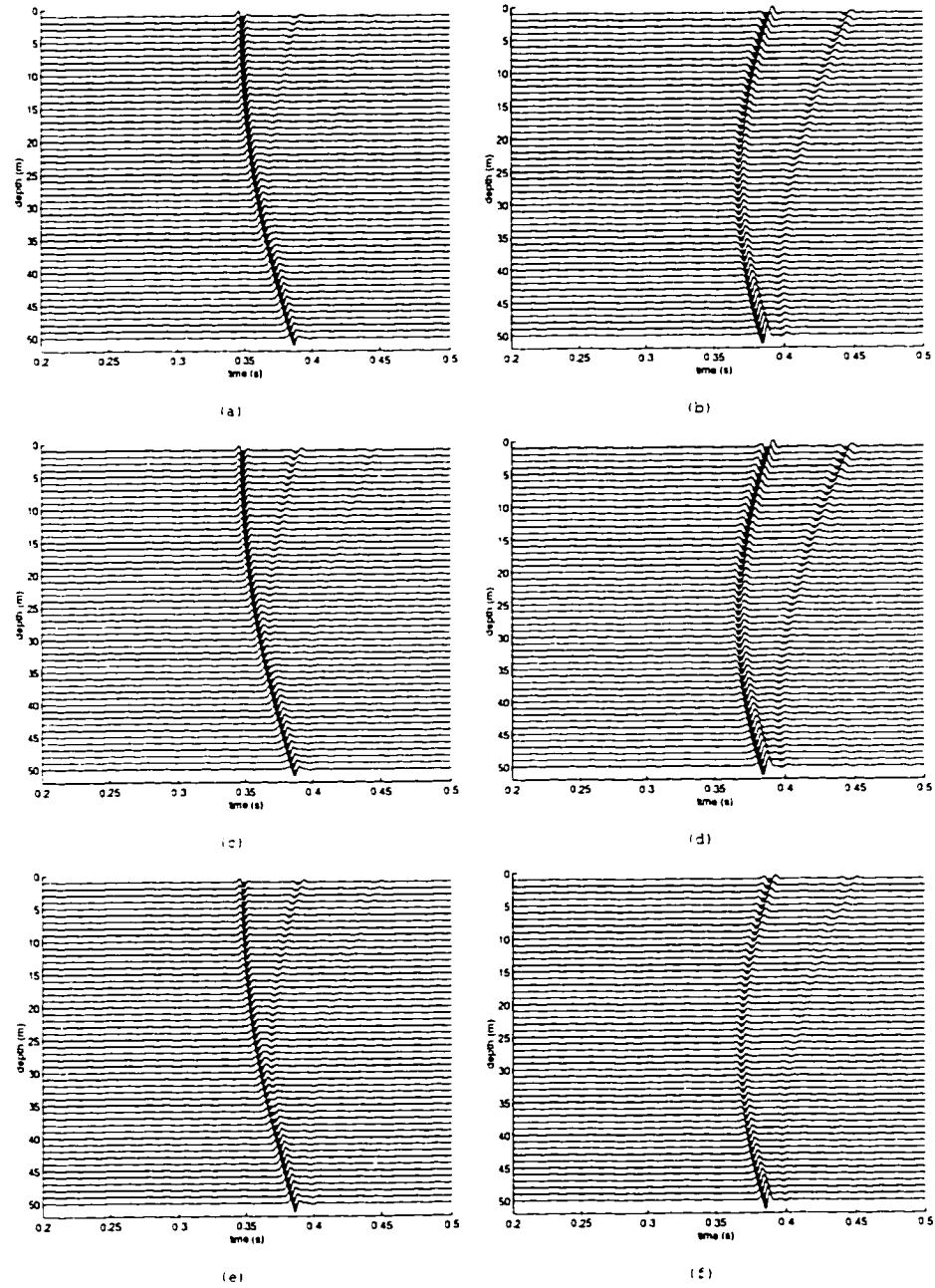
Figure 3.5: The comparison the wavefield by the moment method (top panel), renormalization (middle panel), and the first Born approximation (bottom panel) over a two layer model: (a), (c), and (e) are total fields; (b), (d), and (f) are scattered fields.

the field are shown in figure 3.6. Figure 3.7 shows the inversion results using the first Born approximation and the renormalization method, respectively.
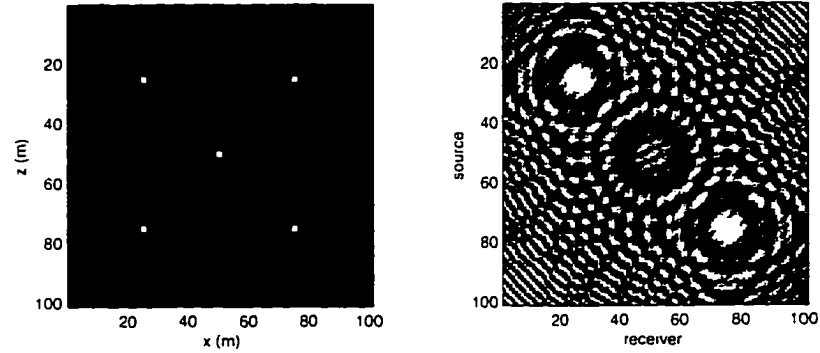
Figure 3.6: Diffractor model and the scattered field: the left panel is the model with five diffractors; the right panel is the real part of the scattered field calculated using the moment method.
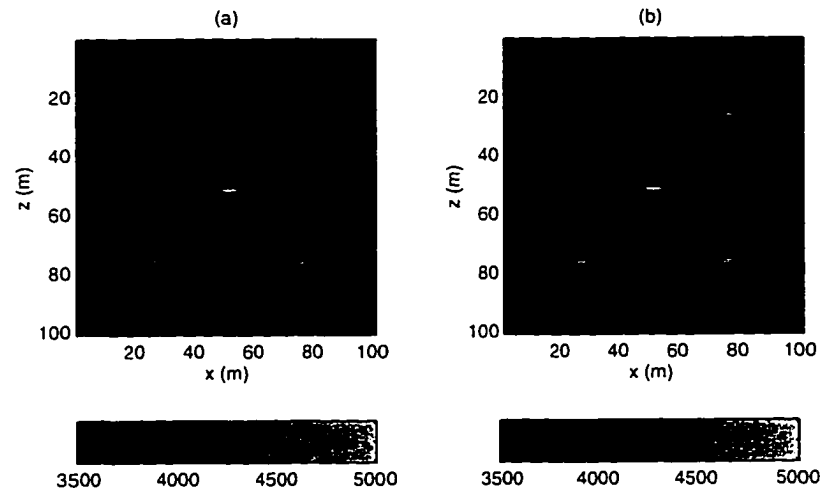
Figure 3.7: Reconstructed image: panel (a) and panel (b) are the inversions using the renormalization and the first Born approximation, respectively. The average absolute differences are 6.7 between the model and (a), and 21.3 between the model and (b).

The two images essentially are the same except that the intensity of the off center diffractors is more balanced relative to the center diffractor in the image recovered using the renormalization. This is expected for the isolated diffractors since the first Born approximation is valid.

In the next numerical example, an inversion is conducted on the synthetic data of a complicated model of three fractures. Figure 3.8 displays the model and the wavefield. The velocity of the background and inhomogeneity (fractures) is $3500m/s$ and $4500m/s$, respectively. The wavefield is calculated using the moment method at the frequency of $500Hz$. Figure 3.9 shows inversions using the renormalization and the
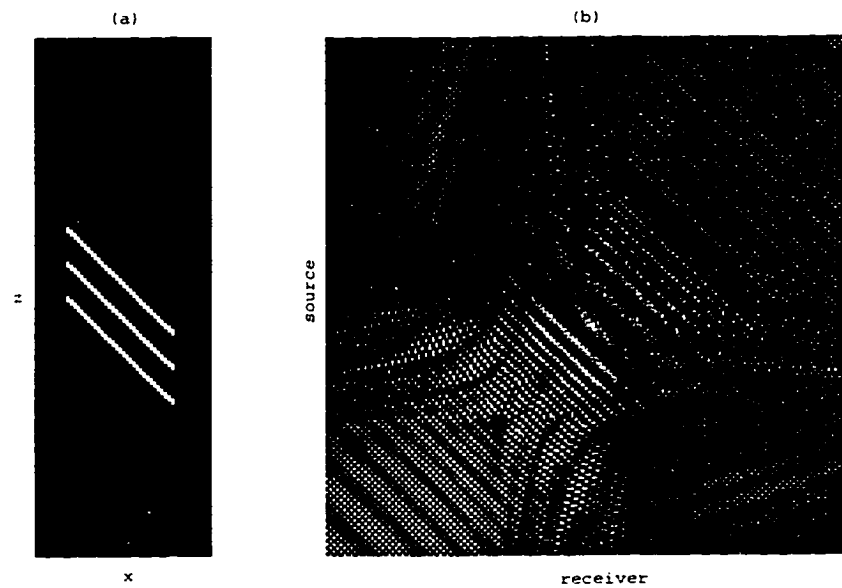
Figure 3.8: (a) is the model of three fractures and (b) is the wavefield of the single frequency at 500 Hz.

first Born approximation. The reconstruction recovering the strength of inhomogeneity using the renormalization is better than that of using the first Born approximation. The average absolute difference between the model and the reconstruction using the first Born approximation, and between the model and the reconstruction using the renormalization is 72.8 and 19.4, respectively.

We also apply the algorithm to field data from the McElroy reservoir in west Texas. See Harris et al. (1995) for a description of the site, geology, and data acquisition. A typical common receiver gather is plotted in figure 3.10a and the data is recorded at 202 receiver and 202 source locations. The amplitudes of the wave field are normalized relative to the one at the nearest offset 3.10(b). For convenience, the source line and receiver line are padded with zeros to form a 256 by 256 matrix and then Fourier
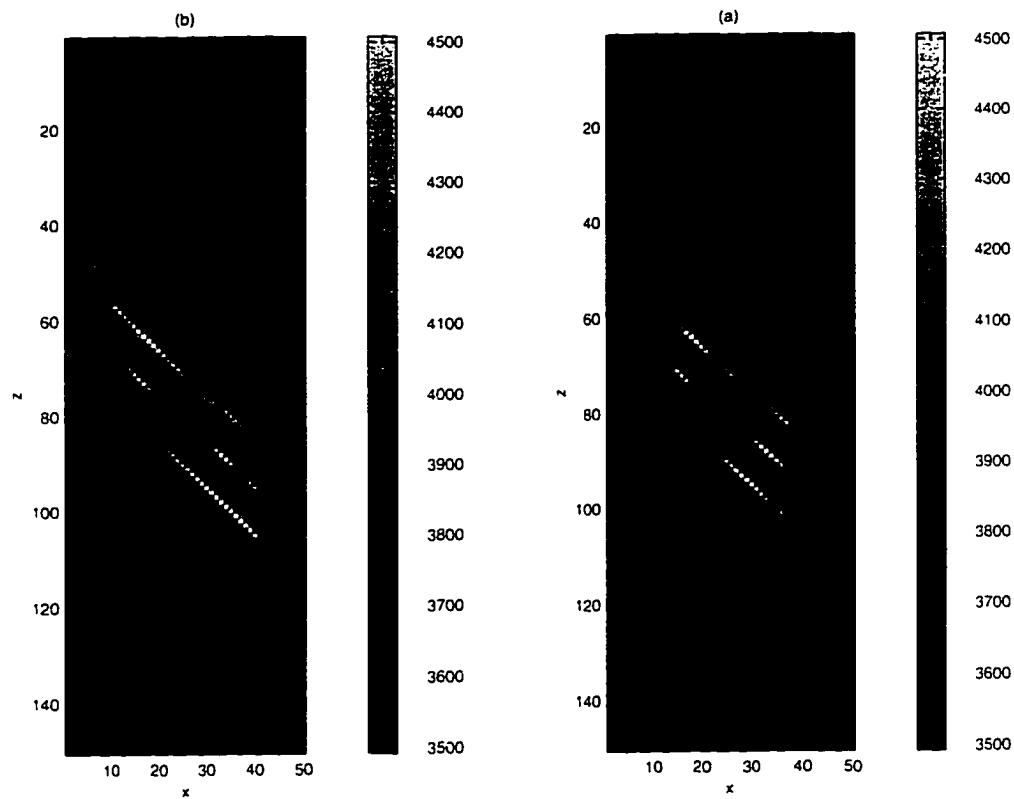
Figure 3.9: Comparison the renormalization with the first Born approximation inversions on a model with three fractures. Panel (a) is the inversion using the first Born approximation and panel (b) is from the renormalization inversion. The average absolute difference between the model and the inversion using the first Born approximation, and between the model and the inversion using the renormalization is 72.8 and 19.4, respectively.

transformed to the wave number domain as shown in figure 3.10c.

The near-offset images are reconstructed with wavefield at 1000 Hz. The results are shown (Figure 3.11) in terms of structure, the diffraction tomograms reconstructed using the renormalization and the first Born approximation methods have no significant difference. However, in terms of strength of the inhomogeneity, the diffraction tomogram reconstructed using renormalization have higher contrast of the inhomogeneity (up to 7 percent). Notice that because, in this example, we want only to show the algorithm is working and did not perform any processing on the data set, and the results may not be optimal.
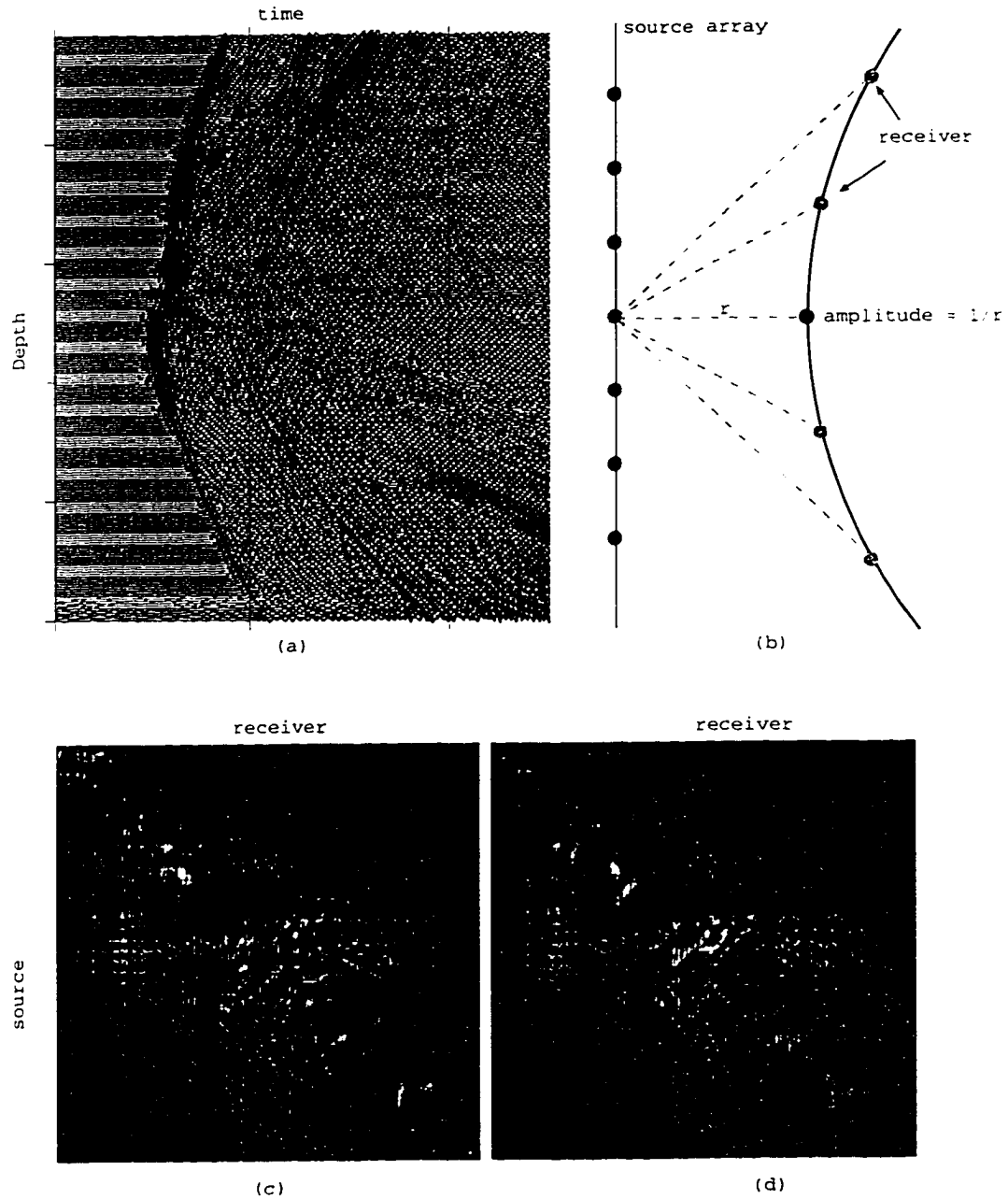
Figure 3.10: McElroy near offset data: (a) a typical common source gather from McElroy near offset survey, (b) the amplitude of the wave field at the zero offset is normalized to a geometrical spreading factor $1/r$, and (c) and (d) are the real and imaginary parts of the wave field at $1250Hz$, respectively.
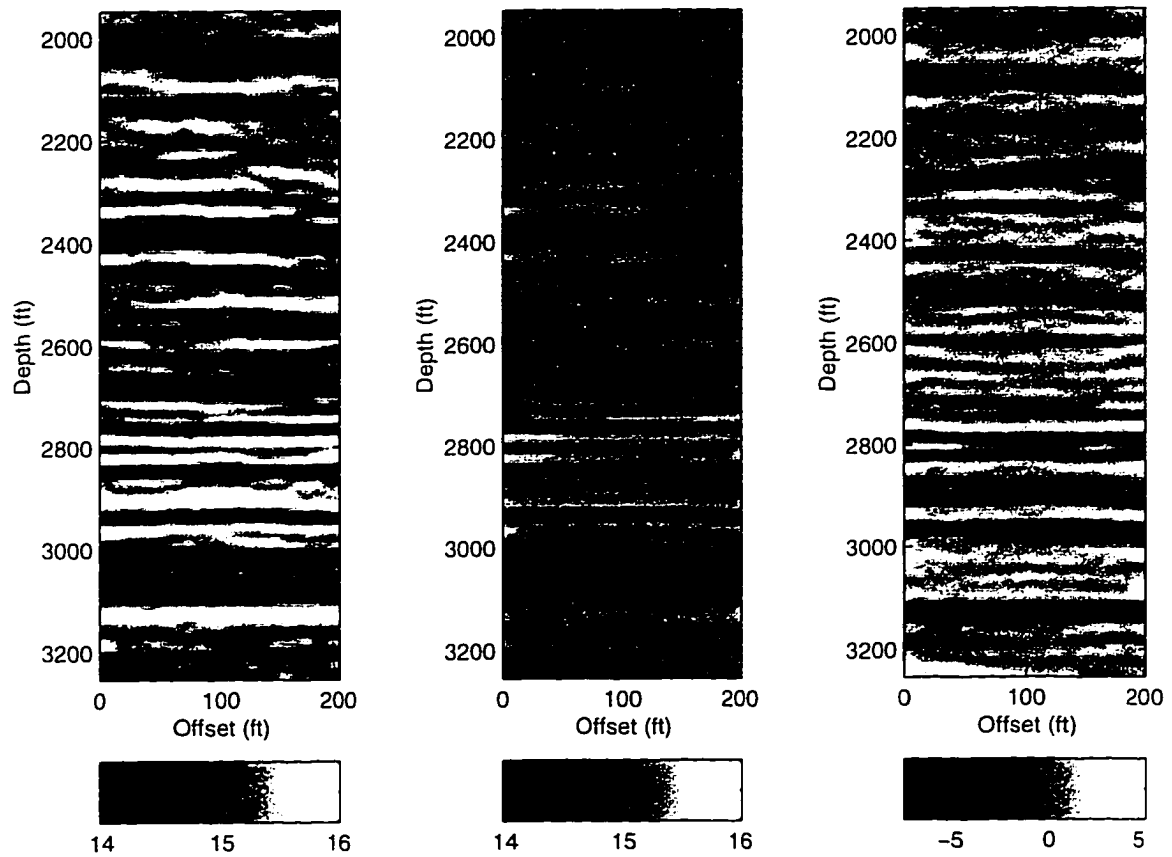
Figure 3.11: The reconstruction of McElroy near offset data. The left panel is reconstructed with renormalization; The middle panel is reconstructed with the first Born approximation; and the right panel is their relative difference in percentage. The unit of the velocity is in Kft/s.

3.3 Back-propagation in the spectral domain

In the previous section, we discussed the localized renormalization in the spatial domain. Such a method is limited to situations where the inhomogeneity is not localized. As a complement to the localized spatial renormalization, the wave fields may be back-propagated directly in the spectral domain to obtain the diffraction projections. The inversion is carried out efficiently by taking advantage of the Fourier transform.

3.3.1 Spectral representation

The integral representation of scattered fields can be rewritten as two parts, i.e.,

$$U(\mathbf{r}, \mathbf{s}) = \int m(\mathbf{x})G(\mathbf{r}, \mathbf{x})(G(\mathbf{x}, s) + U(\mathbf{x}, s))d\mathbf{x}, \qquad (3.8)$$

where U is the scattered field; m is the reduced perturbation function representing inhomogeneity in the medium; and G is the Green's function. The second term on the right hand of the equation (3.8) represents the multiple scattering which is responsible for the nonlinear effects of the interaction between the scatterer and scattered waves, as indicated in figure 3.12.
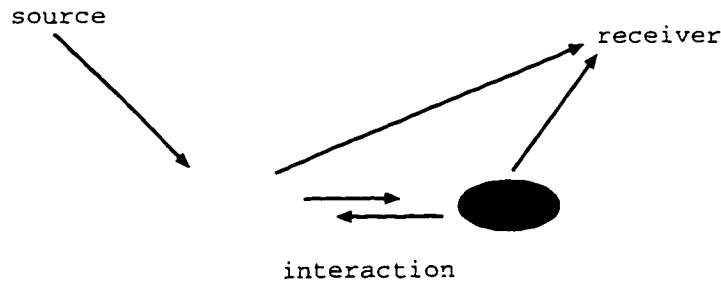
Figure 3.12: Illustration of multiple scattering.

For multi-source and multi-receiver configurations, we may perform the Fourier transform of the scattered field along the source array and receiver array. Then, the

counterpart of equation (3.8) in wavenumber domain is:

$$U(\mathbf{k}_r, \mathbf{k}_s) = \int m(\mathbf{x})G(\mathbf{k}_r, \mathbf{x})(G(\mathbf{x}, \mathbf{k}_s) + U(\mathbf{x}, \mathbf{k}_s))d\mathbf{x}, \qquad (3.9)$$

where $U(\mathbf{k}_r, \mathbf{k}_s)$ is the spectrum of the scattered field, $\mathbf{k}_s$ and $\mathbf{k}_r$ are the incident wave vector and scattered wave vector, respectively. In general, equation (3.9) can be arranged such that it is a Fourier transform of the perturbation function m, i.e.

$$U(k_r, k_s) = A(\mathbf{k}_r, \mathbf{k}_s) \int_v m(\mathbf{x})e^{-i(\mathbf{k}_r - \mathbf{k}_s)\cdot\mathbf{x}}d\mathbf{x} + B(k_r) \int_v m(\mathbf{x})U(\mathbf{x}, k_s)e^{-i\mathbf{k}_r\cdot\mathbf{x}}d\mathbf{x}.$$

$$(3.10)$$

where $A(\mathbf{k}_r, \mathbf{k}_s)$ and $B(k_r)$ are the functions resulting from plane wave decomposition of the spherical or cylindrical waves.[6]

3.3.2   Nonlinear diffraction projections

As in the case of the phase shift migration (Gazdag and Sguazzero, 1978), the scattering field at the receiver location is back-propagated to arbitrary locations, i.e. to

---

[6]For a two dimensional problem, the Green's function in equation (3.8) is the first kind and zero order Hankel function, i.e.,

$$G(\mathbf{x}, \mathbf{s}) = \frac{i}{4}H_0^{(1)}(k|\mathbf{x} - \mathbf{s}|), \qquad G(\mathbf{g}, \mathbf{x}) = \frac{i}{4}H_0^{(1)}(k|\mathbf{g} - \mathbf{x}|).$$

The spectra of the Hankel function along the source line and receiver line are

$$G(\mathbf{x}, k_s) = \frac{i}{4\gamma_s}e^{(i\gamma_s x_s + ik\hat{s}\cdot\mathbf{x})}, \qquad G(k_r, \mathbf{x}) = \frac{i}{4\gamma_s}e^{(-i\gamma_r x_r - ik\hat{r}\cdot\mathbf{x})},$$

which are in the form of plane waves. Where $\gamma_r = \sqrt{k_0^2 - k_r^2}$ and $\gamma_s = \sqrt{k_0^2 - k_s^2}$. After plane wave decomposition, the spectrum representation of equation (3.9) take the form of

$$U(k_r, k_s) = A(k_s, k_r) \int m(\mathbf{x})e^{-i[(\gamma_g - \gamma_s)x + (k_s + k_r)z]}dxdz + B(k_r) \int U(\mathbf{x}, k_s)e^{-i(\gamma_g x - k_r z)}dxdz.$$

where $A = -exp(-i\gamma_r x_r + i\gamma_s x_s)/16\gamma_r\gamma_s$, and $B = exp(-i\gamma_r x_r)/4\gamma_r$.

express $U(\mathbf{x}, \mathbf{k}_s)$ in terms of $U(\mathbf{k}_r, \mathbf{k}_s)$. In general, the spatial filter is given as

$$
H(\mathbf{k}; \mathbf{x}) = \left\{ \begin{array}{ll} e^{i\mathbf{k}\cdot\mathbf{x}} & \text{for } k_x^2 + k_y^2 + k_z^2 = k_0^2, \\ 0 & \text{otherwise,} \end{array} \right.
$$

With the continuation process, the scattered wavefield at a arbitrary location is expressed in terms of the scattered wavefield at the boundary, i.e.,

$$
U(\mathbf{x}, \mathbf{k}_s) = \frac{1}{2\pi} \int U(\mathbf{k}_s, \mathbf{k}_r) H(\mathbf{k}_r, \mathbf{x}) d\mathbf{k}_r. \tag{3.11}
$$

where $U(\mathbf{k}_s, \mathbf{k}_r)$ is the wavefield spectrum at the received locations. By noticing that the integrals on the right side of equation (3.10) are Fourier transforms and substituting (3.11) into (3.10), we have

$$
U(\mathbf{k}_r, \mathbf{k}_s) = AM(\mathbf{k}_r - \mathbf{k}_s) + \frac{B}{2\pi} \int U(\mathbf{k}', \mathbf{k}_s) M(\mathbf{k}' - \mathbf{k}_s) d\mathbf{k}'. \tag{3.12}
$$

where $\mathbf{k}' \subset \mathbf{k}_r$. Equation (3.12) is recognized as a convolution integral equation for the transform of the perturbation function in terms of the measured scattering field. Equation (3.12) is more manageable than the integral equation (3.8) in the spatial domain.

Notice that when the strength of the scatterer is weak, only the first term on the right side of the equation (3.12) is taken into the consideration, which is the case of the first Born approximation. However, when multiple scattering is strong, the convolution integral in equation (3.12) cannot be ignored and the linear relation under the first Born approximation is not adequate.

It can be shown that, in equation (3.12), $M(\mathbf{k}_r - \mathbf{k}_s)$ is a single diffracted projection for a fixed wavenumber $\mathbf{k}_s$, which is independent to other projections of different wavenumber $\mathbf{k}_s$ and can be solved independently.

For a fixed $\mathbf{k}_s$, the above linear system can be solved for one trace of the spectrum of the object function M as indicated in figure 3.13a. With a Jacobean transformation, the above linear trace of object spectrum in $(\mathbf{k}_g - \mathbf{k}_s)$ becomes a curve in (k_x, k_y, k_z) domain (see figure 3.13b).
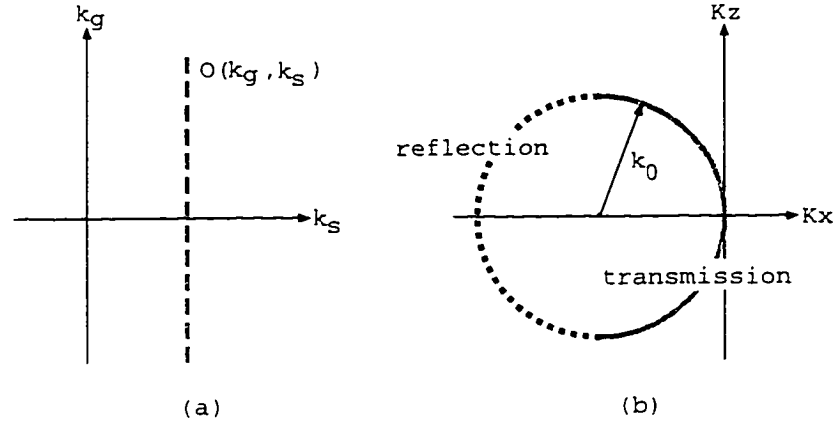
Figure 3.13: Nonlinear diffraction projection: (a) is the projection in (k_g, k_s) domain, and (b) shows the projection in (K_x, K_z) domain

The discrete form of equation (3.12) can be written as

$$U(\mathbf{k}_r, \mathbf{k}_s) = AM(\mathbf{k}_r - \mathbf{k}_s) + B \sum_i M(\mathbf{k}' - \mathbf{k}_s) \int_i U(\mathbf{k}', \mathbf{k}_r) dk'. \qquad (3.13)$$

where $\int_i U(\mathbf{k}', \mathbf{k}_r) dk'$ is the integral over a pixel volume.[7] The system in equation (3.13) can be rearranged into a Toeplitz type with the matrix elements consisting of the Fourier coefficients of the observed scattered field. i.e.,

$$\begin{pmatrix} 1 - \Phi_0 & \Phi_{-1} & \cdots & \Phi_{-n} \\ \Phi_1 & 1 - \Phi_0 & \cdots & \Phi_{1-n} \\ \vdots & \vdots & \ddots & \vdots \\ \Phi_n & \Phi_{n-1} & \cdots & 1 - \Phi_0 \end{pmatrix}. \qquad (3.14)$$

where

$$\Phi_{k_s - k'} = \frac{B}{2\pi} \int_i U(k_s - k') dk'.$$

---

[7] For a crosswell survey, it can be rewritten as

$$U(\mathbf{k}_s, \mathbf{k}_g) = \frac{e^{i\gamma_g x_g}}{16\gamma_g \gamma_s} M_{\mathbf{k}_s}(\mathbf{k}_g) - \frac{iexp(-i\gamma_g x_g)}{4\pi} \int M(\mathbf{k}') U\mathbf{k}_s - \mathbf{k}', \mathbf{k}_s(\mathbf{k}') dk'.$$

3.3.3 Examples of the inversion

This section illustrates the spectral domain back-propagation method with the numerical examples. In the first example, an infinite cylindrical disk model is considered. which has a analytical solution[8]. The geometry and parameters are shown in figure 3.14.
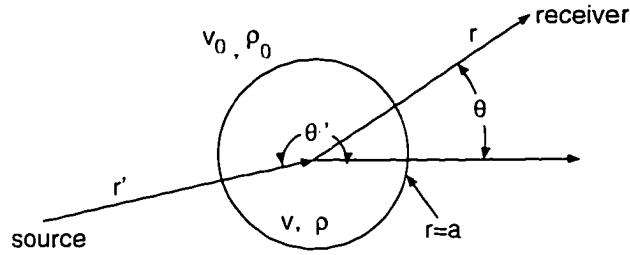
Figure 3.14: Scattering geometry of a cylindrical disk.

Figure 3.15a shows the velocity model used for the two-dimensional experiment. An anomalous circular region 20 m in diameter with a velocity of 5000 m/sec is located at the center of the medium. The background velocity is 3000 m/sec and the frequency is 1000 Hz. The scattered field calculated using the analytical solution of a cylinder is shown in figure 3.15b. We can see that the scattered field is stronger in the forward direction as expected. The difference between the projection obtained by using the first Born approximation and by using the wavefield backpropagation is shown in figure 3.16. One can see that the largest difference (around 10 percent) occurred at the high frequency, which is expected, since the multiple scattering has higher spatial frequency usually.

The inversion is shown in figure 3.17. The shape reconstruction is consistent with

---

[8]That is

$$U(r,\theta) = \frac{i}{4} \sum_n e^{-i(\theta'-\theta)n} H_n^{(1)}(k_0 r') H_n^{(1)}(k_0 r) \frac{C_{out}}{C_i n},$$

where

$$C_{out} = \rho k_0 J_n(ka) \dot{J}_n(ka) - \rho_0 k \dot{J}_n(ka) J_n(k_0 a),$$

$$C_{in} = \rho_0 k H_n^{(1)}(k_0 a) \dot{J}_n(ka) - \rho k_0 \dot{H}^{(1)}{}_n(k_0 a) J_n(ka),$$

and ρ, v, ρ_0, and v_0 is density and velocity of disk and background medium, respectively.
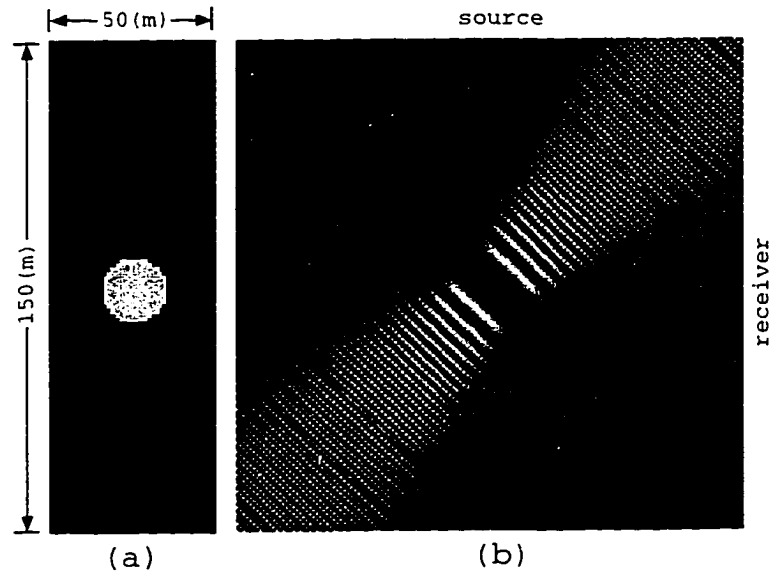
Figure 3.15: Synthetic data modeling using analytical solution: a) an infinite cylindrical disk model; and b) calculated scattered field (real part). Frequency=$1000Hz$.

the model by using both the first Born approximation and nonlinear projections. Note that the disk is elongated in the x direction, both in figure 3.17 b and c, as is expected since the resolution is poorer in that direction for limited source/receiver aperture. However, compared to the result using the first Born approximation, the velocity reconstruction using nonlinear projection algorithm has significantly improved, especially in the middle of the disk (see figure 3.17 c). The average absolute difference between the model and the reconstruction using the first Born approximation is 54.6 while it is 32.4 between the model and the reconstruction using nonlinear projection algorithm.

In the second example, the model, representing fracture zones, has a background velocity of $3000m/sec$ and two linear velocity abnormal features of $5000m/sec$, see figure 3.18a. The moment method is used to generate the wavefield (Wang, 1995). A $50m$ horizontal by $150m$ vertical area is considered with a sampling interval of $0.5m$. Frequency is $1000Hz$. The calculated scattered field (real part) is shown in figure 3.18b.
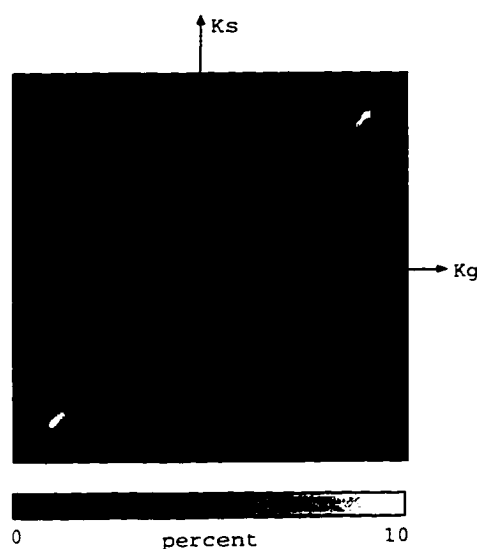
Figure 3.16: The difference of the diffraction projections between the the first Born approximation and the nonlinear projection. The largest difference occurs at high frequencies. The scattered field is from the synthetic data of the disk model.
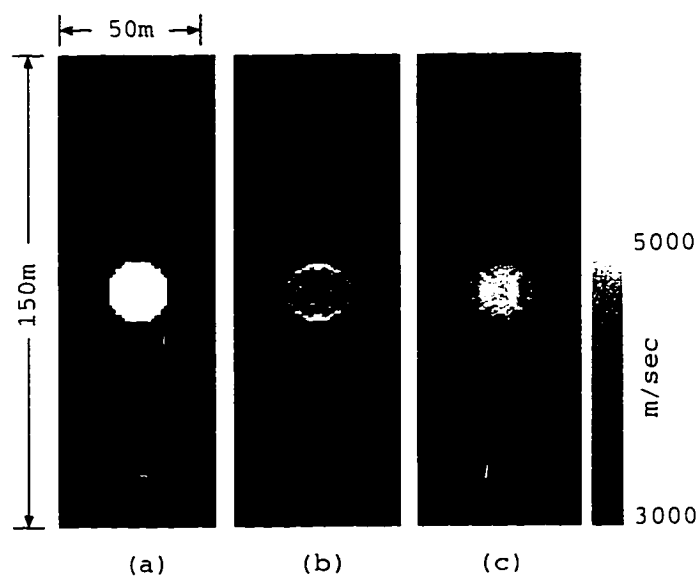
Figure 3.17: A comparison between the first Born approximation and nonlinear projection diffraction tomography: a) is a disk model; b) shows the reconstruction with linear projection; and c) shows the reconstruction with nonlinear projection. The average absolute difference between a) and b), and between a) and c) is 54.6 and 32.4, respectively.
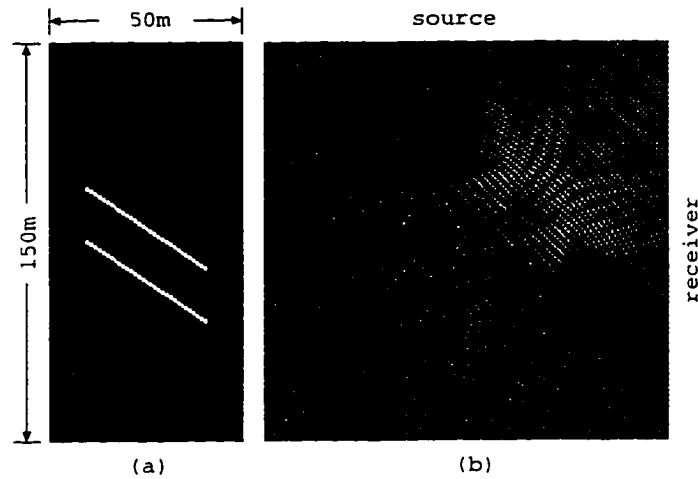
Figure 3.18: Scattered field generated using the moment method: a) a fracture model; and b) scattered field (real part). Frequency $= 1000Hz$.

The inversion results are shown in figure 3.19b and c. We can see that the diffractor lines are thicker comparing to input model and the diffractors in the lines are not distinctly resolved as can be seen by a comparison with the original image. This is caused by the wavenumber domain coverage being constrained to low wavenumber in the crosswell case. In this example, the reconstructed images with Born approximation and nonlinear projection don't show much of a difference, since the multiple scattering is insignificant in forward direction.

When the scale of inhomogeneity is relatively large, effects of multiple scattering become stronger. Figure 3.20 shows a reconstruction from a fault model. One can see that the recovered amplitude agrees with that of the model. The average absolute difference between the model and the reconstruction is 60.3.

Numerical examples in this section demonstrate that the computational efficiency and simplicity of the traditional diffraction tomography can be preserved while the nonlinear effects of multiple scattering are taken into account. Results show the improvement to the first Born approximation for the models that have strongly scattering.
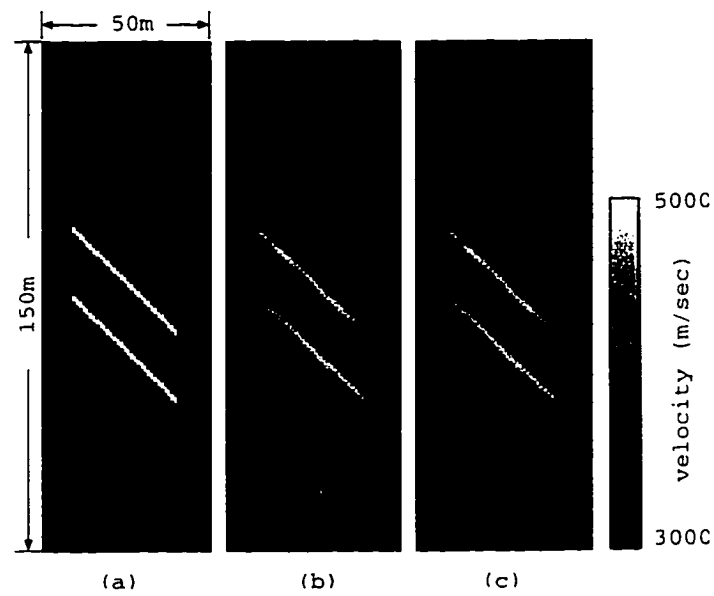
Figure 3.19: A comparison between the linear and nonlinear projection inversion: a) fracture model; b) the reconstruction with linear projection; and c) the reconstruction with nonlinear projection.
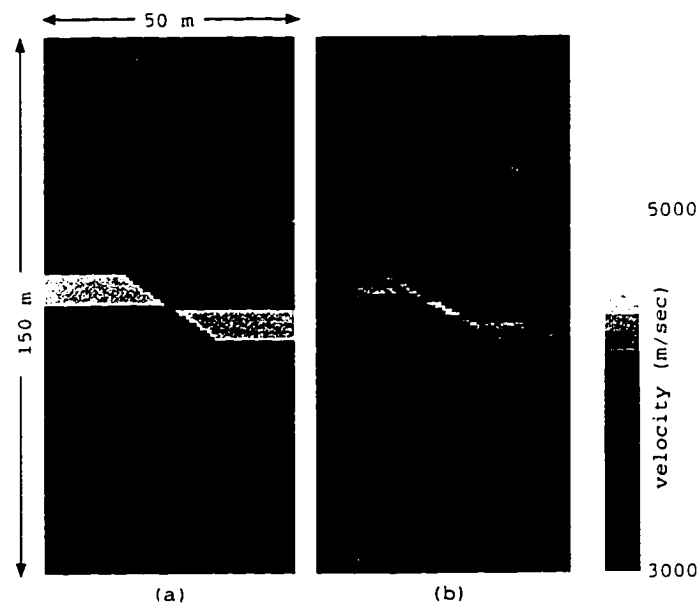
Figure 3.20: Reconstruction of a fault model: a) model, b) tomogram reconstructed using nonlinear inversion. The average absolute difference between the model and the reconstruction is 60.3.

3.4 Renormalization using a stratified background

A stratified background may be determined from well logs or transmission tomography. In this section, the stratified background is used to rescale the incident field to maintain the small perturbations assumptions relative to the layered background. according to the normal mode solution to the scalar wave equation. The Fourier spectrum of the scattered fields is first decomposed into contributions from different layers. Then. a selection rule is applied to sort out the heterogeneity spectrum of the individual layers.

The scattered field in the layered background media can be written as

$$U_l(\mathbf{x}_r, \mathbf{x}_s) = \sum_n^N \int_{s_n} M_n(\mathbf{x})G^l(\mathbf{x}_r, \mathbf{x})G^n(\mathbf{x}, \mathbf{x}_s)d\mathbf{x} \qquad (3.15)$$

where $U_l(\mathbf{x}_r, \mathbf{x}_s)$ is the scattered field in the lth layer. M_n is the reduced perturbation function embedded in n^{th} layer; $G^l(\mathbf{x}_r, \mathbf{x})$ and $G^n(\mathbf{x}, \mathbf{x}_s)$ are the corresponding Green's functions; and N is the number of layers as shown in figure 3.21. It can be shown
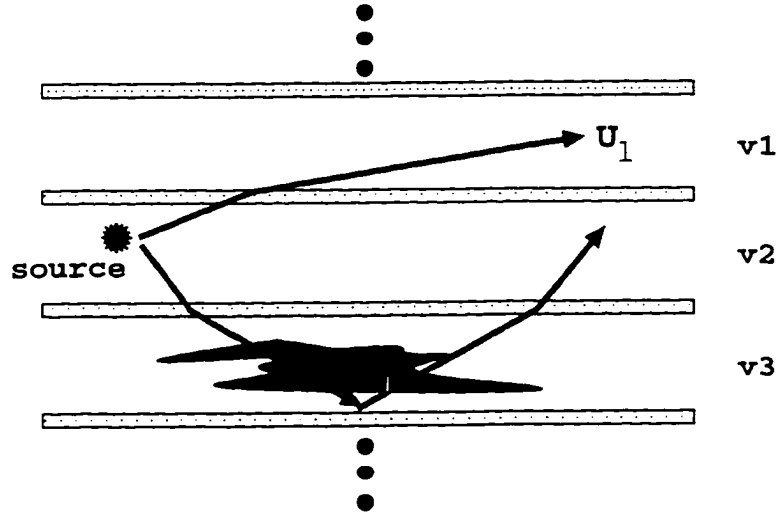
Figure 3.21: The scattered wavefield a layered background medium. The field is contributed from the inhomogeneities embedded in all the layers.

(Harris and Wang, 1996) that, in the spatial frequency domain. equation (3.15) can

be transformed into

$$U_l(\mathbf{k}_r, \mathbf{k}_s) = \sum_n F_{ln}(\mathbf{k}_r, \mathbf{k}_s) M_n(\mathbf{k}_r - \mathbf{k}_s), \tag{3.16}$$

where $F_{ln} = f^n(\mathbf{k}_r, \mathbf{k}_s)(A^l(\mathbf{k}_r)A^n(\mathbf{k}_s) + B^l(\mathbf{k}_r)B^n(\mathbf{k}_s))$; f^n is the weighting function depending on the observation geometry; and A and B are the amplitudes of the up-going and down-going wave, respectively, see figure 3.22. Consequently, the perturbation
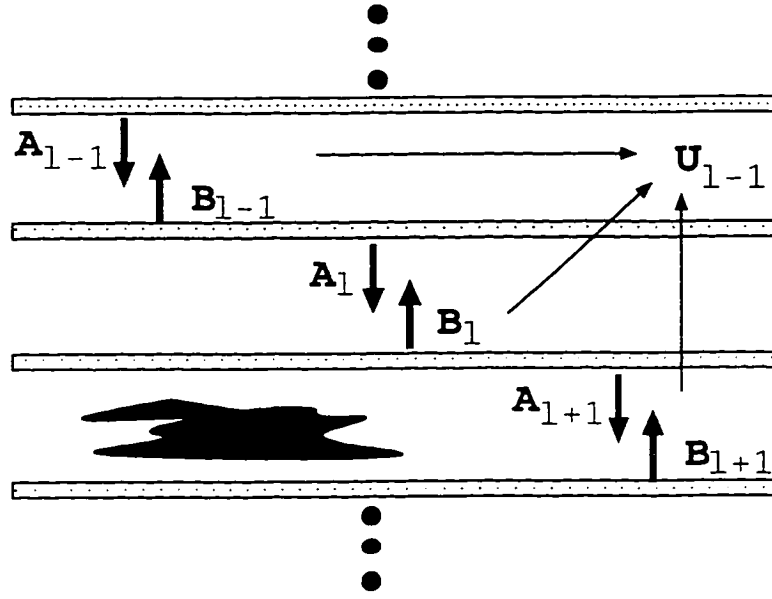
Figure 3.22: The spectrum of the scattered wavefield in a layer.

function spectrum $\{M_n\}$ can be solved as

$$\begin{pmatrix} M_1 \\ \vdots \\ M_N \end{pmatrix} = \begin{pmatrix} F_{11} & \cdots & F_{1N} \\ \vdots & \vdots & \vdots \\ F_{N1} & \cdots & F_{NN} \end{pmatrix}^{-1} \begin{pmatrix} U_1 \\ \vdots \\ U_N \end{pmatrix} \tag{3.17}$$

The perturbation function $m_l(\mathbf{x})$ itself is obtained by taking the inverse Fourier transform of $M_l(\mathbf{k}_r - \mathbf{k}_s)$, as the conventional diffraction tomography (see Appendix A).

3.4.1 Synthetic data inversion

The synthetic model consists of several thin beds embedded in a 3-layer reference medium. The total field and background field, illustrated in figure 3.23, are calculated respectively in the frequency domain for a point source. Instead of averaging the
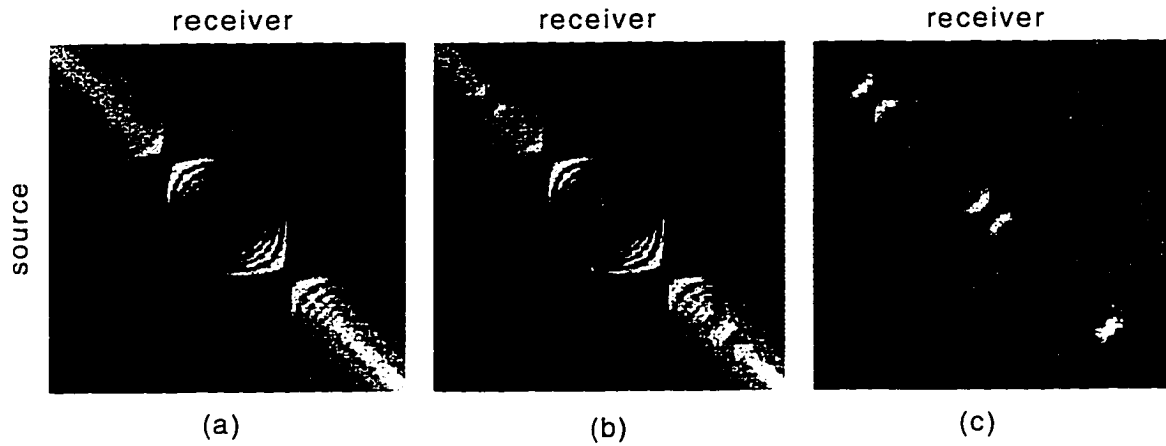
Figure 3.23: The wave field spectra of a three layer model: (a), (b) and (c) are the amplitude of the background field, total field and the scattered field, respectively.

reconstructed images from different frequencies, the calculated frequency responses are averaged in the range between 995 to $1005Hz$, with $5Hz$ incremental frequency, to give a nominal $1000Hz$ response. The scattered field is then obtained by subtracting the background from the total field. The vertical aperture is $256ft$, well separation is $100ft$, and sampling interval is $2.5ft$. The reconstructed image for this model is shown in figure 3.24. The image provides an clear reconstruction of the small perturbations in the model, especially for the location of the thin beds.

3.4.2 Field data inversion

We apply the algorithm to the field data from McElroy test site in west Texas. The measurement geometry is shown in the left panel in figure 3.25. For the well A and well B (separation is $180ft$), both the source and receiver spacing were $2.5ft$ apart. For well B and well C (separation is $600ft$), the sources and receivers' intervals are
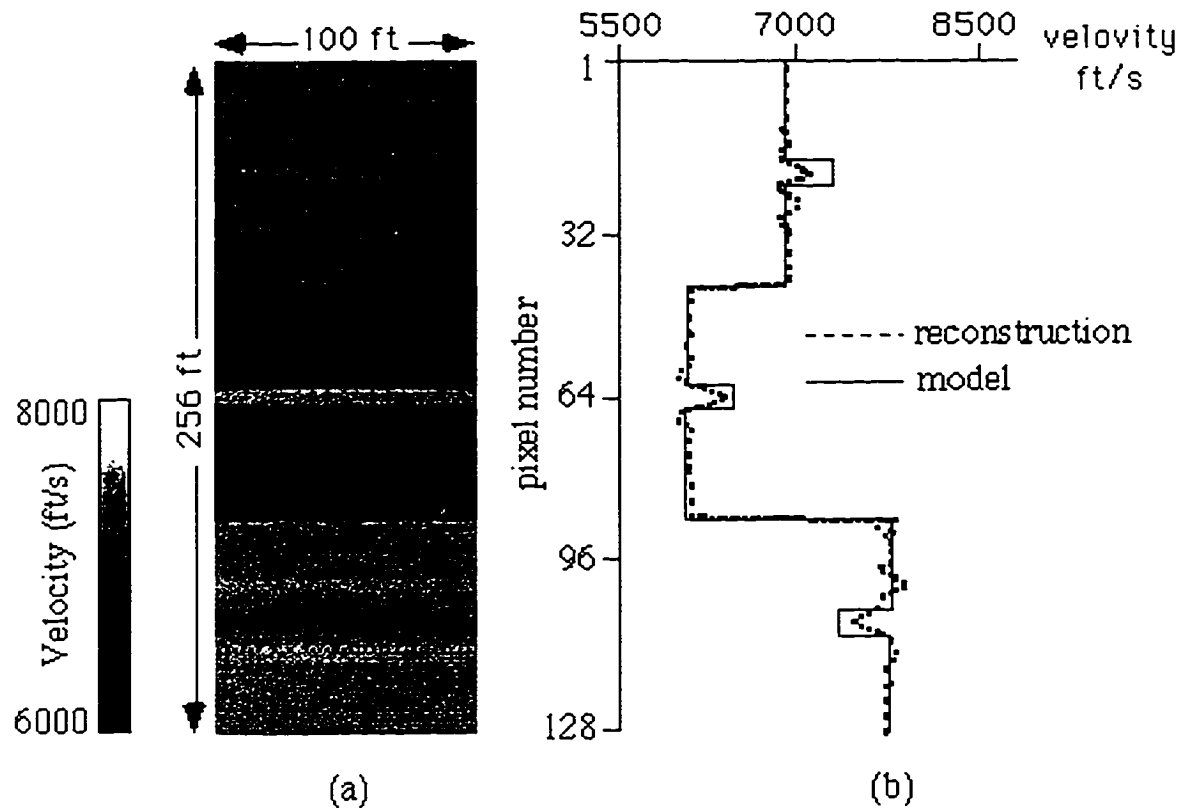
Figure 3.24: 1-D synthetic inversion: (a) is the inversion from the synthetic data; (b) is the cross sections along the depth axis, solid line for the model and dashed line for the reconstruction.

$5ft$. According to prior known geological information, the reservoir is located at the depth between 2850 and $2950ft$.
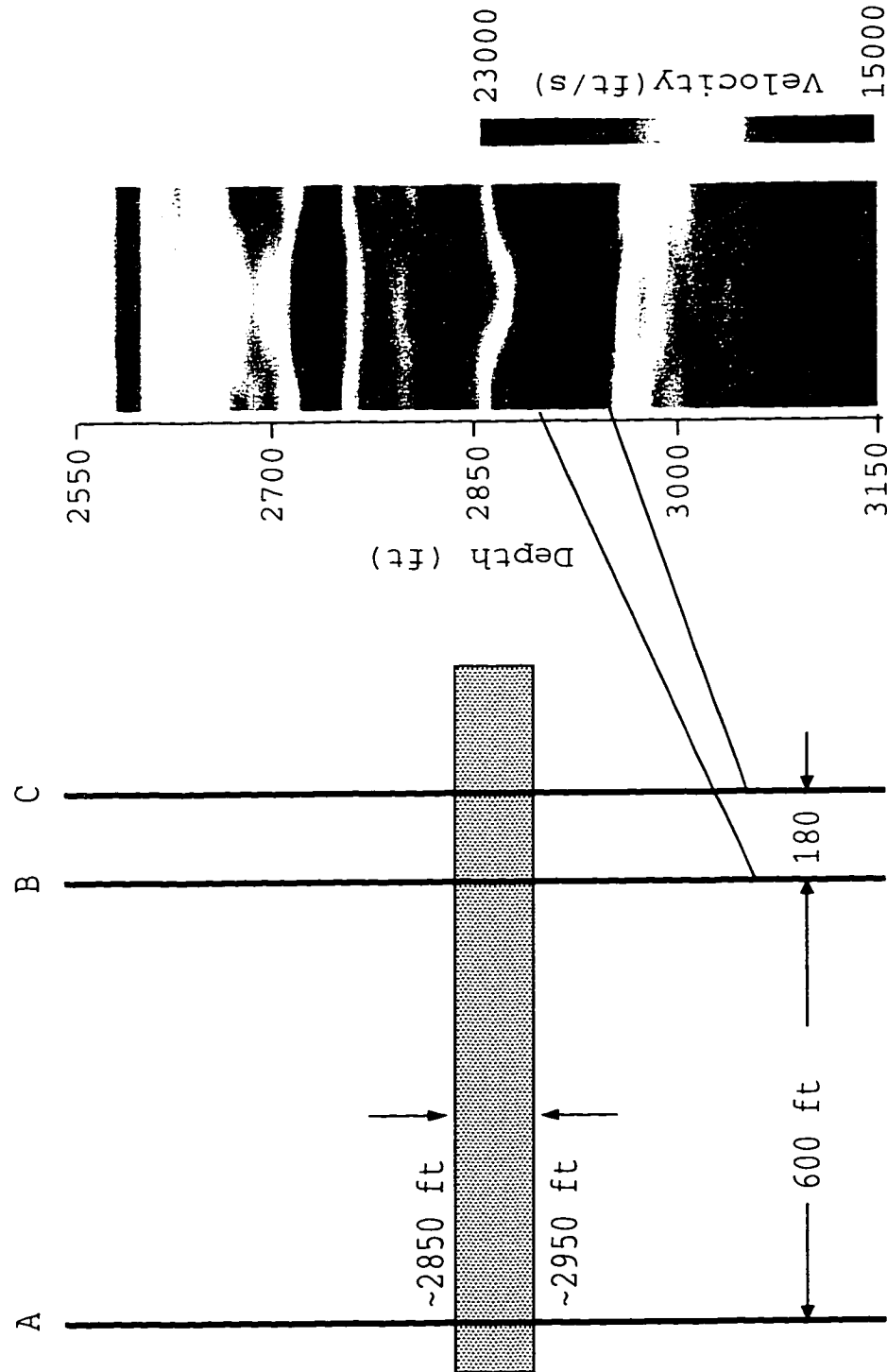
Figure 3.25: The left panel is the well locations of the McElroy field survey and the right panel is a traveltime tomogram inverted from McElroy near offset data.

Again, source function and coupling factors are eliminated by normalizing the amplitude of the wave field at the nearest offset receiver position according to geometrical spreading. The amplitudes of the wave field at the remainder of the receiver positions are normalized relative to the one at the nearest offset. A traveltime tomogram, the right panel in figure 3.25, is used to create a background model, which is used to generate reference field used in diffraction tomography. Notice that although the reservoir zone can be seen, its internal structure is not resolved by the traveltime tomogram.

The diffraction tomogram is reconstructed with the data at frequency $1400Hz$ and the results are shown in figure 3.26. From the object function image and velocity image one can identify the internal structure of the reservoir. This is not surprising. because in essence, with the traveltime tomography one reconstructs the low frequency components of the inhomogeneity. With the diffraction tomography one recovers the higher frequency components. Most of the structures in the reconstructed images here are comparable to those using crosswell reflection imaging and migration techniques (Lazazatos. 1993).

The inversion results of the McElroy far offset data are shown in figure 3.27. From the perturbation function image and velocity image, we can see the improvement of the resolution compared to the traveltime tomogram. especially around the reservoir area. Notice that although the resolution is lower, the far offset images can still be tied to the near offset images, as indicated in figure 3.27.

In an ideal situation in which the source and receiver lines are extended to infinity. the maximum vertical wave number is $2\pi/D$ and the maximum horizontal wave number is $2\pi/\lambda$. If the wavelength is $10ft$ and spatial sampling interval D is $2.5ft$ (one quarter of the wavelength), then the best resolution of the image would be $2.5ft$ in the vertical direction and $10ft$ in horizontal direction. Due to the limited aperture and relatively low frequency, the wave numbers in both vertical and horizontal directions can not reach these maximum values and the reconstructed image is blurred. The resolution of the reconstructed images is reduced. Taking into consideration both resolution limits and distortion effects of limited aperture, the resolution of the image can be estimated as approximately half the wavelength or $5ft$ in the vertical direction
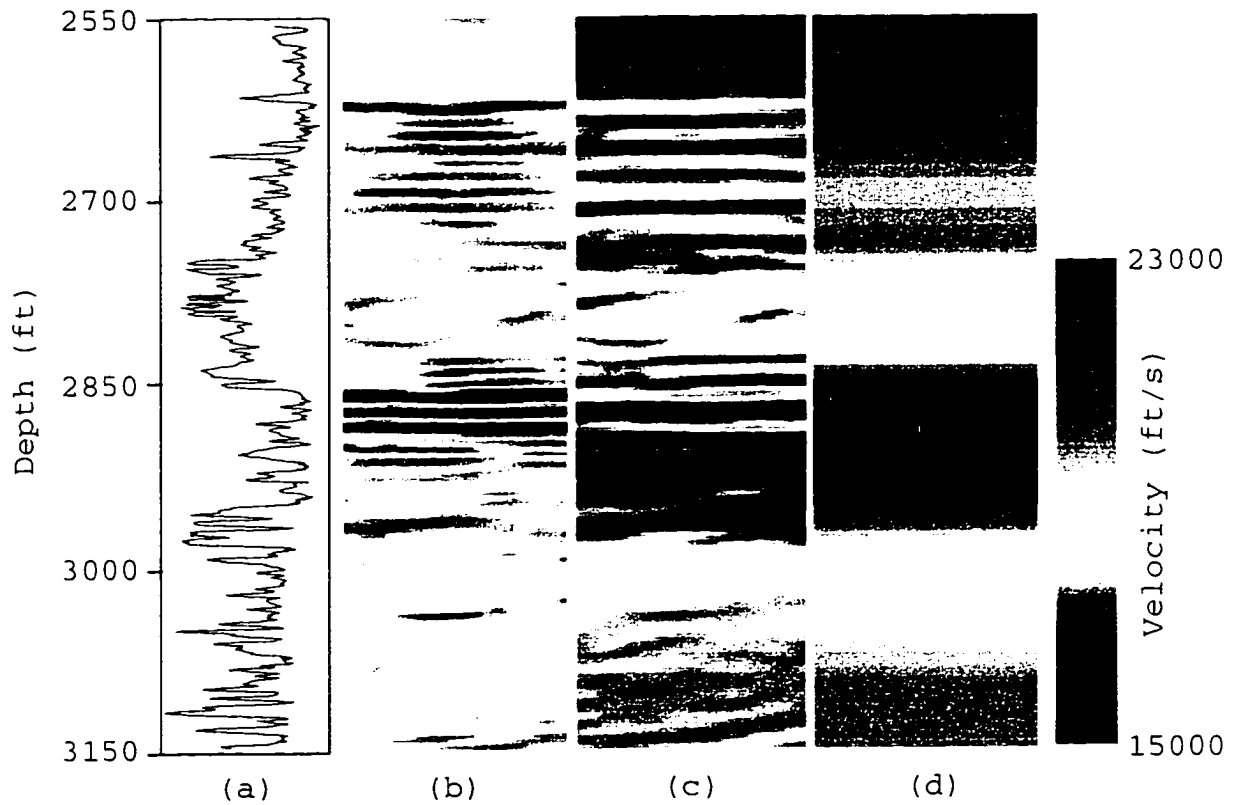
Figure 3.26: Inversion for McElroy near offset data: (a), (b), (c) and (d) are sonic log (well 1202), recovered object function, diffraction tomogram, and 1-d traveltime tomogram, respectively.
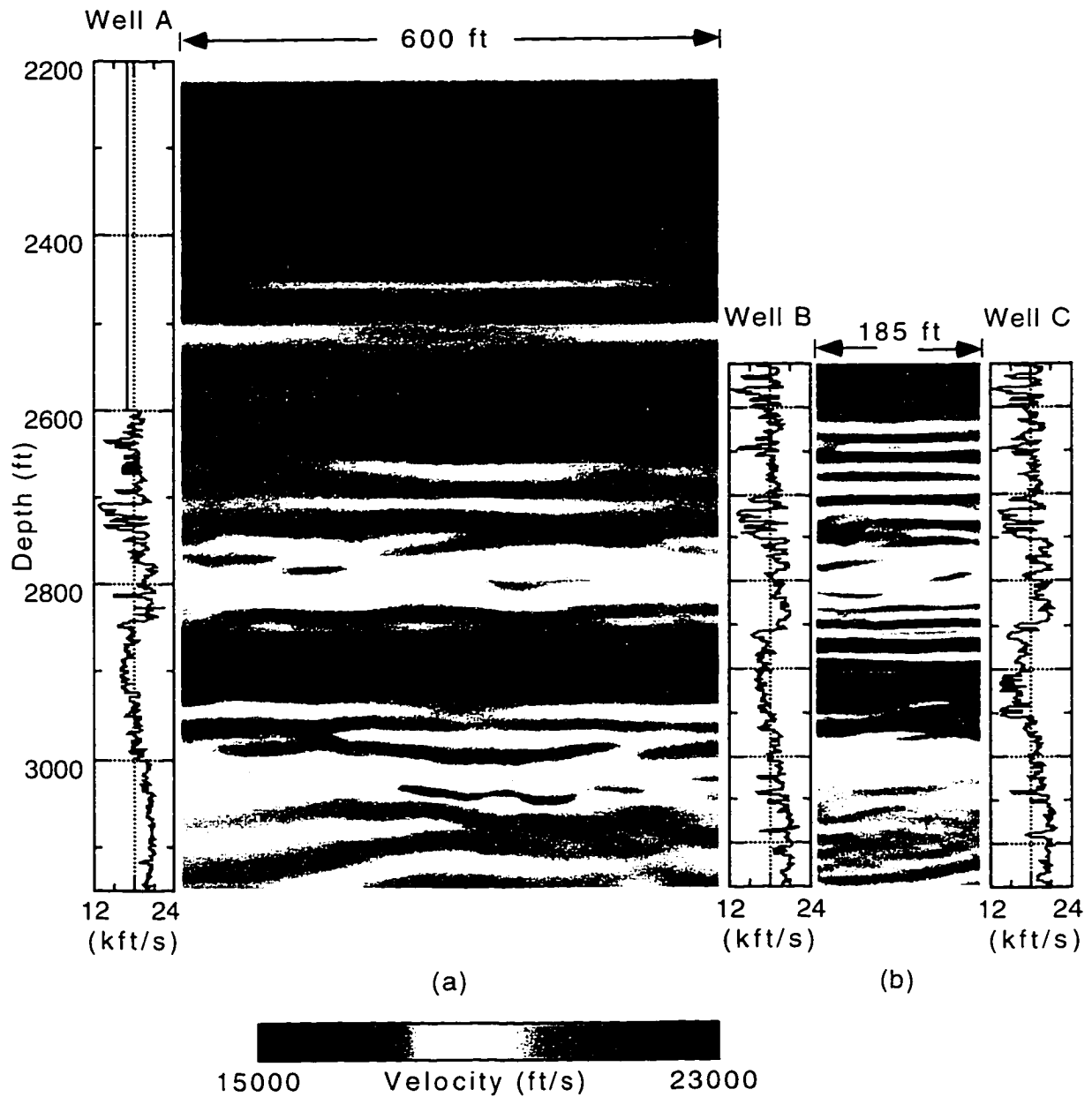
Figure 3.27: Inversion for the McElroy data: (a) and (b) are the far offset and near offset diffraction tomogram, respectively.

and one and one half wavelength, or $15ft$ in the horizontal direction.

3.5 Conclusions

Given the variety of scales and strong inhomogeneity of the earth's medium encountered in geophysics, it is necessary to use efficient approximations especially for inverse problems. The renormalization schemes discussed in this chapter are, essentially. to regulate the Born series and extend the first Born approximation when strong fluctuations are involved. The technique renormalized in the spatial domain is more appropriate for forward modeling, while the renormalization in the spectral domain is more appropriate for inverse problems. Effectiveness of the layering renormalization method is achieved by properly choosing a stratified background medium. using well log or a traveltime tomogram, to maintain the validity of the small perturbation assumption.

Chapter 4

Inversion of Strong Scattering Media Using Wave Asymptotics

In subsurface imaging, another way to describe wave propagation is using rays rather than the wave field itself in the short-wavelength limit. The crux of this formalism lies in the assumption of wave propagation in a medium that is slowly varying in space compared with the wavelength of the wave solutions. The rays are defined by the projections of the trajectory of a Hamilton system in phase space. This chapter reviews asymptotic wave theory and constructs the Green's function using traveltime and ray spreading from paraxial raytracing. The Maslov canonical operator method is used to obtain a uniform asymptotic wave field that is valid even in regions of caustics, where regular ray theory is not applicable. We apply pseudodifferential operator theory, together with distorted Born approximation, to develop an asymptotic inversion method for variable background medium.

4.1 Wave asymptotics

Connections between areas of physics often involve limits, e.g., wave optics reduces to ray optics asymptotically in the limit of small wavelength. A classical description of asymptotic wave theory for light in the geometric optics limit is given in "Principles of Optics" by Born and Wolf, 1970. In this section we shall review the assumptions,

methods and results of the conventional eikonal approach to the asymptotic solution
of a wave equation:

$$\frac{1}{c^2(x)}\ddot{u}(\mathbf{x}, t) - u_{,jj}(\mathbf{x}, t) = 0,\tag{4.1}$$

where $\ddot{u} = \partial_t^2 u$ and the summation is implied over repeated indices and $j = 1, 2, 3$
($u_{,jj} = \nabla^2 u$). To apply the high frequency asymptotic solution to the wave equation.
the basic assumption is that the waves described by $u(\mathbf{x}, t)$ are characterized by a
typical wavenumber $k(\mathbf{x})$ and frequency ω which are large compared with the temporal
and spatial rate of variation of the medium. If this is the case, it is reasonable to
assume that at a point $\mathbf{x}$ the wave solution looks roughly like a plane wave,[1] but
over a larger scale, the amplitude, wavenumber and frequency may vary, as do the
properties of the medium. These concepts are embodied in the solution to the wave
equation (Beydoun and Mendes, 1989)

$$u(\mathbf{x}, t) \equiv A(\mathbf{x})e^{i\phi(\mathbf{x}, t)}.\tag{4.2}$$

where $A(\mathbf{x})$ is amplitude and $\phi(\mathbf{x}, t)$ is phase. In analogy with the plane-wave solutions
in a uniform medium where the phase $\phi(\mathbf{x}, t)$ is $\mathbf{k} \cdot \mathbf{x} - \omega t$, the local wavenumber and
frequency are defined to be the measure of the local rate of variation of the phase,
i.e.,

$$k_j(\mathbf{x}, t) \equiv \phi_{,j}(\mathbf{x}, t), \qquad \omega(\mathbf{x}, t) \equiv -\dot{\phi}(\mathbf{x}, t).\tag{4.3}$$

If the length scales of variation of the medium are L, we can define a small dimen-
sionless parameter ϵ, where

$$k(\mathbf{x}, t)L \equiv \epsilon^{-1} \gg 1,\tag{4.4}$$

---

[1] These locally quasi-plane waves also called eikonal waves, which are asymptotically associated
with a surface of the dispersion relation in phase space (Ziolkowski, 1984).

and impose the conditions

$$\frac{A_j}{A} \sim \frac{k_j}{k} \sim \frac{1}{L},$$

so that the assumptions about the variation of the amplitude $A(\mathbf{x})$ and wavenumber are made explicit. All higher derivatives are assumed to be of correspondingly higher order in ϵ. Inserting equation (4.2) into (4.1), from the real part and imaginary part respectively, one obtains the eikonal equation and transport equation [2]:

$$\sum_j \phi_j^2 - k^2 = 0, \tag{4.5}$$

and

$$2A_j \phi_j + A\phi_{jj} = 0, \tag{4.6}$$

where $k(\mathbf{x}) = \dot{\phi}/c(\mathbf{x})$ is the local wavenumber.

4.1.1 Geometrical optics solutions

To solve the eikonal equation and transport equation with the initial conditions, it is necessary to construct the system of rays. One way of doing this is to write out the Hamilton system consisting of ordinary differential equations. The Hamiltonian is directly obtained from eikonal equation by eliminating one coordinate variable. The Hamiltonian contains all the information that is needed to generate rays and calculate wave fronts.

---

[2]Substitute (4.2) into (4.1) and neglect the second order variations. From the real part, one has $(\dot{\phi}^2/c^2 - \phi_j^2 + A_{jj}/A = 0$, which leads to eikonal equation; from the imaginary part, one obtains $A\ddot{\phi}/c^2 - 2A_j\phi_j + A\phi_{jj} = 0$, which results in transport equation under the high frequency assumption of the amplitude. In general, the amplitude should be expressed as a power series in ϵ: $A = \sum_n \epsilon^n A_n$. As we shall consider only the lowest order in the approximation treatment, this expansion is not necessary.

Solution to eikonal equation

Let $p_j = \phi_{,j}$ be the wave propagation vector or wave momentum, and the Hamiltonian $H(x_j, p_j) = p_j^2 - k^2(\mathbf{x})$ [3], then the eikonal equation can be written as

$$H(x_j, p_j) = p_j^2 - k^2(\mathbf{x}) = 0. \tag{4.7}$$

Obviously, the Hamiltonian H represents the local dispersion relation in this context. The position vector x_j and momentum p_j define a six-dimensional phase space.

The rays emitted at $x_j = x_j^0$ can be parameterized by their take-off angle θ and the independent variable along a ray, σ, i.e.,

$$x_j = x_j(\sigma, \theta), \qquad p_j = p_j(\sigma, \theta). \tag{4.8}$$

The rays are generated in phase space by applying the Hamiltonian equations:

$$\frac{dx_j}{d\sigma} = \frac{\partial H}{\partial p_j}, \qquad \frac{dp_j}{d\sigma} = -\frac{\partial H}{\partial x_j}. \tag{4.9}$$

If ray $\mathbf{x}(\sigma)$ is known, the explicit solution for the eikonal equation in terms of the

---

[3]Hamilton's principle assumes a knowledge of the Lagrangian function $L(q, \dot{q}, t)$ and considers variational paths in the configuration space. It is also possible to set up an equivalent variational principle that assumes a knowledge of the Hamiltonian $H(q, p, t)$ and considers variational paths in phase space q, p. Consider the Legendre transformation of H: $f(p, q, \dot{q}, t) = p\dot{q} - H(q, p, t)$ for the variational paths in phase space to be stationary, i.e.

$$\delta \int_{t1}^{t_2} f(p, q, \dot{q}, t)dt = 0,$$

if and only if the function H satisfies

$$\dot{q} = \frac{\partial H}{\partial p}, \ \dot{p} = -\frac{\partial H}{\partial q},$$

which is the direct result of applying the Euler equations to the function f, i.e.,

$$\frac{d}{dt}\frac{\partial f}{\dot{q}} - \frac{\partial f}{\partial q} = 0, \ \frac{d}{dt}\frac{\partial f}{\dot{p}} - \frac{\partial f}{\partial p} = 0.$$

$\mathbf{x}(\sigma)$ and initial values ϕ_0 is:

$$\phi = \phi_0 + \int_0^\sigma k(\mathbf{x}(\sigma'))d\sigma'. \tag{4.10}$$

Solution to transport equation

The transport equation can also be solved by integrating along the rays. To do so, we express $\phi_{,jj}$ in terms of its variation along a ray tube [4] depicted in figure 4.2. Then,
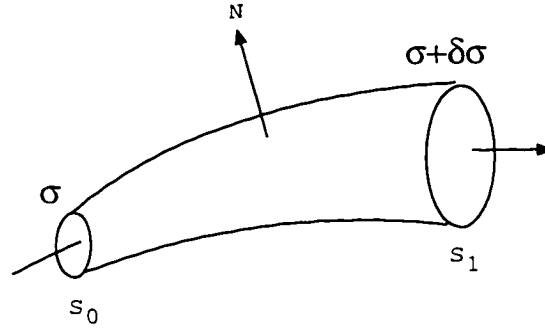
Figure 4.1: Wave propagation along a ray tube

the transport equation (4.6) can be written as

$$2k\frac{dA}{d\sigma} + \frac{1}{J}\frac{d(kJ)}{d\sigma}A = 0, \tag{4.11}$$

---

[4]Consider a region V bound laterally by a tube of rays and capped by two segment of wave fronts, $\phi = constant$ which are denoted as a_0 and a_1 as shown in figure 4.1. Let $\mathbf{N}$ be the exterior unit normal of V, and apply the divergence theorem in V i.e.,

$$\int_s \nabla\phi \cdot \mathbf{N}ds = \int_{a_1} kda - \int_{a_0} kda \approx [kJ|_{\sigma+d\sigma} - kJ|_\sigma]d\xi d\zeta,$$

$$\int_v \nabla^2\phi dv \approx \nabla^2\phi J d\xi d\zeta d\sigma.$$

where J is the Jacobian transformation between the coordinates $\mathbf{x}$ and (σ, ξ, ζ), one obtains

$$\nabla^2\phi = \frac{1}{J}\frac{d(kJ)}{d\sigma},$$

in the limit of $d\sigma \to 0$.

or

$$\frac{2k}{\sqrt{kJ}} \frac{d(A\sqrt{kJ})}{d\sigma} = 0. \tag{4.12}$$

where the Jacobian characterizes the density of the rays in the "ray tube". Integrating along the ray $\mathbf{x}(\sigma)$ from σ_0 to σ we have a solution to amplitude in terms of the density of rays, i.e..

$$A = A(\sigma_0)\sqrt{\frac{k(\sigma_0)J(\sigma_0)}{k(\sigma)J(\sigma)}}. \tag{4.13}$$

Rays may intersect at caustics where $J = 0$ and at these regions a dramatic change of wave propagation (the phase and amplitude) occurs. A caustic is shown in figure 4.2 originates at the instant when the rays intersect. The ray field theory
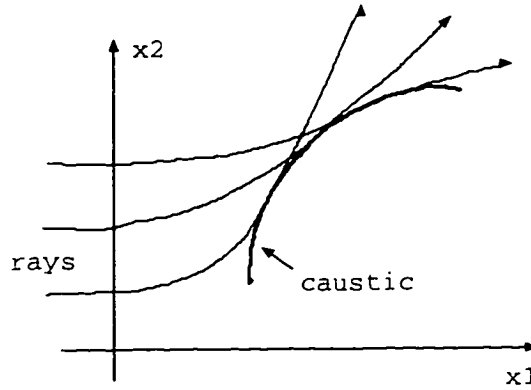
Figure 4.2: When rays intersect and their envelope is caustic

breaks down as soon as the rays intersect. The solutions to the eikonal equation and transport equation break down at a caustic in two ways: continuation of the phase by ray tracing beyond the caustic and the determination of the amplitude by transport equation at a caustic. The former difficulty arises because the solution to eikonal equation is generally multi-valued. The caustic coincides with the joining of the branches of the phase function. As the phase is continued through a caustic, $\pi/2$ phase shifts are resulted. The ray tracing fails to give a prescription for the choice of

the branch on which the continuation should proceed for the phase shift. Amplitude transport fails at a caustic because the tube of rays in which the intensity is being conserved has a zero cross section there; thus the ray theory incorrectly predicts an infinite amplitude. Figure 4.3. shows the raypath and traveltime at receiver locations. The caustics occurred in the low velocity zone for the given source location (the model used to generate rays to be described in the following section).

Figure 4.3: Raytracing through a velocity model. The left panel shows the caustics occurred in the low velocity zone for the given source location; the right panel shows the triplication of the traveltime at the receiver positions.

4.1.2 Maslov uniform solution

Maslov introduced the concept of Lagrangian submanifolds (Maslov. 1988) while generalizing the earlier one-dimensional work of Keller (1958)[5] to overcome the difficulties of representing the eikonal wave field at caustics. The main idea of Maslov's method is that the asymptotic wave field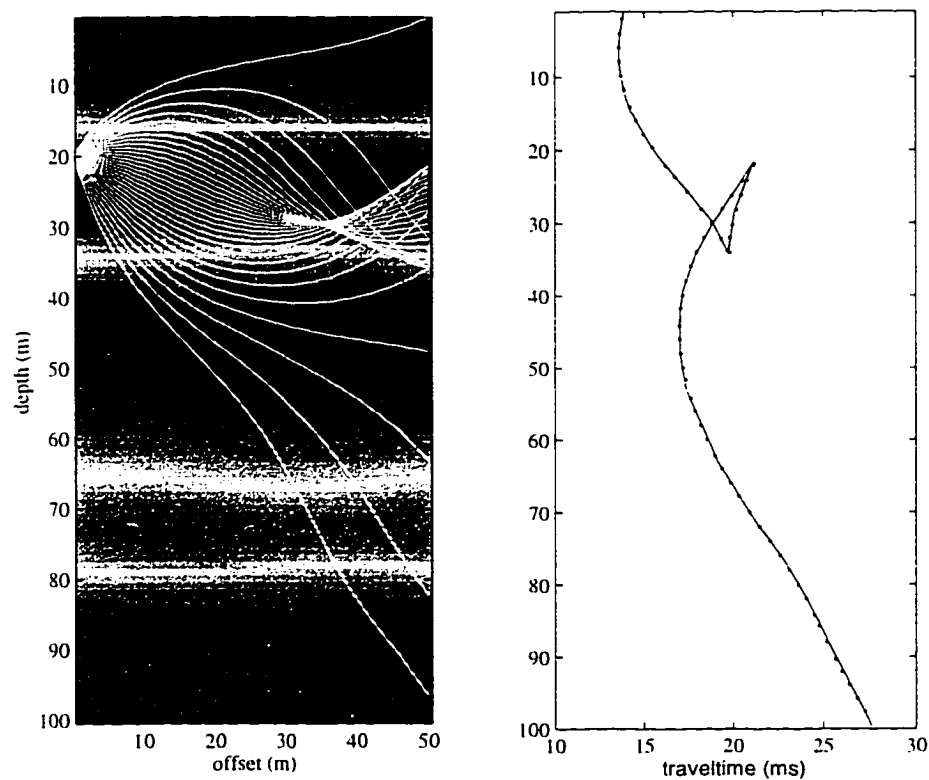 should be constructed not in the real space but in the phase space where the rays present no caustics. The phase space $\mathcal{M}$ consists of a position vector $\mathbf{x}$ and a wave slowness vector $\mathbf{p}$. The desired field can be obtained by transforming the phase space solution back to real space. The surface determined
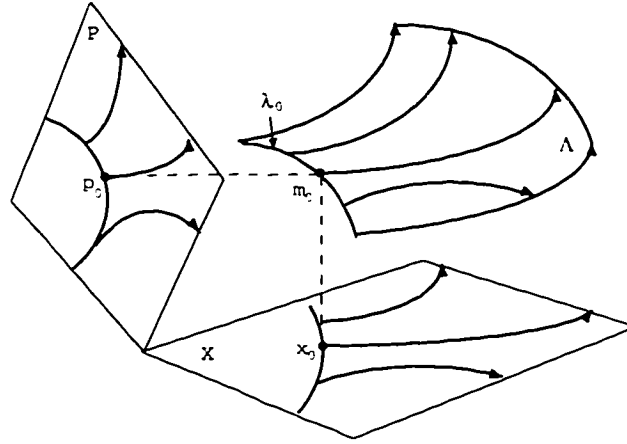
Figure 4.4: The rays and their velocity vector in the space X and P are projections of phase space trajectories and their velocity vectors. Λ is a Lagrangian submanifold in the phase space.

by the dispersion relation in phase space is called the Lagrangian submanifold Λ by Maslov, on which the bicharacteristics of the Hamiltonian evolve. The importance of the Λ is to produce global solutions including representations in the caustic regions (Kravtsov. 1990, 1993, Ziolkwski, 1983, Bregman and Chapman, 1989). as depicted in figure 4.4. Intuitively, a locally plane wave with propagation vector p_j is restricted to the particular values $p_j = \phi_j$ in the phase phase space and can be projected onto

---

[5]Ordinary asymptotic wave theory breaks down when diffraction occurs where the medium scale length is as small as the wavelength, or near turning points. Keller has developed a geometric diffraction theory which uses geometric optics away from the bad regions in the medium and glues in the extra rays due to diffraction emanating from these regions using matched asymptotics.

x or p space equally.

Analogous to equation (4.2), the wave field in phase space can be written as

$$u(\mathbf{p}, \mathbf{x}_c) \sim B(\mathbf{p}, \mathbf{x}_c)e^{\iota\Phi(\mathbf{p}, \mathbf{x}_c)}. \tag{4.14}$$

The function $\Phi(\mathbf{p}, \mathbf{x}_c)$ in phase-space is obtained via the Legendre transformation of ϕ, i.e..

$$\Phi(\mathbf{p}, \mathbf{x}_c) = \mathbf{p}\mathbf{x}_c - \phi(\mathbf{x}_c),$$

where $\mathbf{x}_c$ is the location of caustics. Similarly, the $B(\mathbf{p}, \mathbf{x}_c)$ is calculated using the Jacobian in phase space, i.e.,

$$\tilde{J} = (\partial\mathbf{p}, \partial\mathbf{x}|\partial\theta, \partial\sigma)_{\mathbf{x}=x_c} \ .$$

Equation (4.14) is defined as the asymptotic Fourier transform $\mathcal{F}_0$ (see Appendix C). A suitable choice of coordinates in the phase space can always eliminate the singularity of $B(\mathbf{p}, \mathbf{x})$ at caustics. Thus, the $u(\mathbf{x})$ at a caustic is finite. A choice of mixed coordinates in which $\tilde{J} \neq 0$, though $J = 0$, relies on the properties of the Lagrangian submanifold of the phase space. The wave field estimation is completed by the KMAH index that will determine the $\pi/2$ phase shift when a ray passes through a caustic. The wave field in the real space can be obtained by taking the Fourier transform of equation (4.14), i.e.

$$u(\mathbf{x}_c) \sim \int_{-\infty}^{\infty} B(\mathbf{p}, \mathbf{x}_c)e^{\iota\Phi(\mathbf{p}, \mathbf{x}_c)}e^{\iota\mathbf{p}\mathbf{x}_c}dp. \tag{4.15}$$

For example, in a two dimensional numerical implementation, one can choose the mixed coordinates (p_x, z), such that at caustic x_c

$$u(x_c, z) \sim \int_{-p_{max}}^{p_{max}} B(p_x, z)e^{\iota\Phi(p_x, z)}e^{\iota p_x x_c}dp_x,$$

where the amplitude $B(p_x, z)$ can be calculated using the corresponding Jacobian $\tilde{J}$

as in the case of real space,

$$\tilde{J} = \begin{vmatrix} \partial p_x/\partial\theta & \partial p_x/\partial\sigma \\ \partial z/\partial\theta & \partial z/\partial\sigma \end{vmatrix}.$$

In general, the continuation of a field through a caustic region has the alternating compact representation (Ziolkwski, 1983):

$$u(\mathbf{x}) = \begin{cases} u(\mathbf{x}) & \text{if } \mathbf{x} \text{ is away from any caustic} \\ \{\mathcal{F}^{-1} \circ \mathcal{F}_0\}[u(\mathbf{x})] & \text{if } \mathbf{x} \text{ is near a caustic.} \end{cases} \qquad (4.16)$$

The asymptotic Fourier operator $\mathcal{F}_0$ (see Appendix C) effectively cancels the singularities in the regular ray theory field $G_0(\mathbf{x})$. Clearly, if $\mathbf{x}$ is sufficiently far from a caustic, the operator $\mathcal{F}^{-1}$ can be replaced with $\mathcal{F}_0^{-1}$ and returns to regular ray theory solution immediately.

4.1.3   Numerical implementation

In order to calculate the raypath and its perturbation, we implement paraxial ray tracing. The position of a paraxial ray and the wave momentum can be written as:

$$\mathbf{x}(\sigma) = \mathbf{x}_0(\sigma) + \delta\mathbf{x}(\sigma), \qquad (4.17)$$

$$\mathbf{p}(\sigma) = \mathbf{p}_0(\sigma) + \delta\mathbf{p}(\sigma), \qquad (4.18)$$

where δ is used for paraxial perturbations with regarding to take-off angle. (Cerveny, 1984, Farra, 1989). The perturbation of ray position and the slowness vector deduced from equation (4.9) are:

$$\delta\dot{\mathbf{x}} = \nabla_x\nabla_p H \delta\mathbf{x} + \nabla_p\nabla_p H \delta\mathbf{p}, \qquad (4.19)$$

$$\delta\dot{\mathbf{p}} = -\nabla_x\nabla_x H \delta\mathbf{x} - \nabla_p\nabla_x H \delta\mathbf{p}, \qquad (4.20)$$

or

$$\begin{pmatrix} \delta\dot{\mathbf{x}} \\ \delta\dot{\mathbf{p}} \end{pmatrix} = \begin{pmatrix} \nabla_x\nabla_p H & \nabla_p\nabla_p H \\ -\nabla_x\nabla_x H & -\nabla_p\nabla_x H \end{pmatrix} \begin{pmatrix} \delta\mathbf{x} \\ \delta\mathbf{p} \end{pmatrix},$$
                                                                                        (4.21)

where $\dot{\mathbf{x}}$ and $\dot{\mathbf{p}}$ represent $dx/d\sigma$ and $dp/d\sigma$, respectively and ∇_x, ∇_p are the gradient operators regarding to $\mathbf{x}$ and $\mathbf{p}$ respectively. We can solve the ray system and the paraxial ray system simultaneously by using Runge-Kutta method, i.e.,

$$\begin{pmatrix} \dot{\mathbf{x}} \\ \dot{\mathbf{p}} \end{pmatrix} = \begin{pmatrix} \nabla_p H \\ -\nabla_x H \end{pmatrix}$$

$$\begin{pmatrix} \delta\dot{\mathbf{x}} \\ \delta\dot{\mathbf{p}} \end{pmatrix} = \begin{pmatrix} \nabla_x\nabla_p H & \nabla_p\nabla_p H \\ -\nabla_x\nabla_x H & -\nabla_p\nabla_x H \end{pmatrix} \begin{pmatrix} \delta\mathbf{x} \\ \delta\mathbf{p} \end{pmatrix}.$$

with initial conditions:

$$\mathbf{x} = \mathbf{x}_s,$$

$$\mathbf{p} = (cos\theta, sin\theta)/v,$$

$$\delta x = 0,$$

$$\delta\mathbf{p} = (-sin\theta, cos\theta)/v.$$

With the raypath perturbation information, one is able to calculate the Jacobian, i.e.,

$$J = \begin{pmatrix} \partial x/\partial\theta & \partial z/\partial\theta \\ \partial x/\partial\sigma & \partial z/\partial\sigma \end{pmatrix},$$

or, in phase space,

$$\tilde{J} = \begin{pmatrix} \partial p_x/\partial\theta & \partial z/\partial\theta \\ \partial p_x/\partial\sigma & \partial z/\partial\sigma \end{pmatrix}.$$

To check the computer program, we compare the theoretical ray spreading of a homogeneous medium with that calculated using the raypath information resulting

from raytracing. As indicated in Figure 4.5, the calculated value agrees with the theoretic prediction. In Figure 4.6, we show that the phase and amplitude of the wave are correctly simulated in a three layer model.
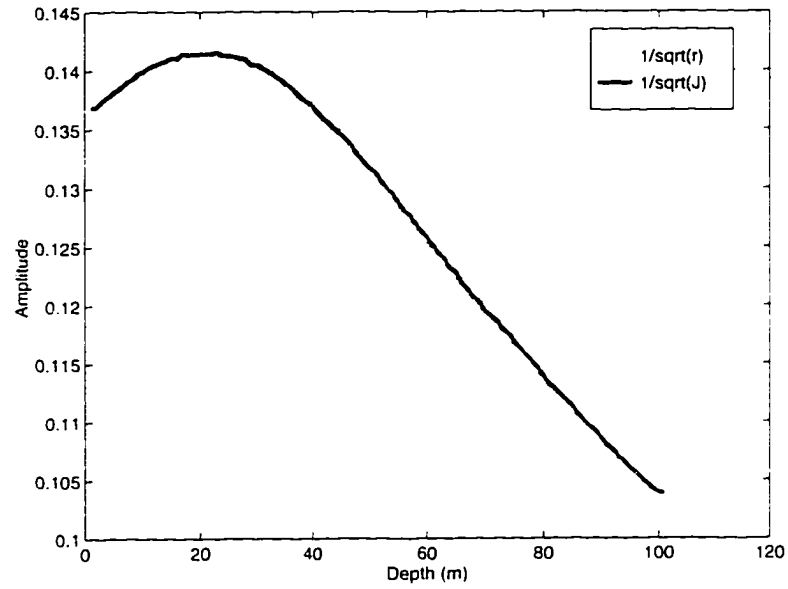

Figure 4.5: A comparison of the amplitudes simulated by $1/\sqrt{r}$ and by $1/\sqrt{J}$ in a homogeneous medium, where Jacobian J is calculated using paraxial raypath information.
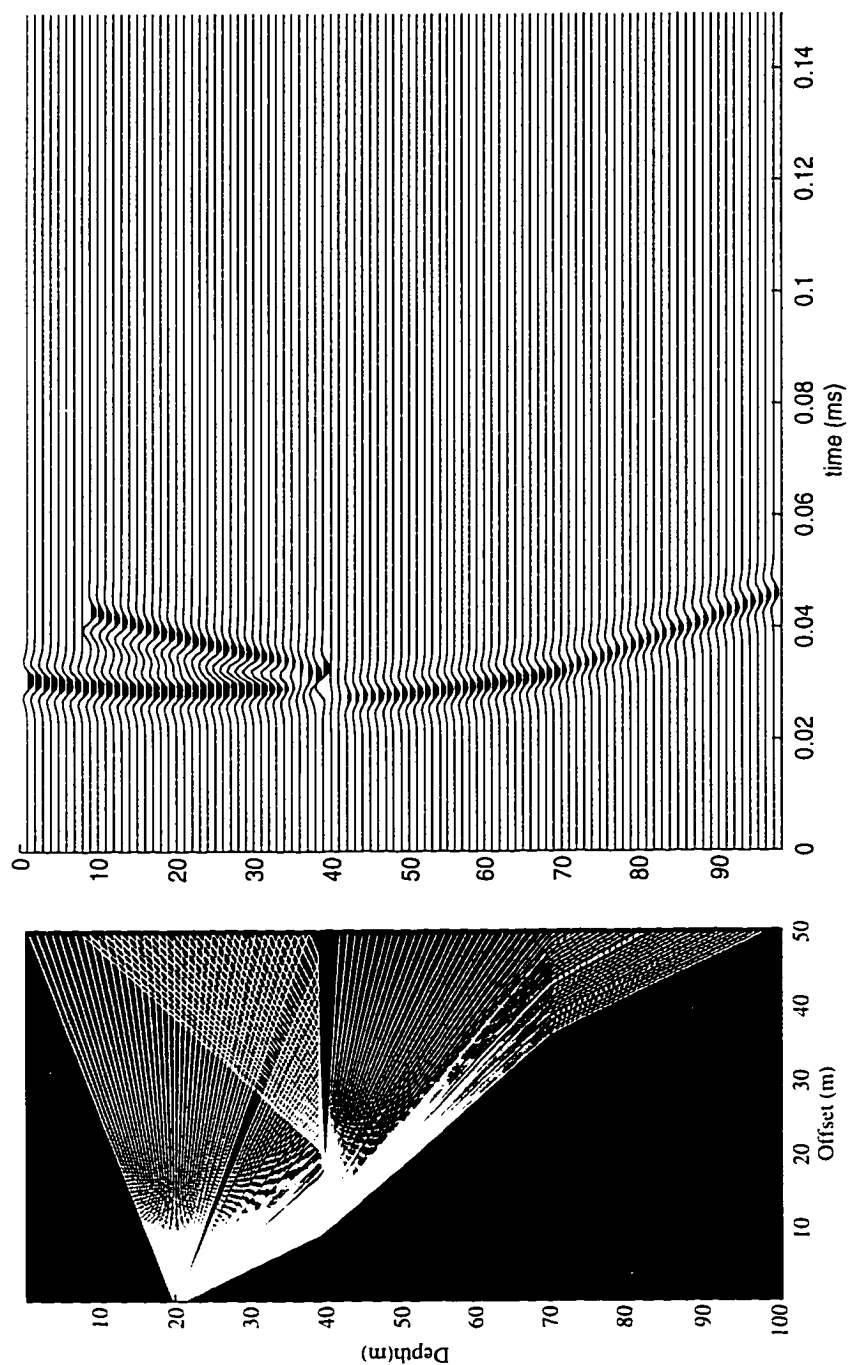
Figure 4.6: Wavefield calculation using wave asymptotics over a layer model: the left panel is raypath image; the right panel is a time section. Both phase and amplitude are correctly predicted.

In the following examples, the velocity model is random characterized by an ellipsoidal autocorrelation function (see chapter 6). The correlation lengths are chosen such as the model approach a 1-D model. The raypath of the source in a low velocity zone is displayed in figure 4.3. One caustic region is clearly identified. Figure
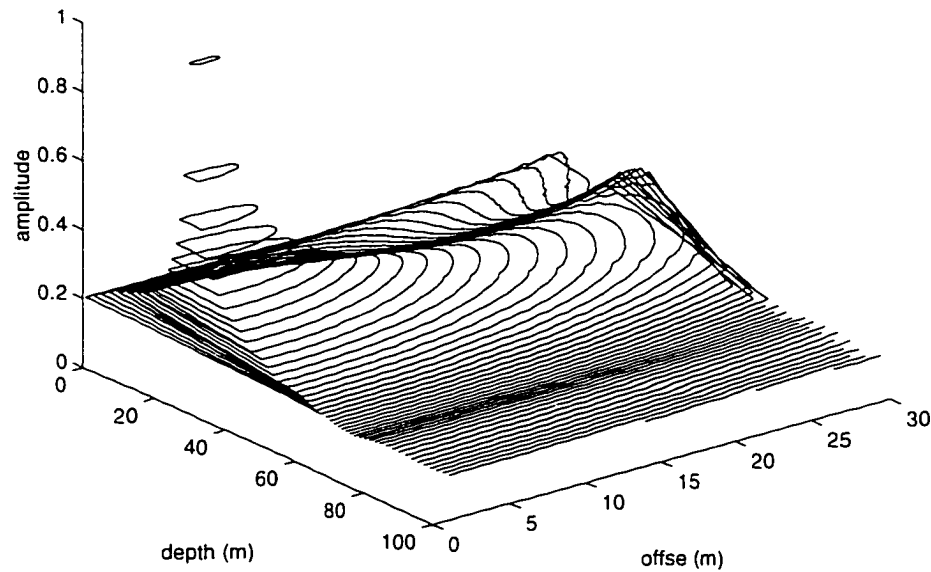
Figure 4.7: Wave amplitude vs. wave front: the contour lines represent wave front and the elevations represent amplitude.

4.7 shows the wave front and wave amplitude. The contour lines represent the wave front and the elevation of the contour represents the amplitude. One can see that the variation both of the wavefront and amplitude are continuous even at the caustic region indicated in figure 4.3.

In figure 4.8, we show the wave amplitude of an array of sources and an array of receivers, which is the data configuration used in the inverse problem discussed in the following sections. Since the model is complicated, one can see that there are some shadow zones where the raytracing can not go through. Therefore, the amplitude is not calculated there.

In summary, the Maslov technique provides a means of constructing a uniform
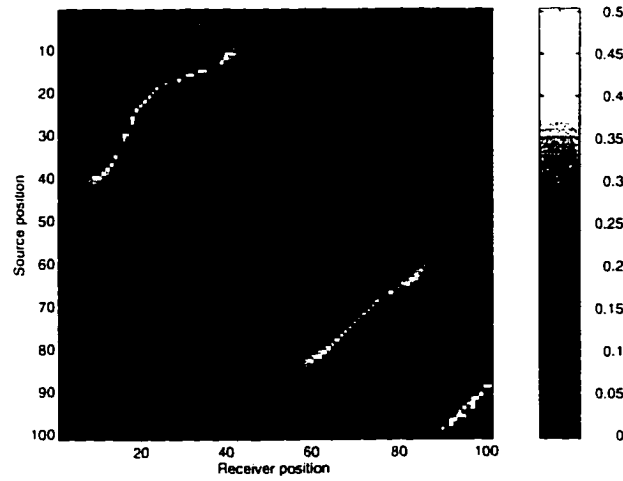
Figure 4.8: The amplitude variation in the map of source and receiver arrays.

asymptotic solution to the wave equation. To find an asymptotic solution that is valid in the vicinity of a caustic, we express the wavefield as a summation of neighboring rays, rather than just considering the contribution from a single ray. Apart from caustics, Maslov synthetics agree with those based on classical ray theory.

4.2   Asymptotic inversion of scalar waves

As in the forward modeling, we assume the background wave field propagates in a smoothly inhomogeneous medium. The condition of smoothness requires that the characteristic scale of the field variations is much smaller than the scale of medium property variations. We use the results from previous sections to calculate wave asymptotics of the variable background and use the distorted Born approximation to estimate the scattered field. The inversion operator is constructed using the generalized Fourier transform.

4.2.1 Inversion theory

The scattering integral for the scalar wave can be written as

$$U(\mathbf{r}, \mathbf{s}) \approx \int m(\mathbf{x}) A(\mathbf{x}, \mathbf{r}, \mathbf{s}) e^{i\phi(x,r,s)} d\mathbf{x}, \tag{4.22}$$

where $U(\mathbf{r}, \mathbf{s})$ is the scattered field at the receiver position $\mathbf{r}$ for a given source at location $\mathbf{s}$, $m(\mathbf{x}) = -k_0^2(\mathbf{x})(1 - c_0^2(\mathbf{x})/c^2(\mathbf{x}))$, $A(\mathbf{x}, \mathbf{r}, \mathbf{s}) = \tilde{A}(\mathbf{x}, \mathbf{s})\hat{A}(\mathbf{r}, \mathbf{x})$ is the product of the amplitude and $\phi(\mathbf{x}, \mathbf{r}, \mathbf{s}) = \tilde{\phi}(\mathbf{x}, \mathbf{s}) + \hat{\phi}(\mathbf{x}, \mathbf{r})$ is the total phase of the background field propagating from source location to x, then from $\mathbf{x}$ to the receiver location, which is calculated using the procedure described in the previous section.

According to the pseudodifferential operator theory (see Appendix D), it is possible to invert the integral (4.22) with asymptotic Fourier transform, i.e.,

$$\hat{m}(\mathbf{x}) = \int U(\mathbf{r}, \mathbf{s}) H(\mathbf{r}, \mathbf{s}, \mathbf{x}) \frac{e^{-i\phi(x,r,s)}}{A(\mathbf{x}, \mathbf{r}, \mathbf{s})} d\mathbf{r} d\mathbf{s}, \tag{4.23}$$

where $H(\mathbf{r}, \mathbf{s}, \mathbf{x})$ is a weighting function to be determined. Substituting equation (4.22) into (4.23), one obtains

$$\hat{m}(\mathbf{x}) = \int m(\mathbf{x}') R(\mathbf{x}, \mathbf{x}') d\mathbf{x}', \tag{4.24}$$

where

$$R(\mathbf{x}, \mathbf{x}') = \int \frac{A(\mathbf{x}', \mathbf{r}, \mathbf{s})}{A(\mathbf{x}, \mathbf{r}, \mathbf{s})} H(\mathbf{r}, \mathbf{s}, \mathbf{x}) e^{i[\phi(x',r,s) - \phi(x,r,s)]} d\mathbf{r} d\mathbf{s}. \tag{4.25}$$

The Fourier integral $R(\mathbf{x}, \mathbf{x}')$ is a pseudodifferential operator (Treves, 1980) and its principle symbol is

$$\frac{A(\mathbf{x}', \mathbf{r}, \mathbf{s})}{A(\mathbf{x}, \mathbf{r}, \mathbf{s})} \frac{H(\mathbf{r}, \mathbf{s}, \mathbf{x})}{|J(k; \mathbf{r}, \mathbf{s})|}, \tag{4.26}$$

where $J(k; \mathbf{r}, \mathbf{s})$ is the coordinate transformation from $\mathbf{k}$ to $(\mathbf{r}, \mathbf{s})$. Note that the pseudodifferential operator relates the object function and its estimate. Obviously, it

can be understood as a model resolution operator.

If the operator $R(\mathbf{x}, \mathbf{x}')$ is a δ-like function, then $\hat{m}(\mathbf{x})$ would be identical to $m(\mathbf{x})$. Applying Taylor expansion at the neighborhood of $\mathbf{x}$ to the amplitude and traveltime and taking only leading term, one has

$$A(\mathbf{x}', \mathbf{r}, \mathbf{s}) \approx A(\mathbf{x}, \mathbf{r}, \mathbf{s}),$$

$$\tilde{\phi}(\mathbf{x}', \mathbf{s}) - \tilde{\phi}(\mathbf{x}, \mathbf{s}) \approx \tilde{\phi}_{,j}(\mathbf{x}, \mathbf{s})(x_j - x_j'),$$

$$\hat{\phi}(\mathbf{x}', \mathbf{r}) - \hat{\phi}(\mathbf{x}, \mathbf{r}) \approx \hat{\phi}_{,j}(\mathbf{x}, \mathbf{r})(x_j - x_j').$$

Letting spatial variant wave vectors $\tilde{k}_j = \tilde{\phi}_{,j}(\mathbf{x}, \mathbf{s})$, $\hat{k}_j = \hat{\phi}_{,j}(\mathbf{x}, \mathbf{r})$, and $k_j(\mathbf{x}) = \tilde{k}_j + \hat{k}_j$. $j = 1, 2, 3$. and change variable such that $d\mathbf{k} = |J(\mathbf{k}; \mathbf{r}, \mathbf{s})| d\mathbf{r} d\mathbf{s}$. one obtains

$$R(\mathbf{x}, \mathbf{x}') = \int \frac{H(\mathbf{r}, \mathbf{s}, \mathbf{x})}{|J(\mathbf{k}; \mathbf{r}, \mathbf{s})|} e^{\iota k_j (x_j' - x_j)} d\mathbf{k}. \tag{4.27}$$

If we choose $H(\mathbf{r}, \mathbf{s}, \mathbf{x}) = |J(\mathbf{k}; \mathbf{r}, \mathbf{s})|$, then $R(\mathbf{x}, \mathbf{x}') \rightarrow \delta(\mathbf{x}, \mathbf{x}')$. Consequently. the inversion equation (4.23) takes the form of

$$\hat{m}(\mathbf{x}) = \int U(\mathbf{r}, \mathbf{s}) |J(\mathbf{k}; \mathbf{r}, \mathbf{s})| \frac{e^{-\iota\phi(x, \mathbf{r}, \mathbf{s})}}{A(\mathbf{x}, \mathbf{r}, \mathbf{s})} d\mathbf{r} d\mathbf{s}. \tag{4.28}$$

By choosing weighting function $H(\mathbf{r}, \mathbf{s}, \mathbf{x}) = |J(\mathbf{k}; \mathbf{r}, \mathbf{s})|$, one can reconstruct the inhomogeneity function consist with the information containing in the wave asymptotics. For example, in the two dimensional case, the local wavenumber can be expressed as

$$k_x = k_0(\mathbf{x})(\cos\theta(\mathbf{x}, \mathbf{s}) + \cos\theta(\mathbf{r}, \mathbf{x}))$$

$$k_z = k_0(\mathbf{x})(\sin\theta(\mathbf{x}, \mathbf{s}) + \sin\theta(\mathbf{r}, \mathbf{x})),$$

and the Jacobian transformation J can be calculated as

$$J(\mathbf{k}; \mathbf{r}, \mathbf{s}) = k_0^2(\mathbf{x}) sin\theta(\mathbf{g}, \mathbf{s}) \frac{\partial\theta(\mathbf{x}, \mathbf{s})}{\partial s} \frac{\partial\theta(\mathbf{g}, \mathbf{x})}{\partial g}, \tag{4.29}$$
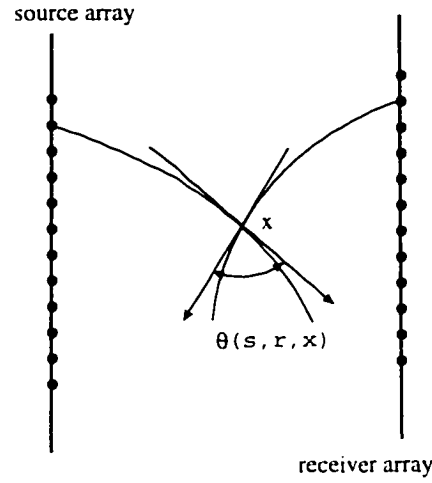
Figure 4.9: At scattering point x, the coming and departure rays make a bisect angle.

where $\theta(\mathbf{r}, \mathbf{s}) = \theta(\mathbf{r}, \mathbf{x}) - \theta(\mathbf{x}, \mathbf{s})$ is the bisect angle[6], as indicated in Figure 4.9. Assuming no temporal dispersion, letting $\phi = \omega\tau$ and choosing an appropriate wavelet, it is possible to transform (4.28) into time domain, e.g.,

$$\hat{m}(\mathbf{x}) = \Re \int \frac{|J(\mathbf{k}; \mathbf{r}, \mathbf{s})|}{A(\mathbf{x}, \mathbf{r}, \mathbf{s})} U(\mathbf{r}, \mathbf{s}, t)|_{t=\tau(\mathbf{x}, \mathbf{r}, \mathbf{s})} d\mathbf{r} d\mathbf{s}, \tag{4.30}$$

where $\Re$ denotes the real part of the integral. $t = \tau(\mathbf{x}, \mathbf{r}, \mathbf{s})$ is called the imaging condition as in the case of migration (Claerbout, 1986).

The reason that the inverse scattering and migration merge to the same algorithm is that asymptotically, the Fourier space and real space are superimposed. Withe a complete set of frequencies, the inverse scattering algorithm using wave asmptotics and Kirchoff migration are essentially the same and this is illustrated in figure 4.10 and figure 4.11.

---

[6]Notice that

$$J(\mathbf{k}; \mathbf{r}, \mathbf{s}) \quad = \quad k_0^2(\mathbf{x})(\frac{\partial cos\theta(\mathbf{x}, \mathbf{s})}{\partial s} \frac{\partial sin\theta(\mathbf{r}, \mathbf{x})}{\partial r} - \frac{\partial cos\theta(\mathbf{r}, \mathbf{x})}{\partial r} \frac{\partial sin\theta(\mathbf{x}, \mathbf{s})}{\partial s}).$$
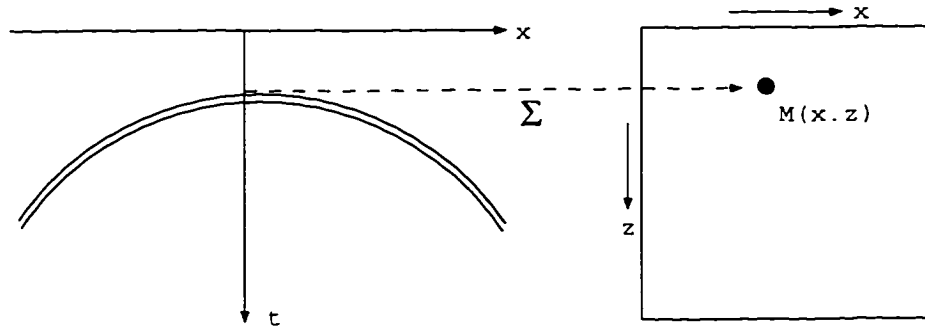
Figure 4.10: The algorithm of Kirchoff migration sums data within the diffraction shape, then places the summed value on the migrated section.
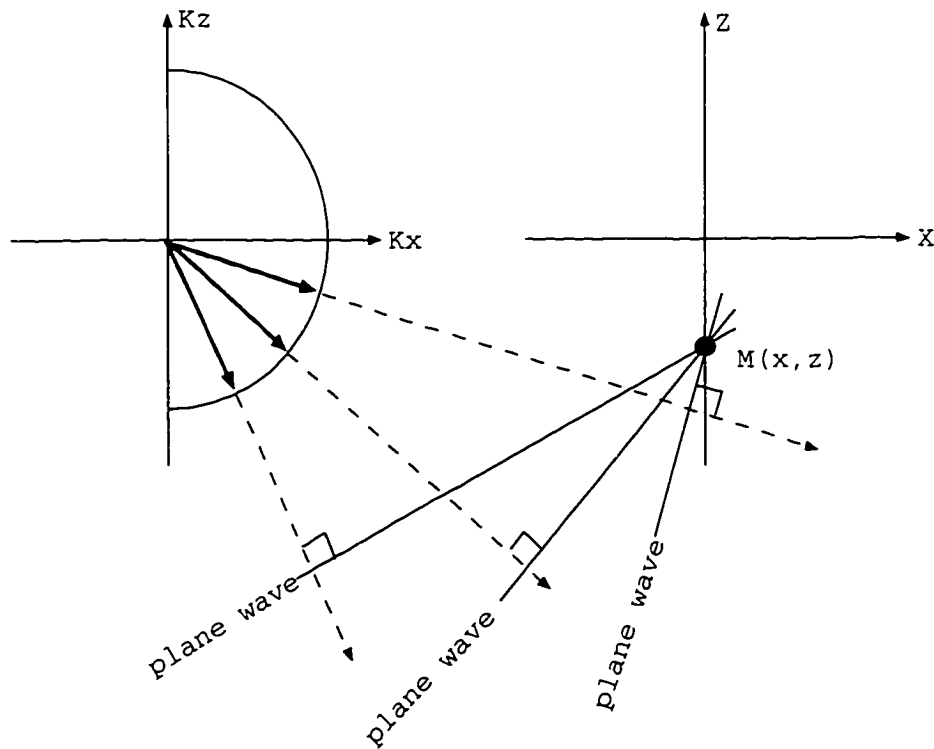

Figure 4.11: The method of asymptotic inverse scattering constructively sums the plane waves in wavenumber domain to produce the discontinuity of the medium.

4.3 Inversion of elastic waves

In the case of elastic wave inversion, the object function of the scattering operator has multiple terms (the perturbations of the density and the elastic constants) and each term has a different polarization factor corresponding to monopole. dipole and multipoles. We have to modify the procedure applied to the scalar wave. In order to recover each term of the object function, the scattered fields are project into different polarization directions, then apply asymptotic Fourier transform to these projections. The resultant multiple "raw" images are then used to solve individual elastic parameters.

4.3.1 Asymptotic Green's function of elastic media

Supposing the density and elastic constant of the medium can be written as

$$c_{lmpq} = c^0_{lmpq} + c'_{lmpq}, \qquad \rho = \rho^0 + \rho',$$

where ρ^0, c^0_{lmpq} are background density and elastic constant. and $\rho'. c'_{lmpq}$ are their perturbations, the integral solution of the scattered field can be obtained for $\mathbf{u}$ using Betti's Theorem. the vector equivalent of Green's Theorem for scalars (see Chapter 2):

$$U_{jk}(\mathbf{s}. \mathbf{r}, t) = - \int [\rho' \partial_t^2 u_{jl} *_t \hat{G}_{kl} + c'_{lmpq} u_{jp.q} *_t \hat{G}_{kl.m}] d\mathbf{x}. \tag{4.31}$$

In the frequency domain,

$$U_{jk}(\mathbf{s}, \mathbf{r}, \omega) = - \int [\rho' \omega^2 u_{jl} \hat{G}_{kl} + c'_{lmpq} u_{jp.q} \hat{G}_{kl,m}] d\mathbf{x}. \tag{4.32}$$

Assuming a smoothly varying background medium and applying the distorted Born approximation, i.e., $u_{jl} \approx \tilde{G}_{jl}$, then

$$U_{jk}(\mathbf{s}, \mathbf{r}, \omega) \approx - \int [\rho' \omega^2 \tilde{G}_{jl} \hat{G}_{kl} + c'_{lmpq} \tilde{G}_{jp,q} \hat{G}_{kl,m}] d\mathbf{x}. \tag{4.33}$$

For an isotropic elastic medium, the asymptotic Green's functions in (4.33) can be decomposed as p and s components:

$$\tilde{G}_{jl} = \tilde{G}_{jl}^p + \tilde{G}_{jl}^s, \qquad \hat{G}_{kl} = \hat{G}_{kl}^p + \hat{G}_{kl}^s, \tag{4.34}$$

where

$$\tilde{G}_{jl}^p = \tilde{A}_{jl}^p e^{\imath \tilde{\phi}^p}, \qquad \tilde{G}_{jl}^s = \tilde{A}_{jl}^s e^{\imath \tilde{\phi}^s},$$

$$\hat{G}_{kl}^p = \hat{A}_{kl}^p e^{\imath \hat{\phi}^p}, \qquad \hat{G}_{kl}^s = \hat{A}_{kl}^s e^{\imath \hat{\phi}^s}.$$

The eikonal equations for the phase functions $\tilde{\phi}^p, \hat{\phi}^p, \tilde{\phi}^s$ and $\hat{\phi}^s$ are:

$$\sum_{j=1,2,3} [\tilde{\phi}_{,j}^p]^2 = \sum_{k=1,2,3} [\hat{\phi}_{,k}^p]^2 = \gamma_p^2,$$

$$\sum_{j=1,2,3} [\tilde{\phi}_{,j}^s]^2 = \sum_{k=1,2,3} [\hat{\phi}_{,k}^s]^2 = \gamma_s^2.$$

where $\gamma_p = \omega/v_p$ and $\gamma_s = \omega/v_s$ are the wavenumbers for the p-wave and the s-wave, respectively. The corresponding transport equation for the amplitudes $\tilde{A}^p, \hat{A}^p, \tilde{A}^s$ and $\hat{A}^s$ are:

$$\left(\frac{\rho^0}{\gamma_p^2}\tilde{A}_{jp}^p\tilde{A}_{jp}^p\tilde{\phi}_{,m}^p\right)_{,m} = 0,$$

$$\left(\frac{\rho^0}{\gamma_p^2}\hat{A}_{kp}^p\hat{A}_{kp}^p\hat{\phi}_{,m}^p\right)_{,m} = 0,$$

$$\left(\frac{\rho^0}{\gamma_s^2}\tilde{A}_{jp}^s\tilde{A}_{jp}^s\tilde{\phi}_{,m}^s\right)_{,m} = 0,$$

$$\left(\frac{\rho^0}{\gamma_s^2}\hat{A}_{kp}^s\hat{A}_{kp}^s\hat{\phi}_{,m}^s\right)_{,m} = 0,$$

with no summation over j and k (Burridge, 1976)[7]

---

[7]In the case of vector amplitude, assume an asymptotic expansion of the solution to the elastic wave equation:
$$u_l = \sum A_l^n(\mathbf{x})f_n, \quad A_l^n = 0, \ n < 0,$$

Again, the problem of finding the asymptotic solution resulting from given sources decomposes into two parts: ray tracing which defines the continuation of the phase independent of the amplitude; and determination of the amplitude, which is carried out by following intensity variations along the rays.

where A_i^n is the amplitude, $f_n = e^{i\phi}(i\omega)^{-n}$ and ϕ is the phase. Substituting the expansion into elastic wave equation and equating the coefficient of f_{-2} to zero, one has

$$(\rho\delta_{ik} - c_{ijkl}k_jk_l)A_k^0 = 0,$$

where $k_j = \phi_{,j}$ and $k_l = \phi_{,l}$. Let $\rho\xi^2(\mathbf{k})$ be an eigenvalue of the symmetric positive definite matrix $c_{ijkl}k_jk_l$. Obviously, $\xi^2(\mathbf{k}) = 1$ and A^0 is the corresponding eigenvector. The eikonal equation, for A is parallel and perpendicular to $\mathbf{k}$, respectively, can be written as

$$\xi^2(\mathbf{k}) = |\mathbf{k}|^2/\gamma_p^2, \quad \xi^2(\mathbf{k}) = |\mathbf{k}|^2/\gamma_s^2.$$

Equating the coefficient of f_{-1} to zero, one has

$$(\rho\delta_{ik} - c_{ijkl}k_jk_l)A_k^1 + (c_{ijkl}k_lA_k^0)_{,j} + c_{ijkl}A_{k,l}^0k_j = 0.$$

In order to obtain the transport equation, the above equation is contracted with A_i^0, i.e.

$$A_i^0(\rho\delta_{ik} - c_{ijkl}k_jk_l)A_k^1 + A_i^0(c_{ijkl}k_lA_k^0)_{,j} + A_i^0c_{ijkl}A_{k,l}^0k_j = 0.$$

Notice that A_i^0 is a null vector of matrix $(\rho\delta_{ik} - c_{ijkl}k_jk_l)$, so the first term vanishes. The reset two terms can be combined as the transport equation:

$$(c_{ijkl}A_i^0A_k^0k_l)_{,j} = 0.$$

By differential $(\rho\xi^2\delta_{ik} - c_{ijkl}k_jk_l)A_k^0 = 0$, with respect to k_p, one has

$$(\rho\xi^2\delta_{ik} - c_{ijkl}k_jk_l)(A_k^0)' + (2\rho\xi\xi'\delta_{ik} - c_{ipkl}k_l - c_{ijkp}k_j)A_k^0 = 0.$$

Contracting with A_i^0, the first term vanishes and one obtains $\rho\xi\xi'A_i^0A_i^0 = c_{ipkl}A_i^0A_k^0k_l$. Noticing that $\xi\xi' = k_p/\gamma^2$, $\gamma = \gamma_p$ or γ_s, one simplifies the transport equation as:

$$(c_{ijkl}A_i^0A_k^0k_l)_{,j} = (\frac{\rho}{\gamma}|\mathbf{A}^0|^2\mathbf{k}_j)_j = 0.$$

4.3.2 Inversion theory

We can rewrite (4.31) as (see Chapter 5):

$$U(\mathbf{r}, \mathbf{s}) = \int \sum_{l=1,2,3} o_l(\mathbf{x}) w_l(\cos\theta(\mathbf{x}, \mathbf{r}, \mathbf{s})) A(\mathbf{x}, \mathbf{r}, \mathbf{s}) e^{\iota\phi(x,\mathbf{r},\mathbf{s})} d\mathbf{x}, \qquad (4.35)$$

where $U(\mathbf{r}, \mathbf{s})$ represents one of the components of a specific elastic scattered wave mode such as U_{jk}, $o_l(\mathbf{x})$ is the object function, and $w_l(\cos\theta)$ is denoted as the polarization factor. As in the previous section, amplitude $A(\mathbf{x}, \mathbf{r}, \mathbf{s}) = \bar{A}(\mathbf{x}, \mathbf{s})\dot{A}(\mathbf{x}, \mathbf{r})$ and traveltime $\phi(\mathbf{x}, \mathbf{r}, \mathbf{s}) = \bar{\phi}(\mathbf{x}, \mathbf{s}) + \dot{\phi}(\mathbf{x}, \mathbf{r})$. In the case of p-p scattering,

$$o_l(\mathbf{x}) \subset \{\frac{\lambda'}{\lambda^0 + 2\mu^0}, \frac{\rho'}{\rho^0}, \frac{2\mu'}{\lambda^0 + 2\mu^0}\}, \qquad w_l(\cos\theta) \subset \{1, \cos\theta, \cos^2\theta\}.$$

Utilizing the results of the scalar wave inversion, one obtains :

$$\sum_{l=1,2,3} o_l(\mathbf{x}') g_{lm}(\cos\theta) = \mathcal{F}_m\{U(\mathbf{r}, \mathbf{s})\}(\mathbf{x}) \qquad (4.36)$$

where

$$g_{lm}(\cos\theta) = w_l(\cos\theta) w_m(\cos\theta),$$

$$\mathcal{F}_m\{U(\mathbf{r}, \mathbf{s}, \omega)\}(\mathbf{x}) = \int \frac{U(\mathbf{r}, \mathbf{s}) w_m(\cos\theta)|J|}{A(x, \mathbf{r}, \mathbf{s})} e^{-\iota\phi(\mathbf{x}, \mathbf{r}, \mathbf{s})} d\mathbf{s} d\mathbf{r}.$$

and $|J(k_j|\mathbf{r}, \mathbf{s})|$ is the Jacobian transformation as in the case of scalar wave. The wave vectors are defined as the following:

$$\bar{k}_j = \bar{\phi}_{,j}(\mathbf{x}, \mathbf{s}), \qquad \dot{k}_j = \dot{\phi}_{,j}(\mathbf{x}, \mathbf{r}), \qquad \mathbf{k}_j = \bar{k}_j + \dot{k}_j.$$

Again the pseudodifferential operator $\mathcal{F}_m$ is the generalized Fourier transform. Notice that the additional weighting function w_m is used to facilitate the recovering individual component o_l of the object function. In the time domain, as in the case of scalar

wave, one obtains:

$$\sum_{l=1,2,3} o_l(\mathbf{x}) g_{lm}(\cos\theta) = \mathcal{F}_m\{U(\mathbf{r}, \mathbf{s}, t)\}(\mathbf{x})_{t=\tau(\mathbf{r},\mathbf{x},\mathbf{s})}. \tag{4.37}$$

4.4   Inversion examples

This section demonstrates the algorithm with numerical experiments. The first example is a model of five diffractors. The synthetic data is generated using the moment method. Figure 4.12 shows the model and the reconstruction, which is comparable to the model except the horizontal blurring due to the limited aperture of the source array and receiver array.
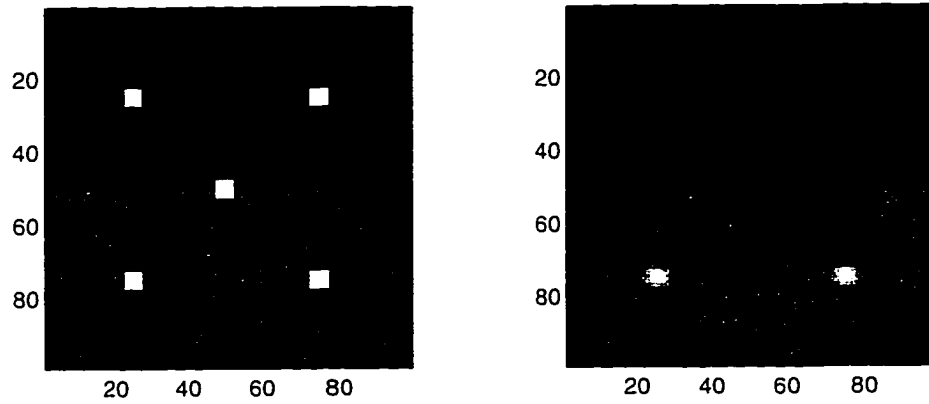

Figure 4.12: Image constructed from diffractor model (slowness): (a) is the model and (b) is the reconstructed slowness image.

The second experiment is based on a model with complicated structure units. The synthetic data is calculated by the distorted Born approximation. Notice that the receiver array is located in the bottom surface instead of on the top, i.e. the forward scattering wave field is generated. The original model is decomposed into background and the perturbation to the background (see figure 4.13). Figure 4.14 shows the model and a common source gather. The inversion of the data using the Born approximation is used to show that the algorithm is correct under the given assumption and that the factors influence the inversion. Figure 4.15 shows the reconstructions with different background velocity. Figure 4.15a is the reconstruction with
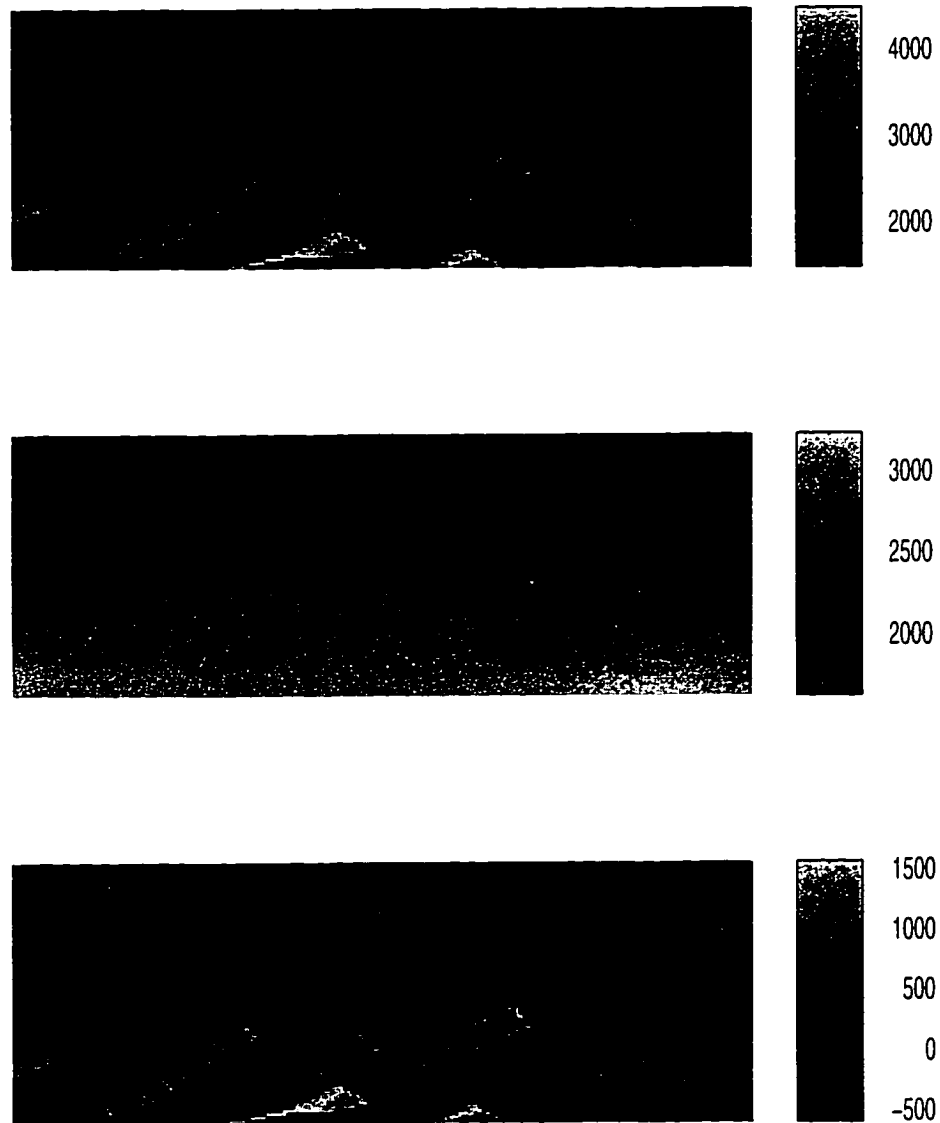
Figure 4.13: A complicated velocity model: The top panel is a velocity model with complicated structure units, where different shading indicates different velocity; the middle and bottom panels are the decomposed background and perturbation to the background.
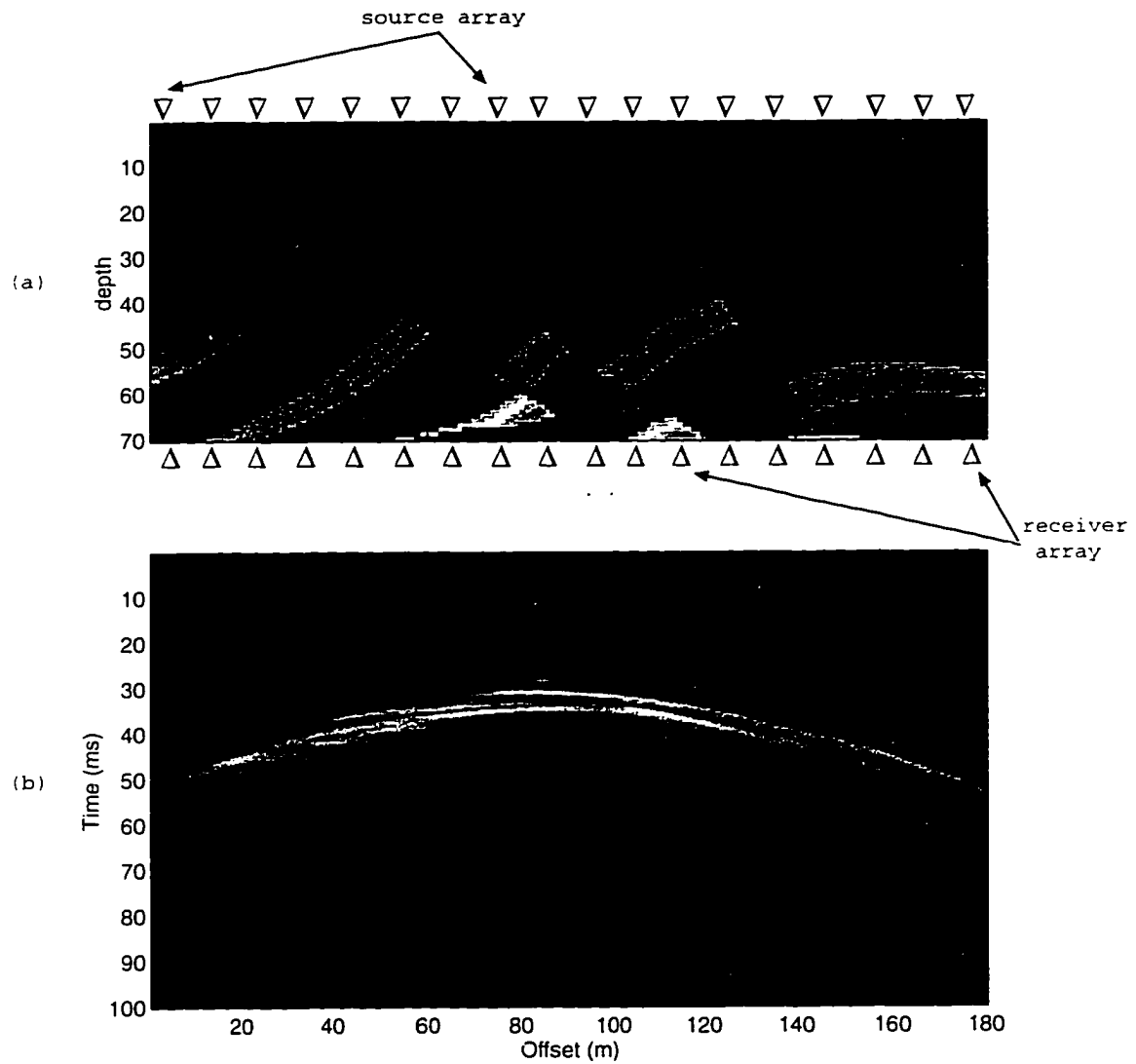
Figure 4.14: A source gather of the complicated synthetic model. The source and receiver locations are displayed in (a) and the scattered field of a common source gather generated using the Born approximation method is shown in (b).
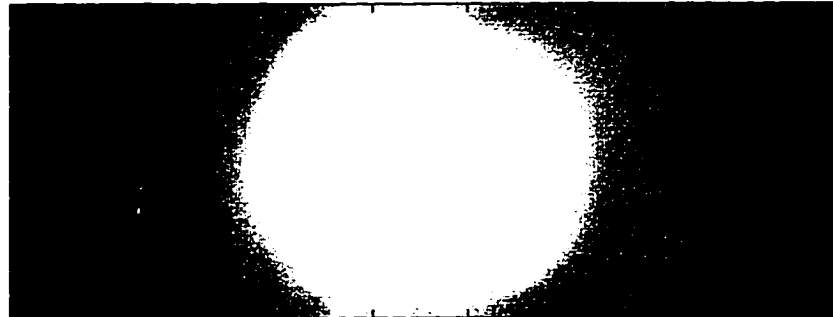
(a)

(b)
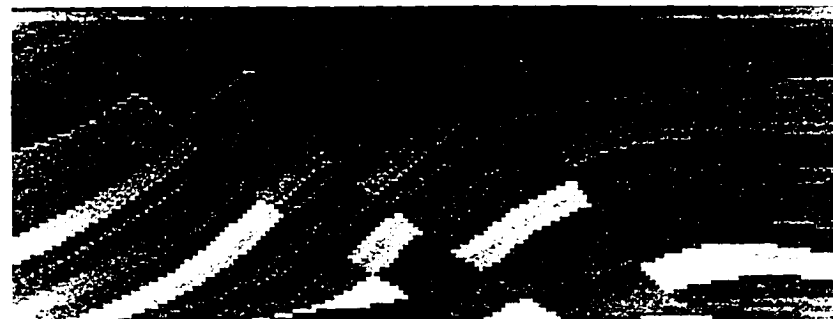
(c)

Figure 4.15: Asymptotic inversion: a) the reconstruction with a constant velocity background; b) the reconstruction with a background velocity of 20 percent higher than the correct velocity; and (c) the reconstruction with correct background velocity. Notice that the synthetic data is created with the distorted Born approximation.

Figure 4.16: McElroy site well location of CO_2 injection experiment.

a constant background velocity and, obviously, the result is poor. Figure 4.15b is the inversion with a background velocity 20 percent higher than the correct background velocity (figure 4.13). The basic features of the model can be recognized except the complicated detail. Figure 4.15c is the inversion with the correct velocity, which produces a result almost identical to that of the original model. This is not surprising, since the data is calculated using the same approximation to the inversion theory.
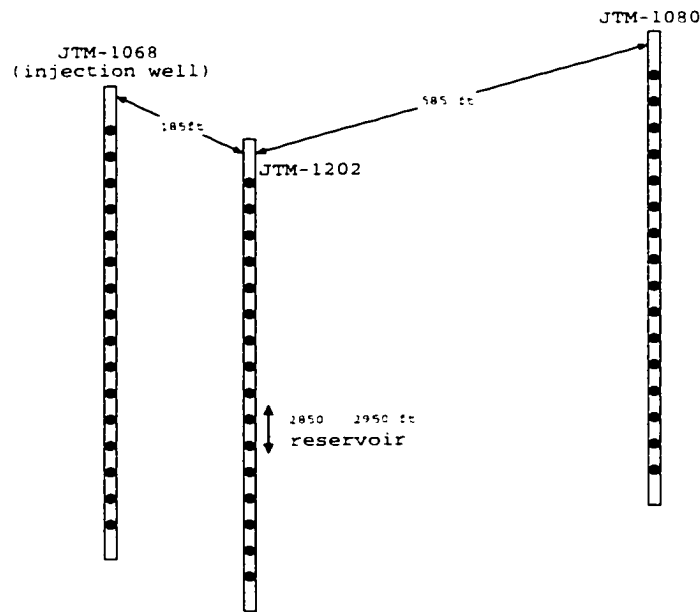
The algorithm is also applied to field data from McElroy test site in west Texas. These surveys have source and receiver apertures across the reservoir zone, as displayed in figure 4.16. Figure 4.17 shows the reconstructions of near offset data in the time domain without any data processing and inversion regulation. Both p- and s- slowness images indicate horizontal bedding between 2850 and 2950ft, as well as dip layers between 3000 and 3100ft. Although the traveltime tomogram successfully images the major layers, there is little evidence on the tomogram for the fine bedding inside the reservoir. The poorer resolution in the p- wave image relative to s- wave image is due to the directivity, i.e., the p- wave scattering is less efficient than that of s- wave in the near offset survey.
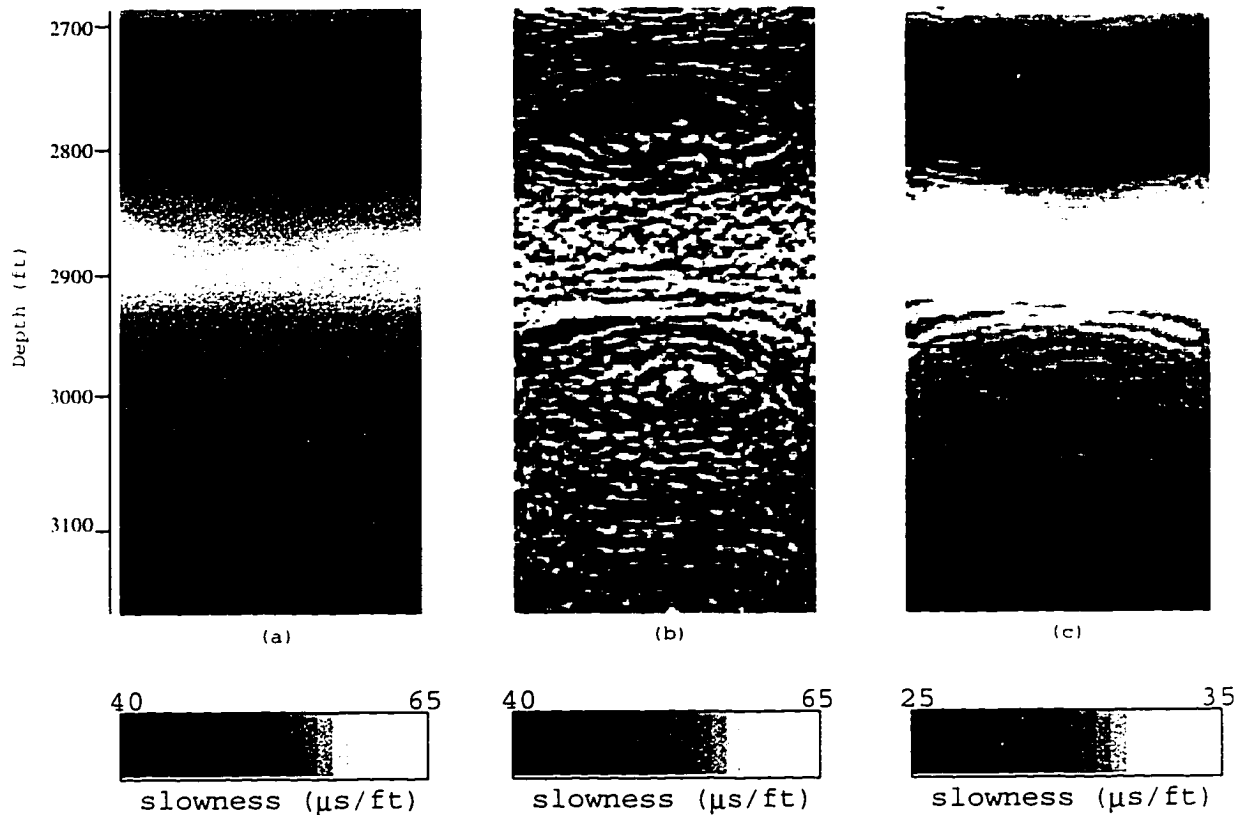
Figure 4.17: McElroy near offset wave asymptotic inversion: (a) traveltime tomogram, (b) and (c) diffraction tomogram reconstructed using pp and ss waves respectively.

The resolution of the diffraction tomogram is higher than that of the traveltime tomogram, but the useful details are buried in the noisy distortions due to the poor quality of the data, especially that of the amplitude. This poses a great difficulty to interpret these images. Therefore, some smoothing and enhancement of the field data has to be done before applying the inversion procedure as discussed in the following example of crosswell time-lapse monitoring survey at the McElroy test site.

In this example, we study the time-lapse slowness difference for the repeated surveys before and after co_2 injection between wells JTM-1068 and JTM-1202, and between JTM-1202 and JTM-1080. One study (Lumley, 1996) shows that the pore pressure changes, among other factors, lead to the change of seismic parameters, such as amplitudes and velocities of the elastic waves that can propagate and scatter

through the reservoir. As expected, the pore pressure increases near the injection well when CO_2 liquid is forced into the reservoir. The increase of the pore pressure leads to the effective pressure[8] drops, and consequently, the wave propagating velocity decreases. Figure 4.18 shows the the first arrival time and their changes observed in the McElroy long offset survey. The average difference of traveltime is about 10 to
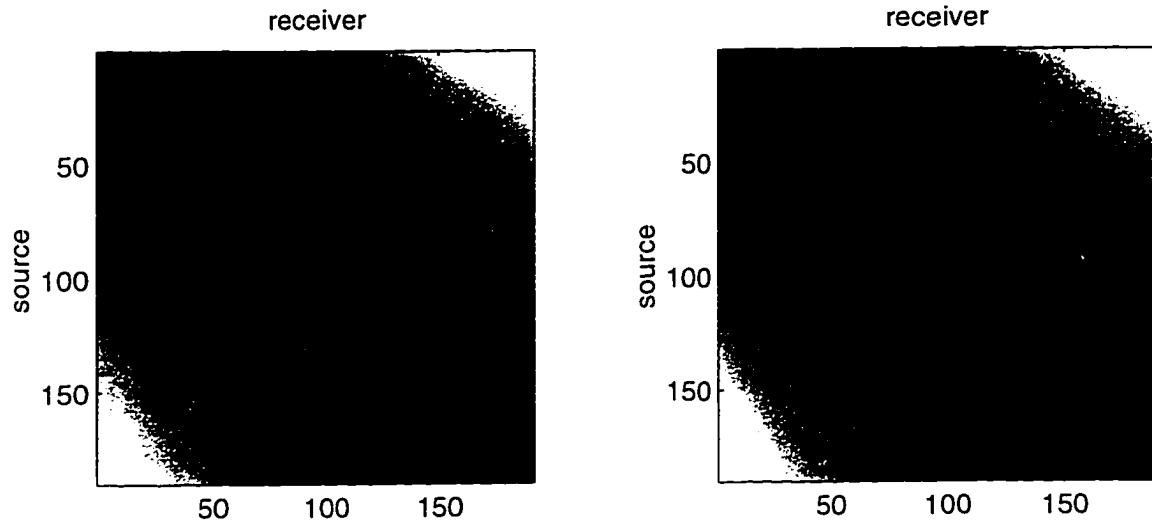
Figure 4.18: McElroy far offset first arrival picks: the left panel represents first arrival picks of the survey before CO_2 injection; the right panel represents first arrival picks of the survey after CO_2 injection.

15 percent as indicated in figure 4.19. Notice that the changes in figure 4.19 reflect only the first arrival time. The change of other characteristics of the wavefield are also evident in the following wave field gathers of the two surveys, as well as the spectra of the scattered field to be discussed next. Considering the practical problems of real data, such as limited aperture, measurement instrumentation, noise and etc.. some data processing and regulations to inversion has to be applied.

Assume that the spectral of the total field $U^t(\omega)$ can be written as

$$U^t(\omega) = U^0(\omega)U^s(\omega) = A(\omega)e^{i\omega\tau}$$

---

[8]Laboratory experiments show that both compressional and shear wave velocities in rocks strongly depend on effective pressure that is difference between confining pressure (overburden) and pore pressure: $P_{effective} = P_{confining} - P_{pore}$.
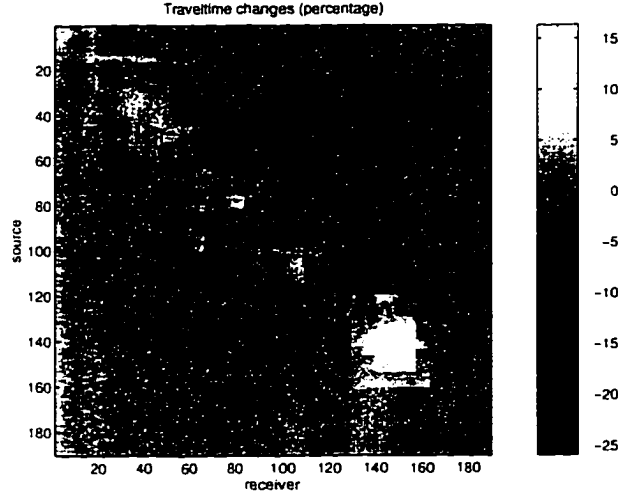
Figure 4.19: McElroy far offset first arrival picks changes due to CO_2 flood: the biggest change occurred in injection zone at depth of the reservoir.

where A is the amplitude and τ is traveltime, U^s is the scattered field, and $U^0 = A_0(\omega)e^{i\omega\tau_0}$ is the background field while A_0 and τ_0 is its amplitude and traveltime (notice that the definition of the scattered field and background field is different here). The above expression states that the total field is the background field modified by the scattered field U^s. Obviously, the scattered field can be derived as

$$U^s = \frac{A(\omega)}{A_0(\omega)}e^{i\omega(\tau-\tau_0)}.$$

The τ can be found by taking derivative of the total field with respect to ω, i.e..

$$\frac{\partial U^t(\omega)}{\partial \omega} = U^t(\frac{A'(\omega)}{A(\omega)} + i\tau),$$

where $A'(\omega) = \partial A(\omega)/\partial \omega$, and therefore,

$$\tau = \Im\{\frac{\partial U^t(\omega)}{\partial \omega}/U^t\},$$

where the symbol $\Im\{\cdot\}$ represent the imaginary part of a complex quantity. Notice also that in this formulation, if the traveltime τ_0 is taken as the first arrival time,

(a)

(b)

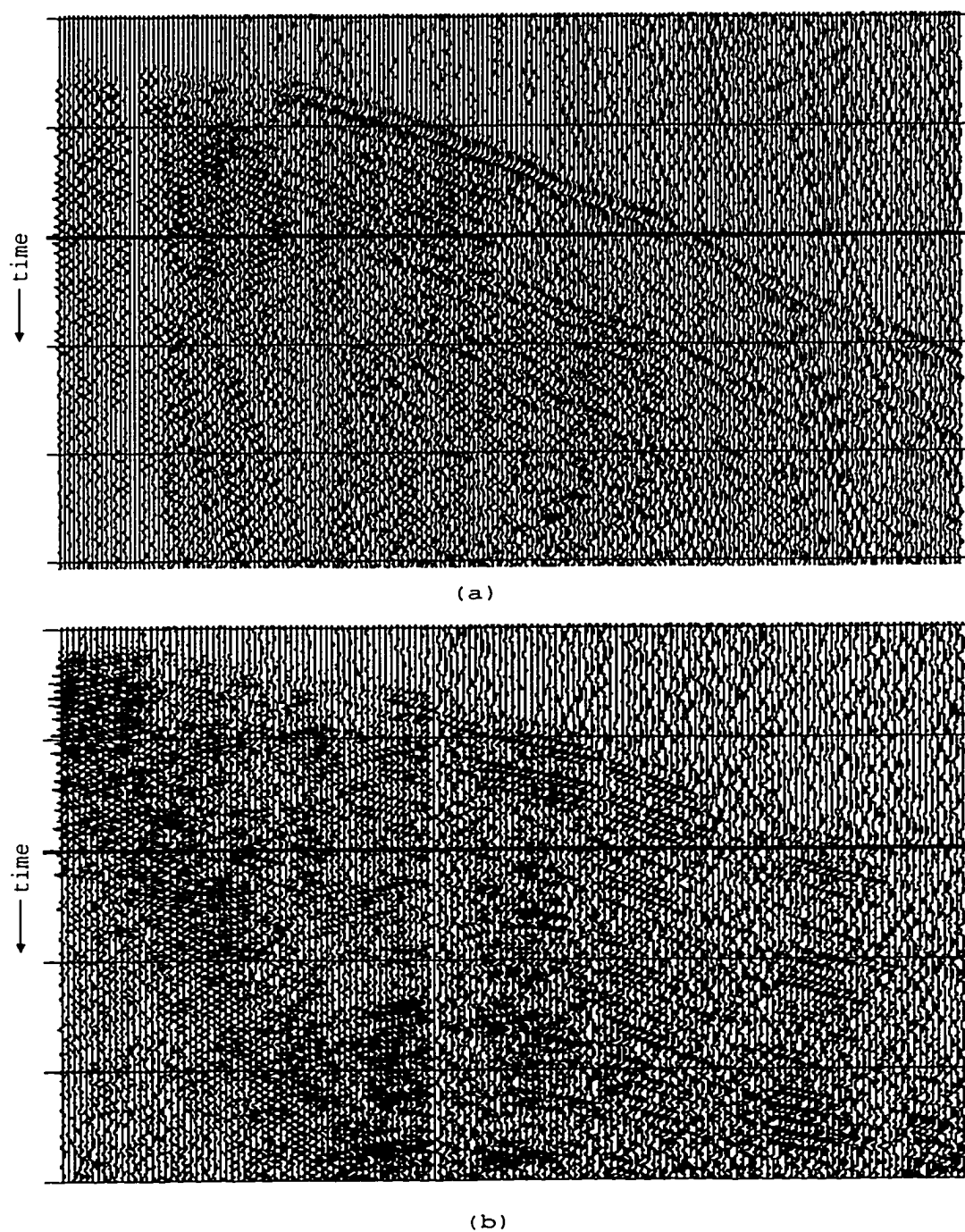Figure 4.20: McElroy far offset data sets: (a) a common source gather of prior CO_2 injection survey, and (b) a common source gather of posterior CO_2 injection survey.

then the prior knowledge can be incorporated into the picking process. Since different downhole sources are used during the two surveys, the amplitudes are less useful in terms of time lapsed monitory.

Figure 4.21a and b shows the real part spectra of the scattered field from the two near offset surveys before and after the injection, according to the formulation described above. Unfortunately, the receiver aperture of the second survey is not complete, making the time-lapse comparison difficult. Figure 4.22a and b shows the real part spectra of the scattered field from two surveys before and after the injection, according to the formulation described above. Notice that the amplitude of the wavefield is discarded.

Figure 4.21: The spectra of the scattered waves from McElroy near offset survey (real part): (a) is from the survey prior to CO_2 injection; and (b) is from the survey following the CO_2 injection. Notice that both the source and receiver aperture of the second survey are not as deep as that of the first survey.

From figures 4.21 and 4.22, one can see the patterns corresponding to layering of the medium, even through the amplitude information is discarded. Applying the inversion method described by equation 4.28 and smooth filter to the data shown in figure 4.22, we obtained the results consistent with prior known geological information. The figure 4.23 displays the diffraction tomogram of the slowness reconstructed
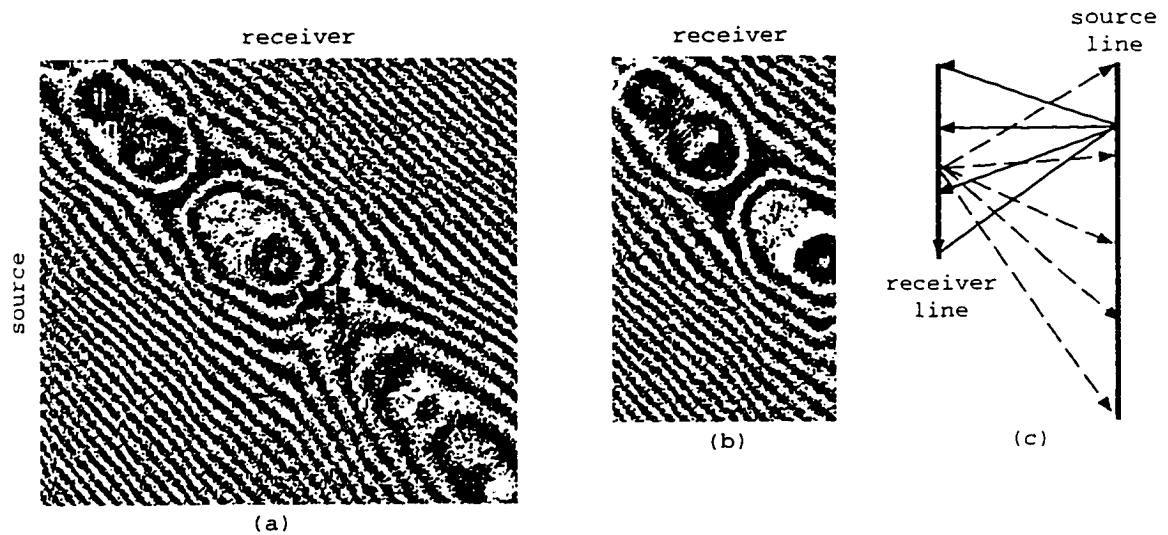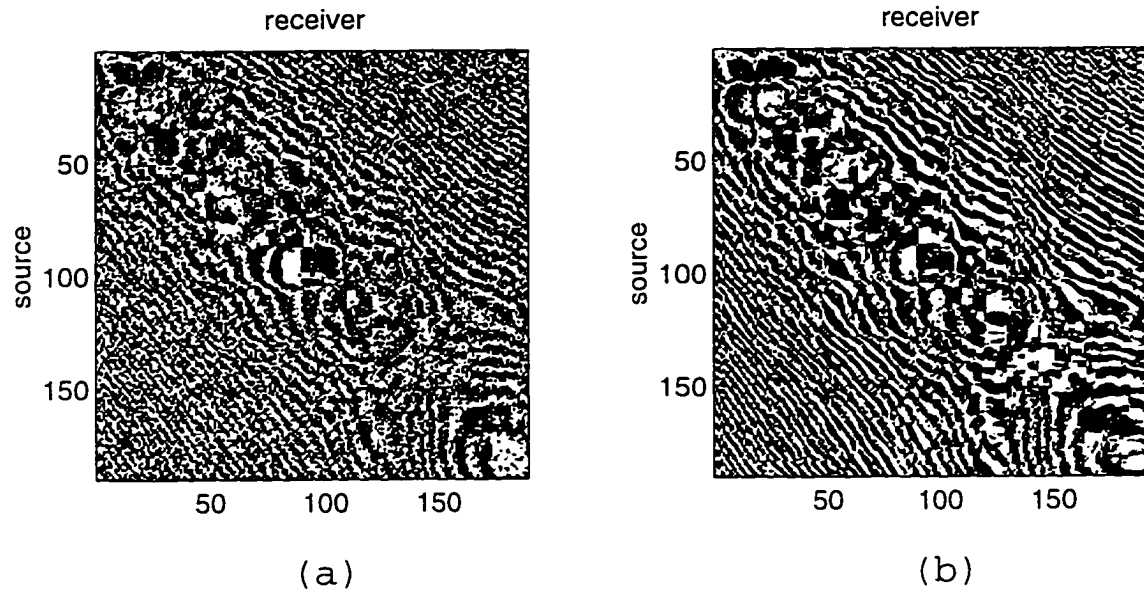
Figure 4.22: The spectra of the scattered waves from McElroy far offset survey (real part): (a) is from the survey prior to CO_2 injection; and (b) is from the survey following the CO_2 injection.

using McElroy near offset data. The figure 4.24 displayed the slowness images from the far offset data set before and after the injection. The visible fault system in the prior injection image, which is the up panel in figure 4.24, is consistent with prior geological information. However, after approximately one year of CO_2 flood, the average slowness increased up to ten to fifteen percent. The fault system seems to be less obvious in the post injection image.

Figure 4.25 is the difference between the two tomographic results. Some of the anomaly in figure 4.25 may be due to the data quality of the different surveys. but the large slowness increase in the injection zone at the depth of the reservoir is clearly the consequence of the CO_2 injection. The anomaly slowness increases at the reservoir zone. The visible slowness increases inside the reservoir is less ambiguous and possibly due to the transient CO_2 pressure.

Figure 4.23: McElroy near offset wave asymptotic inversion: the left and right panels are the slowness images from the near offset dataset prior to and following the CO_2 injection, respectively. The noise in the low-right corner of the post injection image is due to incomplete aperture.
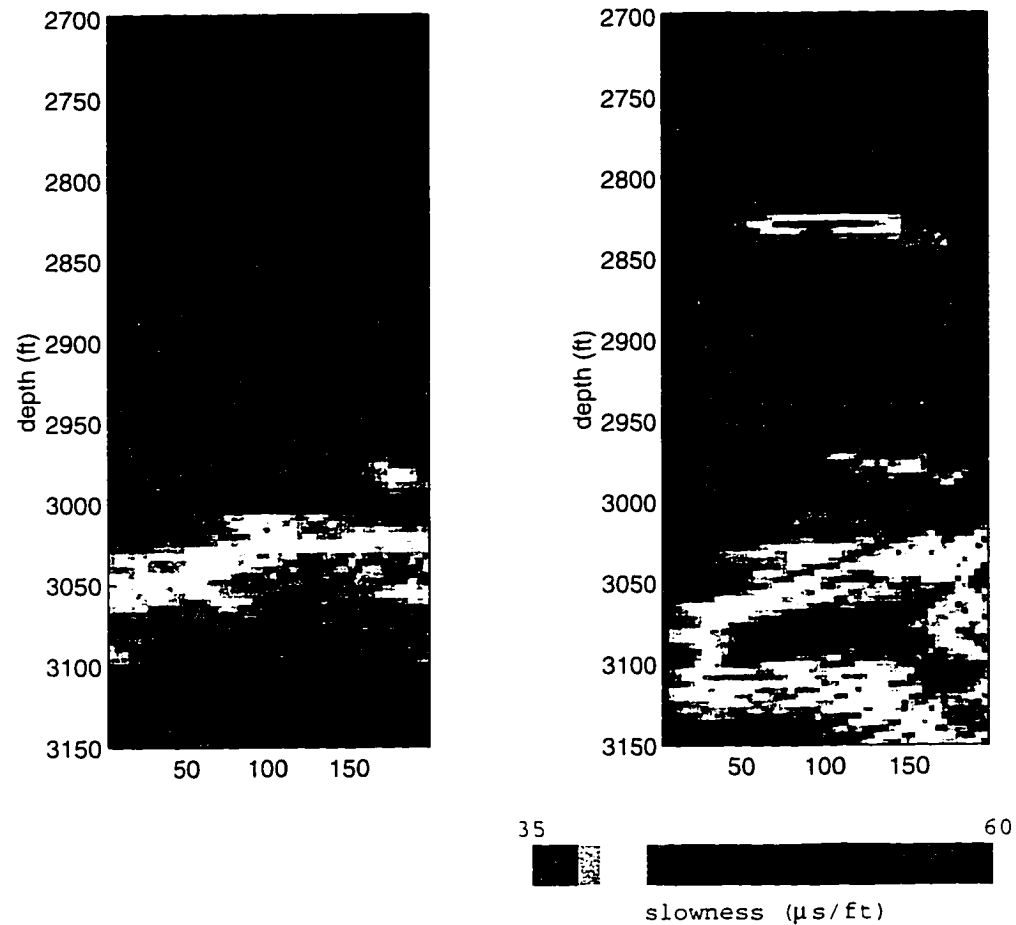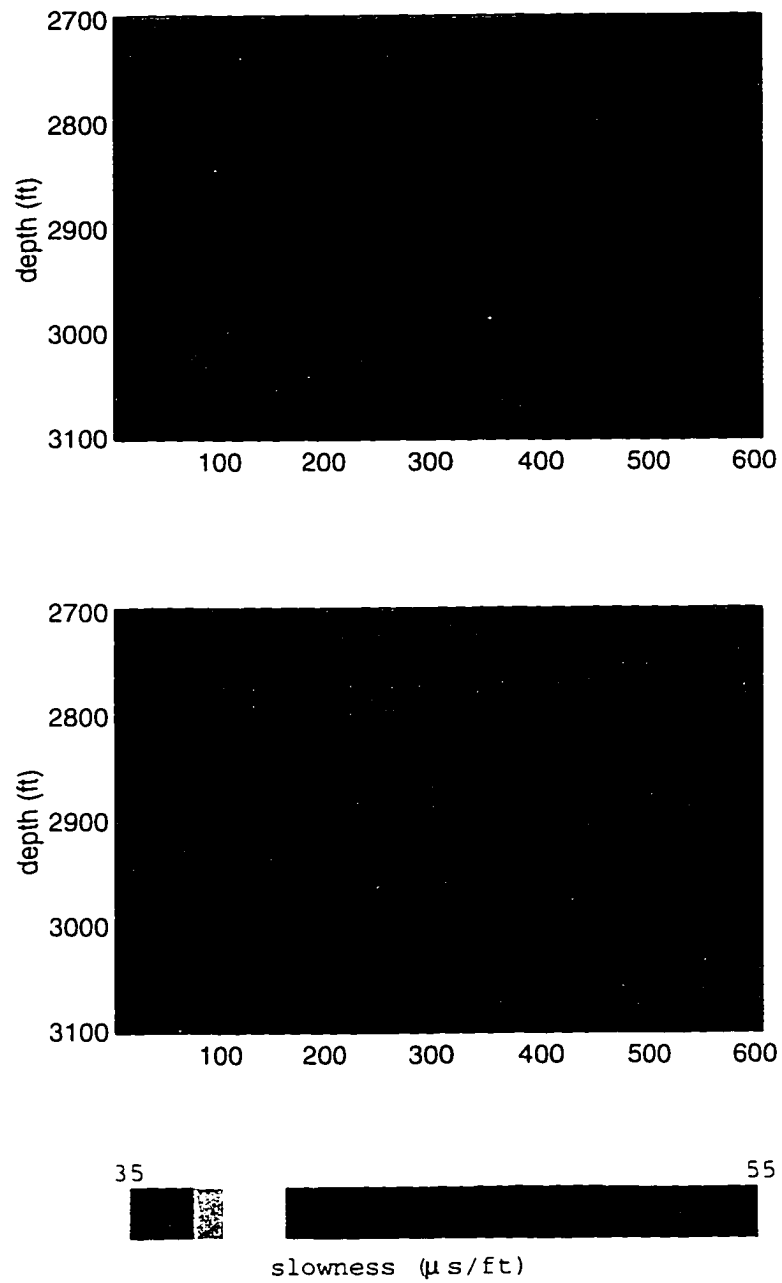
Figure 4.24: McElroy far offset wave asymptotic inversion: the up and low panels are the slowness images from the far offset dataset prior to and following the CO_2 injection, respectively.
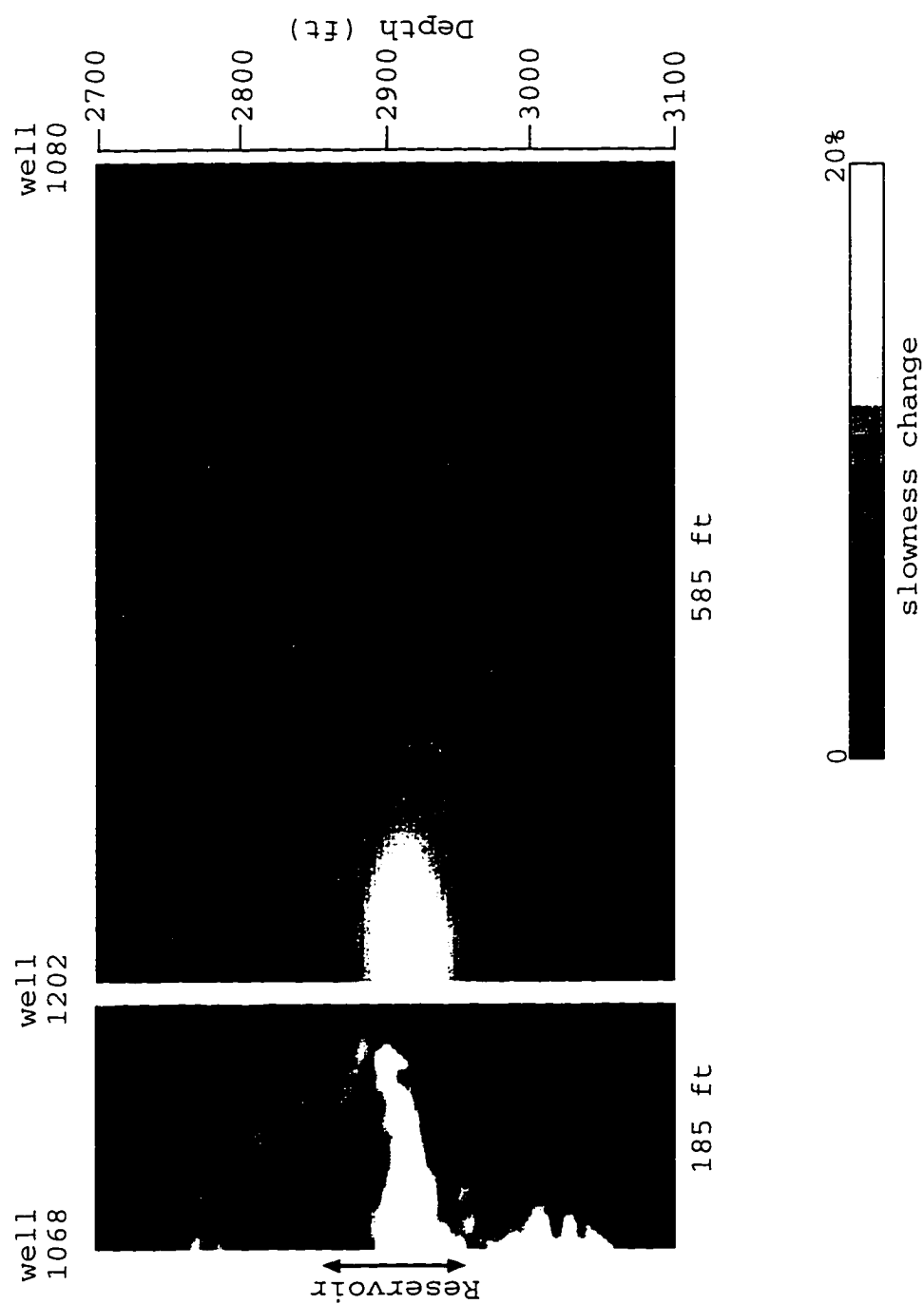
Figure 4.25: The time-elapsed slowness change of McElroy test site: the image is the difference between the results using the data sets before and after CO_2 injection.

4.5 Conclusions

Using the the wave asymptotics, a general Fourier transform is derived that has an approximate inverse, in the sense that the inverse operator recovers the most singular part of the discontinuities of the medium. The resultant algorithm is similar to the Kirchoff migration and simple to implement. The numerical experiment and field data inversion demonstrate that the algorithm is flexible and can be used to image complicated subsurface media. One should emphasize that asymptotic wave theory is subject to fundamental restrictions which put limitations on its applications. These restriction involve the physical parameters: frequency of the wave. scale and gradient of the medium. If any of these restrictions is violated. asymptotic wave theory becomes progressively invalid.

Chapter 5

Random Medium Inversion Using Diffraction Tomography

Complex systems, such as the earth's medium with fine or multicomponent structures, cannot always be described in a deterministic fashion because of either inherent irregularity or lack of knowledge of the phenomena observed. We may treat these types of media with complicated distribution of small scale inhomogeneities as random. The random medium may be viewed as a particular realization of random processes. The wave propagation description of the earth's medium is complicated by such heterogeneities and discontinuities in which the wave energy is scattered randomly. This chapter studies the inverse scattering problem of random media and determines the statistical properties by extending the diffraction tomography procedure discussed in previous chapters. The resolved statistical quantities are appropriate to be used in identification of fracture scales and orientations. In addition to being used to identify the scales and orientations of the inhomogeneities, the estimated statistical quantities can also be directly integrated into geostatistical simulations.

5.1   Diffraction vs. diffusion in random media

Waves propagating in the random media are often treated by using the diffusion equation to calculate the effective transport properties of random media. Laboratory

107

measurement and modeling results (Mukerji, 1995) show that in the effective medium or long wavelength limit, the heterogeneous medium can be modeled as a homogeneous (possibly anisotropic) medium with an effective elastic modulus and seismic velocity.[1] It is based on the principle that the wave energy density should be uniform when averaged over length scales larger than the size of the inhomogeneity. Figure 5.1 shows some examples of random medium. They have different densities of the
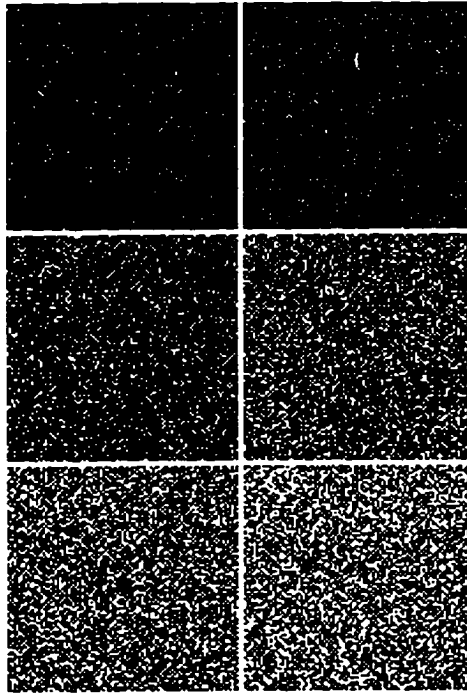
Figure 5.1: The medium with different concentrations of the random distributed scatterers is approximated as an effective medium. The wave scattering can be treated as a diffusion problem. The top and bottom panels are for low and high concentration of scatters respectively.

uniformly random distribution and can be approximated as effective media. However, it is not enough to obtain average transport properties of the media. In many

---

[1]The simplest approximation to a random medium is the effective medium theory according to which waves propagate as if they were in a homogeneous medium whose properties and effective parameters are constant. This approximation is valid in general but is restricted to propagation over distances of the order of, or not much larger than, a wavelength. It is useful in the analysis of waves in confined regions but cannot account for the localized phenomena.

geophysical situations, random distributions may be locally clustered (figure 5.2 and the clustered inhomogeneities will scatter wave fields collectively. The information beyond average properties are contained in the second moment of the wave field. The second order statistics of the random media are more appropriate in geophysical and geostatistical applications.
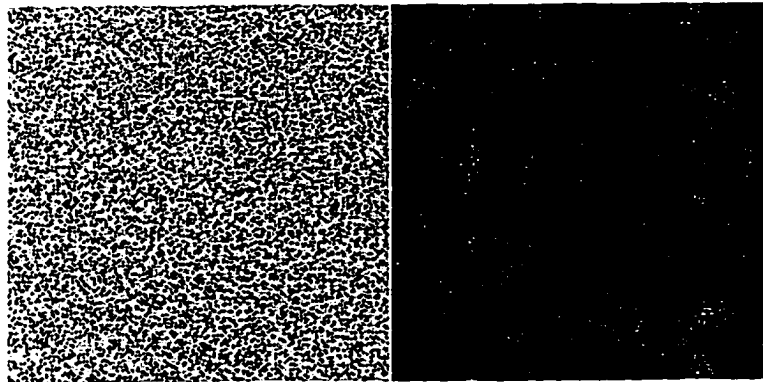
Figure 5.2: An locally clustered medium: the left panel displays a statistically homogeneous medium, while the right panel shows a locally clustered random medium.

To obtain these statistical properties, we examine the wavefield correlations using full wave representations, either scalar or vectorial. The spatial power spectra of the scattered fields are utilized to characterize patterns of inhomogeneities. Notice that the detailed spatial and temporal variations of the wave field, therefore the medium in which waves propagate, can never be retrieved from the moments of wave field. To obtained such information, there is no substitute for an exact solution to the problem.

We assume the large scale component of the elastic parameters is known and the perturbations are random functions of spatial variables with zero mean. When the large scale component of the elastic parameters is inhomogeneous, the asymptotic inversion is used, as discussed in Chapter 5. By probing the medium with multiple sources and receivers, such as in cross well or 3D seismic survey, the second order statistics of the medium are inferred from the second moment of the scattered field by extending diffraction tomographic inversions. The inverted correlations are significant in the following ways: (1) they are consistent with the wave propagation theory and have definite physical meaning; (2) they can be multi-dimensional i.e., the obtained

correlations are in both horizontal and vertical directions.

5.2   Random media and wavefield characterization

5.2.1   Random media simulation

The scattering properties of the medium depend not only on the mean but also on the correlation of the randomly varying part of the material property. Let $m_i(\mathbf{x})$, $i = 1, 2, 3$ be a random isotropic elastic medium, where $\mathbf{x} = (x, z)$, which may consist of p-wave velocity. v_p/v_s ratio and density. The function $m_i(\mathbf{x})$ can be decomposed into $m(\mathbf{x}) = m^0 + m'(\mathbf{x})$, where m^0 represent the large scale inhomogeneities while $m'(\mathbf{x})$ represents small scale inhomogeneities. The correlation of the fluctuation is a measure of the size and shape of a typical irregularity in the medium. The correlation function is well understood if $m(\mathbf{x})$ is a random function of time. such as the density of the atmosphere when temperature fluctuates. In that case, the assembly average[2] may be taken. There is a general way of characterizing a random variable by means of averaging over time or space, which in principle must be performed by repeating the experiment many times on different samples. This tacit consideration is called the ergodic assumption, as depicted in figure 5.3.

Notice that these averages may or may not have a direct connection with particular quantities that are found in a particular sample. In practice, we replace the ensemble average by the temporal average so long as the process is statistically stationary and the total amount of time is large enough to encounter sufficient members of the ensemble.

In a solid medium, however, the fluctuation of the property $m'(\mathbf{x})$ is not a function of the time at least for the durations of seismic experiments. By analogy to the ergodic assumption for temporal stochastic process, the ensemble average of the

---

[2]If $m(\mathbf{x})$ is a random function of the coordinates $\mathbf{x}$, there exist an infinitely large number of random functions m which differ from each other but are described by the same probability density. This infinitely large family of possible function $m(\mathbf{x})$ is called an assembly. The assembly average of m at the point $\mathbf{x}$ is obtained by taking the average of $m(\mathbf{x})$ over all members of the assembly. This operation is denoted as by $< m(\mathbf{x}) >$.
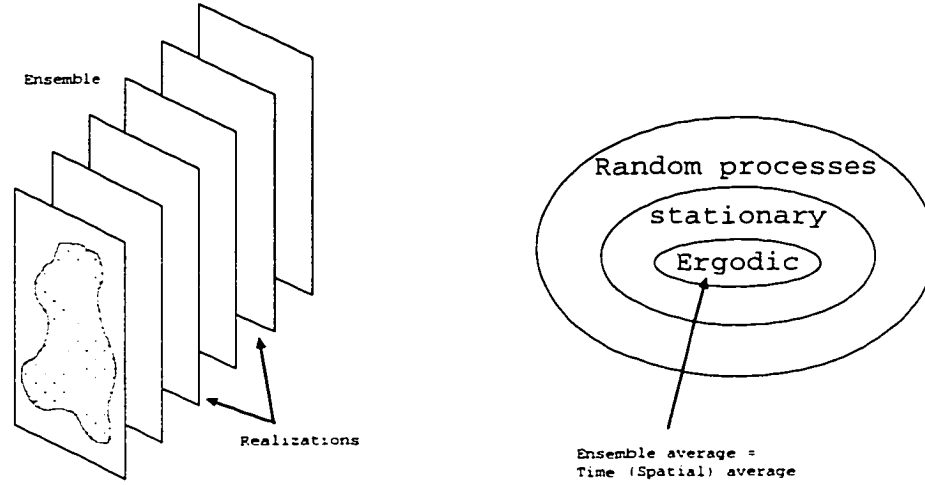
Figure 5.3: To obtain complete statistics of a process, an ensemble of realizations is needed. In ergodic processes, the complete statistics can be determined from any one realization, i.e., every realization carries an identical statistical information.

spatial random functions is approximated as the average over the volume. assuming that the fluctuation $m'(\mathbf{x})$ has spatially invariant statistical properties within the volume considered. It can be shown that the ensemble average of the power spectrum is the average correlation function over the considered volume (Papoulis, 1965). Under these assumptions, correlation is spatially invariant.

The correlation function can have various functional forms depending on the nature of the irregular medium such as the Gaussian form, the exponential form, fractal form and etc. The form of the probability distributions governing $m_i(\mathbf{x})$ and the form of the correlation function are quite independent of each other. A function $m_i(\mathbf{x})$ obeying Gaussian statics may or may not have a Gaussian correlation function. and vice versa. Assuming the random function $m_i(\mathbf{x})$ has an exponential autocorrelation function (Ikelle, 1993), for example,

$$c_i(\xi, \eta) = exp(-\sqrt{\frac{\xi^2}{a^2} + \frac{\eta^2}{b^2}}), \tag{5.1}$$

where a and b are the autocorrelation length scales, the spectrum of the media in the

Fourier transform domain is constructed as

$$M_i(k_x, k_z) = |C_i(k_x, k_z)| exp(i\theta(k_x, k_z)),$$ (5.2)

where $C_i(k_x, k_z)$ is the Fourier transform of the correlation function c_i and the uniform distribution $\theta \subset [0, 2\pi]$ is defined as the phase of the spectrum M_i. The random function m_i is then generated via inverse Fourier transform, i.e.

$$m_i(x, z) = FT_{2d}\{M_i(k_x, k_z)w(k_x, k_z)\},$$ (5.3)

which has the desired autocorrelation function. Notice that the filter $w(k_x, k_z)$ is designed to remove the D.C. component. Notice that only phase is randomized. therefore, the resultant model may not be truly random.
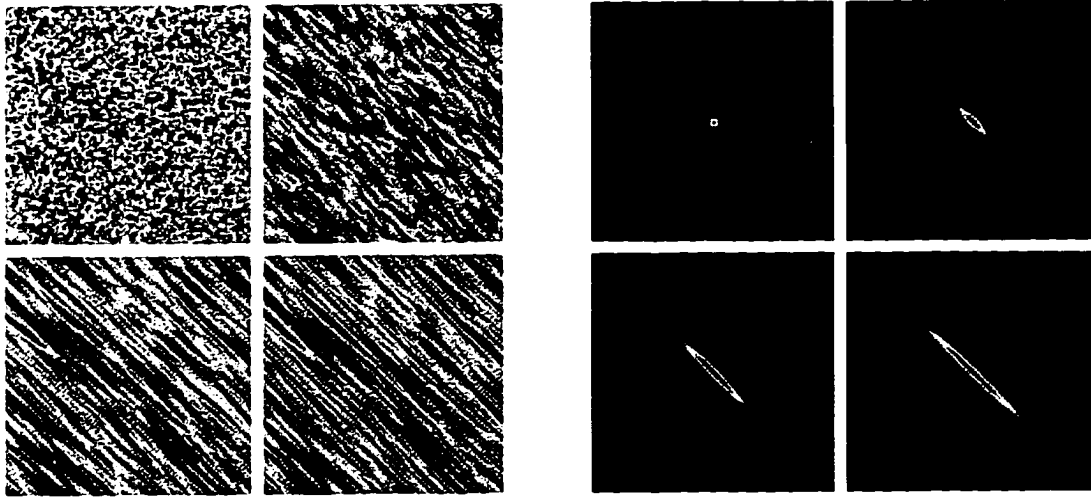
Figure 5.4: The correlation function and realizations: the right panel is the correlation functions with different vertical and horizontal correlation length a's and b's. The left panel is the realizations generated with the correlation functions.

In synthetic simulation, the random distribution is characterized by given autocorrelation functions. With figure 5.4, we show the exponential autocorrelation functions of various correlation length. The realizations are intended to describe the inhomogeneities of the medium as isotropic or elongated in a specified direction. The

correlation between the perturbations of the elastic parameters is still an open question which and beyond the scope of this paper. We assume the cross-correlations between the three elastic parameters are independent.

5.2.2   Weak and strong fluctuations

In order to describe the statistical average of scattered field energy $< UU^* >$, weak and strong fluctuations of the wavefield are considered separately. As a measure of wavefield fluctuations, a parameter ϵ is defined as the amplitude ratio of the incoherent scattered field to coherent incident field (Shapiro, 1993), i.e.,

$$\epsilon = \frac{|U(L)|}{|U_0(L)|} \approx 2\alpha L, \tag{5.4}$$

where α is the scattering coefficient of the mean field and L is a travel distance. If the correlation distance r_0 of the inhomogeneities is of the same order or larger than the wavelength λ then the coefficient α can be roughly estimated as $\sigma^2 k^2 r_0^2$, where $k = 2\pi/\lambda$ and σ^2 is the variance of the fluctuations. In figure 5.5 we depicted
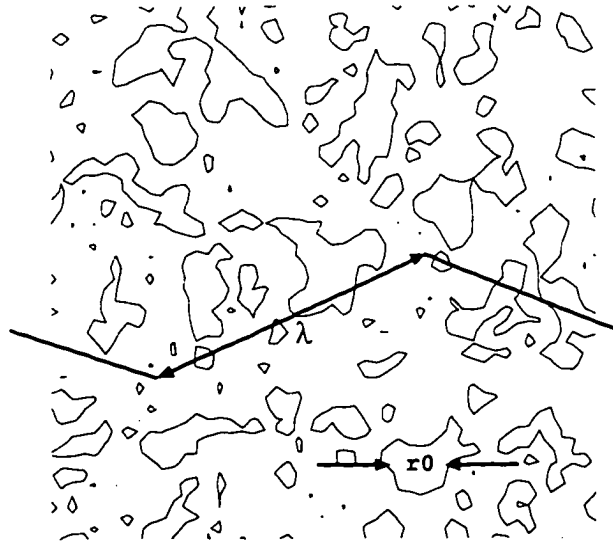

Figure 5.5: The scattering vs. the scale of inhomogeneity: the random spatial distribution function $m_i(\mathbf{x})$. The weak scattering can be interpreted as $\lambda >> r_0$, where r_0 is the correlation length and λ is the average wavelength of the incident wave in the medium.

the average wavelength λ and the correlation length r_0 of the fluctuations of elastic parameters. The weak scattering can be interpreted as $\lambda >> r_0$. which is used to gauge the wave field modeling. In a random medium without energy dissipation. the coherent field and its intensity attenuate due to the energy transfer from U_0 to U. The region of weak wavefield fluctuations is limited to small propagation distances where $\epsilon << 1$. For large L or large α, $\epsilon >> 1$ strong wavefield fluctuations are expected. In random media, the wavefield behaves differently in regions of weak and strong wavefield fluctuations: we solve the problem of small wavefield fluctuations using the first Born approximation, while for the case of strong fluctuation. the asymptotic method discussed in Chapter 5 is used.

5.2.3   Wave field simulation

In the following, wave propagation is simulated using finite difference method. The observation system consists of one shot and multiple receivers in a transmission geometry. The random models are (1) the realization simulated using exponential correlation function and (2) the realization simulated using Gaussian correlation function. The possible errors include those that result from finite grid size and finite simulation dimensions. In the implementation, we make sure that the first two statistical moments are correct. To satisfy the condition of stability and dispersion required in the finite difference solver, the limits to p-wave velocity and s-wave velocity variations are imposed. These limits are large enough so that statistical parameters do not change.

In Figure 5.6, we show the geometry of the calculation. The receivers are placed at positions having equal distance to the source location. The source is polarized in x direction. This geometry is easier to observe the first arrival and the effects of the radiation pattern. The simulation results are shown in Figure 5.7 and 5.8. We can see that although the first arrivals are not sensitive to the inhomogeneities, the scattering is energetic and rich. In this chapter, the data for the synthetic examples are not simulated using the finite difference method, which requires extensive computer power. The Born approximation is used instead since the conditions of the approximation is satisfied by choosing appropriate background medium.
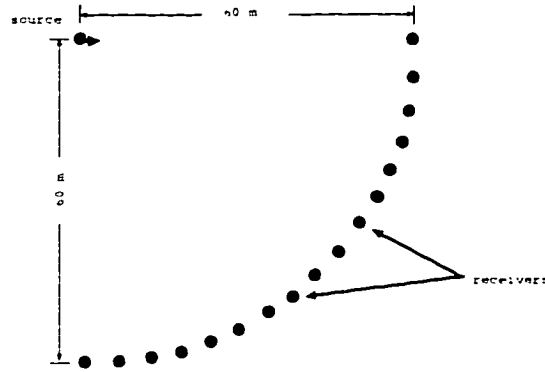
Figure 5.6: The geometry for calculating wave field with finite difference.

5.3   Inversion of correlation functions

Waves scattered by random media are very noisy because of the multiple scattering. If large scale variation of medium properties can be distinguished from their small scale fluctuations due to random inhomogeneity, then it is possible to invert the statistical properties of random media. Instead of multiple independent realizations, the wave field observed along the source and receiver aperture is used to compensate for the randomness. We assume the large scale component of the elastic parameters is known and the perturbations are random functions of spatial variables with zero mean. We consider the inverse problems of determining the spatial correlation function of the perturbation functions with the measured fluctuations of the scattered fields and their spatial correlations [3]. Under the hypothesis of stationarity, the autocorrelation function depends only on the correlation length. In this section we derive the procedures to recover the correlation function of the inhomogeneity function for various practical situations and illustrate the derived methods with numerical examples. For synthetic example, we use the Born approximation to simulate wave propagation in the random media of various correlation functions.

---

[3]For the assumed statistical homogeneous medium, the correlation function depends only on the coordinate differences $r = r_2 - r_1$. For $r = 0$, the correlation function achieves its maximum and equal to the mean square fluctuations. The first moment of wave field gives the way that the incident wave is attenuated on passing though the medium. The second moment $< UU^* >$ is the autocorrelation function of the wave field which determines the power or 'visibility' in terms of optics.

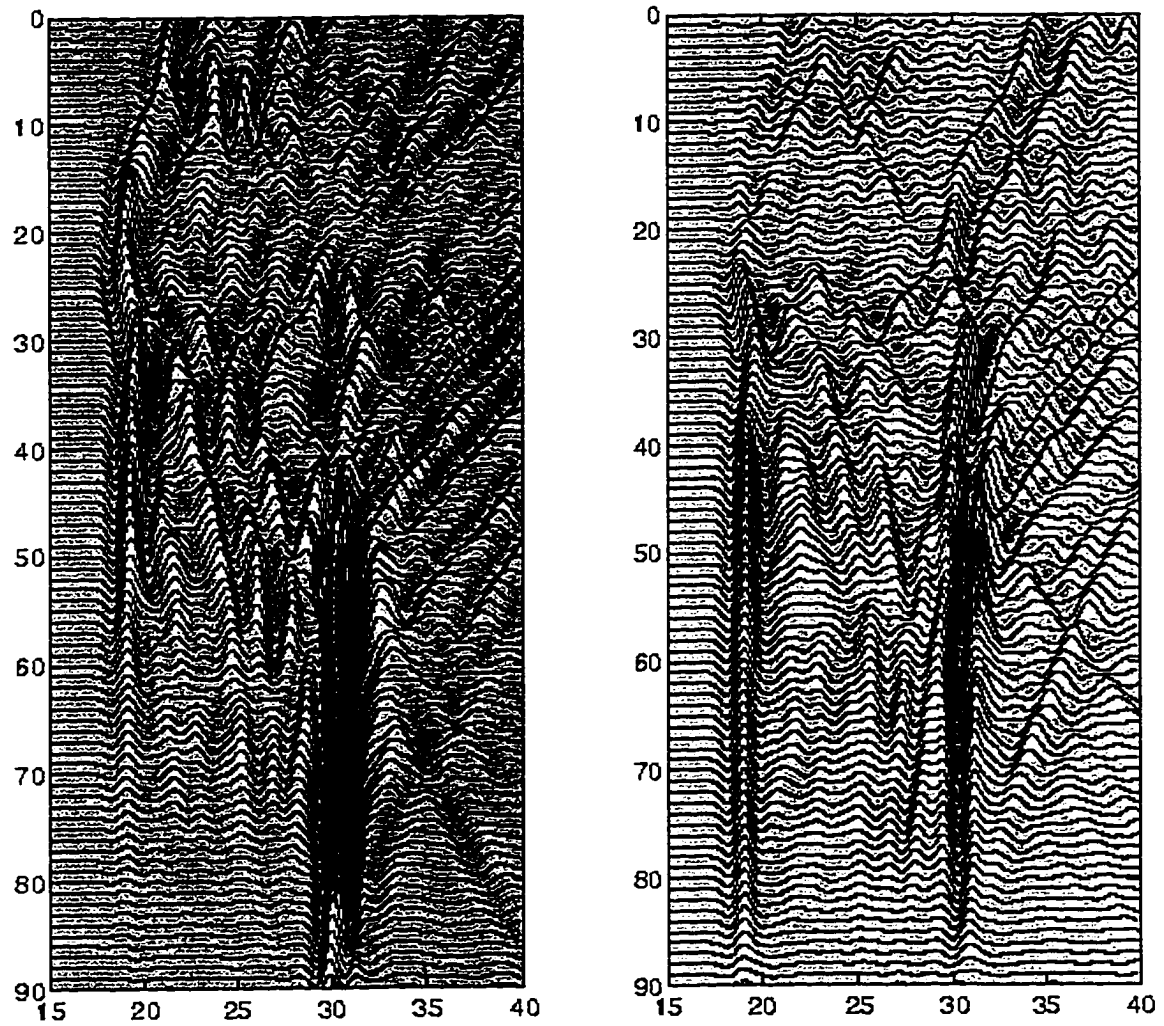Figure 5.7: The finite difference simulation of the wave propagation in a random medium with an exponential correlation. The left panel is the horizontal component and the right panel is the vertical component.
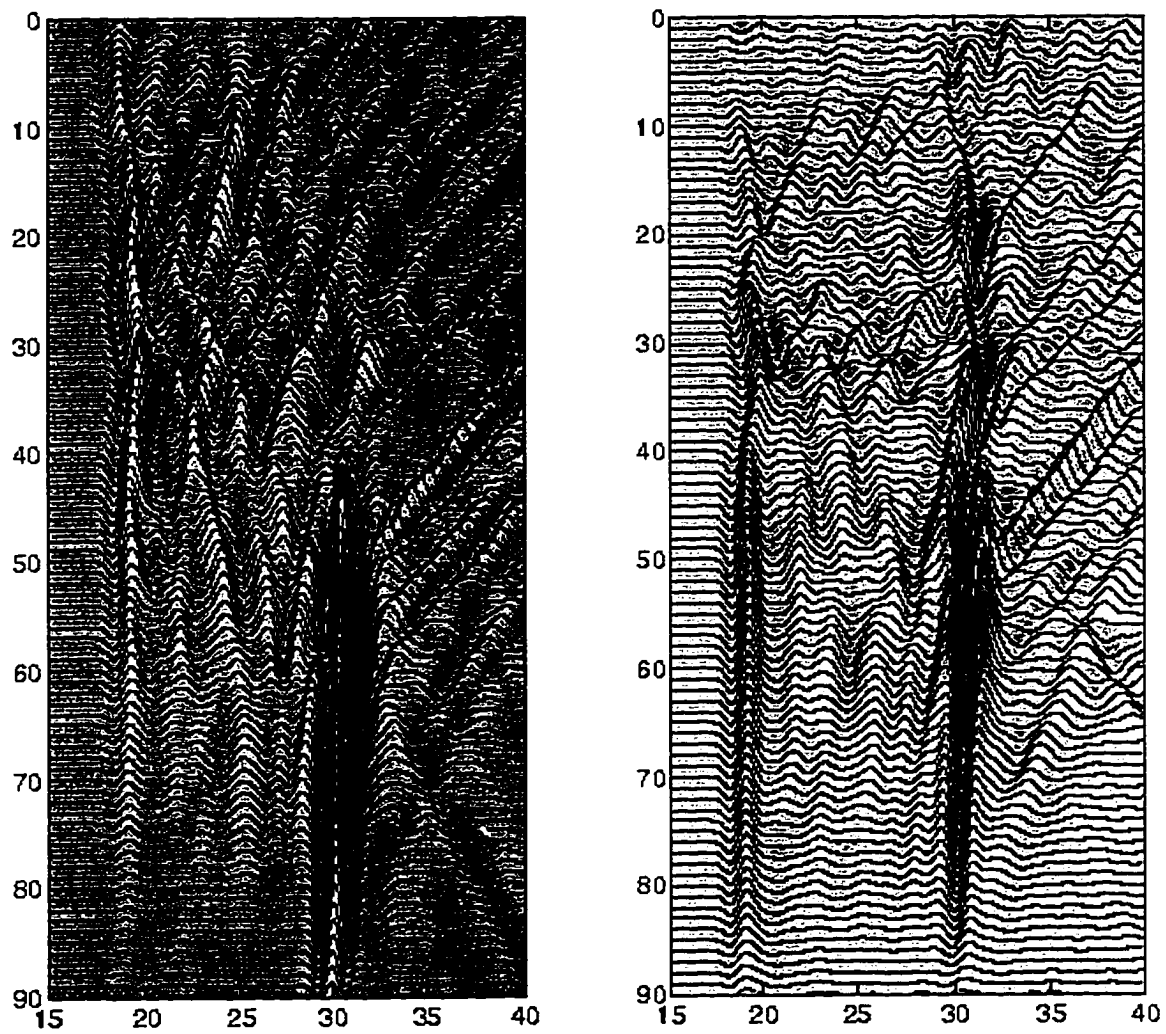
Figure 5.8: The finite difference simulation of the wave propagation in a random medium with Gaussian correlation. The left panel is the horizontal component and the right panel is the vertical component.

5.3.1 Case of the statistically homogeneous media

We first consider a simple case of scale wave in a statistically homogeneous medium. The scattered field $U(\mathbf{s}, \mathbf{r})$ under the Born approximation can be written as (see Chapter 2):

$$U(\mathbf{s}, \mathbf{r}) \sim - \int_V m(\mathbf{x}) G(\mathbf{x}, \mathbf{s}) G(\mathbf{r}, \mathbf{x}) d\mathbf{x}, \qquad (5.5)$$

where $m(\mathbf{x}) = \omega^2(1/c_0^2(\mathbf{x}) - 1/c^2(\mathbf{x}))$ and G is the Green's function. Taking the Fourier transform of along source and receiver array, e.g., with respect to source and receiver well lines respectively in the case of crosswell survey (see Appendix A), one obtains

$$U(\mathbf{k}', \mathbf{k}) \sim f(\mathbf{k}', \mathbf{k}) \int_V m(\mathbf{x}) e^{-\imath(\mathbf{k}' - \mathbf{k})\mathbf{x}} d\mathbf{x}, \qquad (5.6)$$

where $\mathbf{k}'$ and $\mathbf{k}$ is incident and scattering wave vector, respectively; and $f(\mathbf{k}', \mathbf{k})$ is a function resulted from plane wave decomposition that depends on the dimension of the problem (see Appendix A). Without confusion, we use the symbol U for both of the scattered wavefield in the spatial domain and Fourier domain. They are distinguished by the function argument of $\mathbf{x}$ or $\mathbf{k}$.

The second moment of the scattered field $< U(\mathbf{s}, \mathbf{r}) U^*(\mathbf{s}, \mathbf{r}) >$ in the spatial domain can be evaluated through its spatial Fourier domain representation, i.e., $< U(\mathbf{s}, \mathbf{r}) U^*(\mathbf{s}, \mathbf{r}) > = FFT^{-1}\{|U(\mathbf{k}', \mathbf{k})|^2\}$, while the power spectrum $|U(\mathbf{k}', \mathbf{k})|^2$ is directly related to the correlation of the inhomogeneity according to diffraction tomography theory, i.e.,

$$|U(\mathbf{k}', \mathbf{k})|^2 \sim \int_V R(\xi) e^{-\imath(\mathbf{k}' - \mathbf{k})\cdot\xi} d\xi, \qquad (5.7)$$

where $R(\xi) = < m(\xi + \mathbf{x}) m(\mathbf{x}) >$ is the correlation of the object function m [1]. Obviously, we can invert the correlation function $R(\mathbf{x})$ from equation (5.7) by using

---

[1] Using relative coordinates $\xi = \mathbf{x} - \mathbf{y}$, $\int \int m(\mathbf{x}) m(\mathbf{y}) e^{-\imath\mathbf{k}\cdot(\mathbf{x}-\mathbf{y})} d\mathbf{x} d\mathbf{y} = \int R(\xi) e^{-\imath\mathbf{k}\cdot\xi} d\xi$, where the correlation function $\mathcal{R}(\xi) = \int m(\mathbf{y}) m(\mathbf{y} + \xi) d\mathbf{y}$.

diffraction tomographic procedure (described in Appendix A). The inversion procedure is demonstrated with a synthetic example shown in figure 5.9. The left panel in figure 5.9 shows an exponential correlation. The correlation length. $a = b = 0.5$. is described in section 2 of this chapter. The right panel is the random velocity perturbations generated with an exponential correlation function. The maximum amplitude of the random velocity perturbation is ten percent of background velocity. The global average of the perturbation is less than 0.01 percent. Figure 5.10 shows the scattered
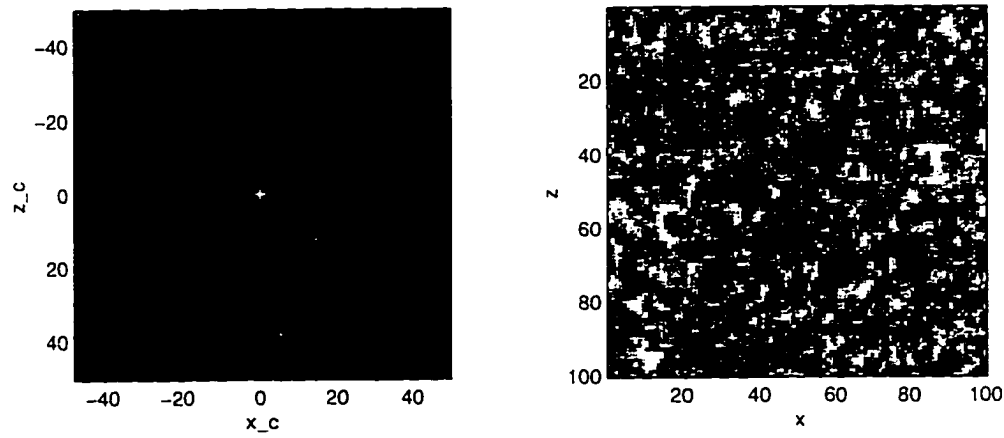

Figure 5.9: A random medium with an exponential correlation with the correlation length of one meter: the left and right panels are the correlation function and the random medium generated, respectively.

field amplitude simulated and recovered correlation of the inhomogeneity. The field is calculated using the Born approximation. As expected, the in-line scattering is stronger than that of off-line. This is indicated as stronger amplitude along the diagonal in the left panel. The inverted correlation function is shown in the right panel of figure 5.10, which is almost as the same as that of the model. This is due to the fact that the wave field calculation and inversion are carried out with a fully circular aperture.

For the limited aperture, the quality of the reconstruction will be degraded. as demonstrated in figure 5.11. The left and right panels are the wavefield amplitude and correlation function reconstructions with a semi circular aperture. One can see that the recovered correlation function is smeared in the horizontal direction. One

Figure 5.10: The inversion of medium correlation using Born approximation: the left panel is the wave field amplitude generated using the circular aperture; and the right panel the inverted correlation of the medium.
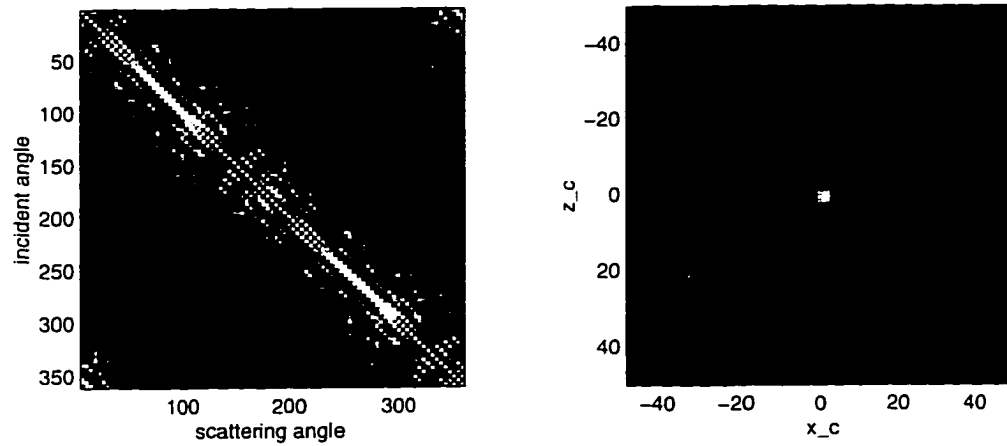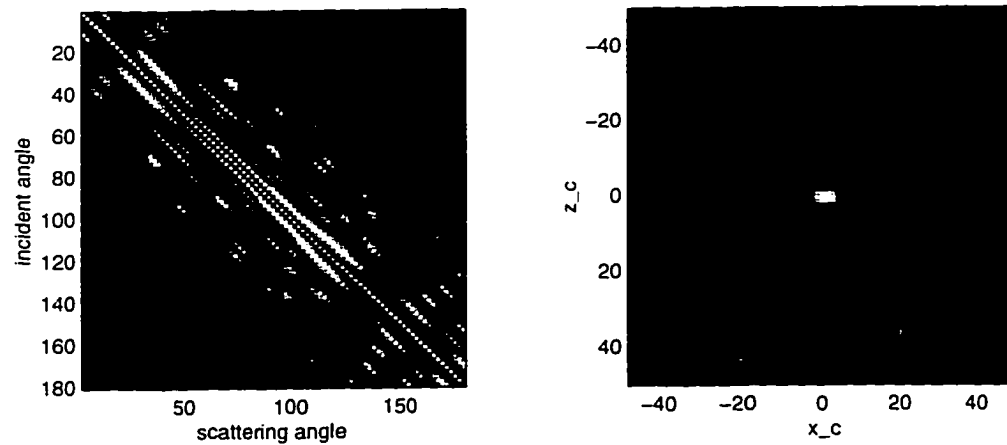

Figure 5.11: The inversion of medium correlation using Born approximation: the left panel is the wave field amplitude generated using the semi circular aperture; and the right panel the inverted correlation of the medium.

should pay particular attention to this distortion when interpreting the results with real data.

5.3.2   Case of the stacked data

For the surface seismic survey, especially 3D seismic survey in which large amount of data is involved, it is an advantage to work with stacked data, since the amount of data is reduced, as well as higher signal-to-noise ratio. This section shows how the stacking process is related to plane wave decomposition and the stacked wave field can be inverted using the diffraction tomographic technique.

Using the concept of exploding sources (Claerbout, 1995), a common midpoint (CMP) gather may be treated as an exploding source gather as shown in the top panel in figure 5.12. The stacking over a CMP gather can be written as

$$u_{cmp}(\mathbf{s}, t) = \int \int u(\mathbf{s}, \mathbf{r}, t - \tau(\mathbf{r})) d\mathbf{r},$$

where u_{cmp} is the stacked wavefield; $\mathbf{r}$ are the coordinates of the receiver on the surface; $\mathbf{s}$ is the coordinates of the middle point or exploding source; and $\tau(\mathbf{r})$ is the move out correction. Taking the temporal Fourier transform of the stacked wavefield u_{cmp}, one obtains

$$U_{cmp}(\mathbf{s}, \omega) = \int U(\mathbf{s}, \mathbf{r}, \omega) e^{i\omega\tau(\mathbf{r})} d\mathbf{r}.$$

where U is the Fourier transform of u. Notice that if $\omega\tau(r)$ is designated as $k_r(\mathbf{r}) \cdot \mathbf{r}$. the the stacked wavefield in frequency domain is equivalent to the plane waves with the wavenumber $\mathbf{k}_r(\mathbf{r})$.

$$U_{cmp}(\mathbf{s}, \omega) = U(\mathbf{s}, \mathbf{k}_r) = \int U(s, r, \omega) e^{i\mathbf{k}_r \cdot \mathbf{r}} d\mathbf{r}.$$

Similar to the crosswell diffraction tomographic technique, the Fourier transform is

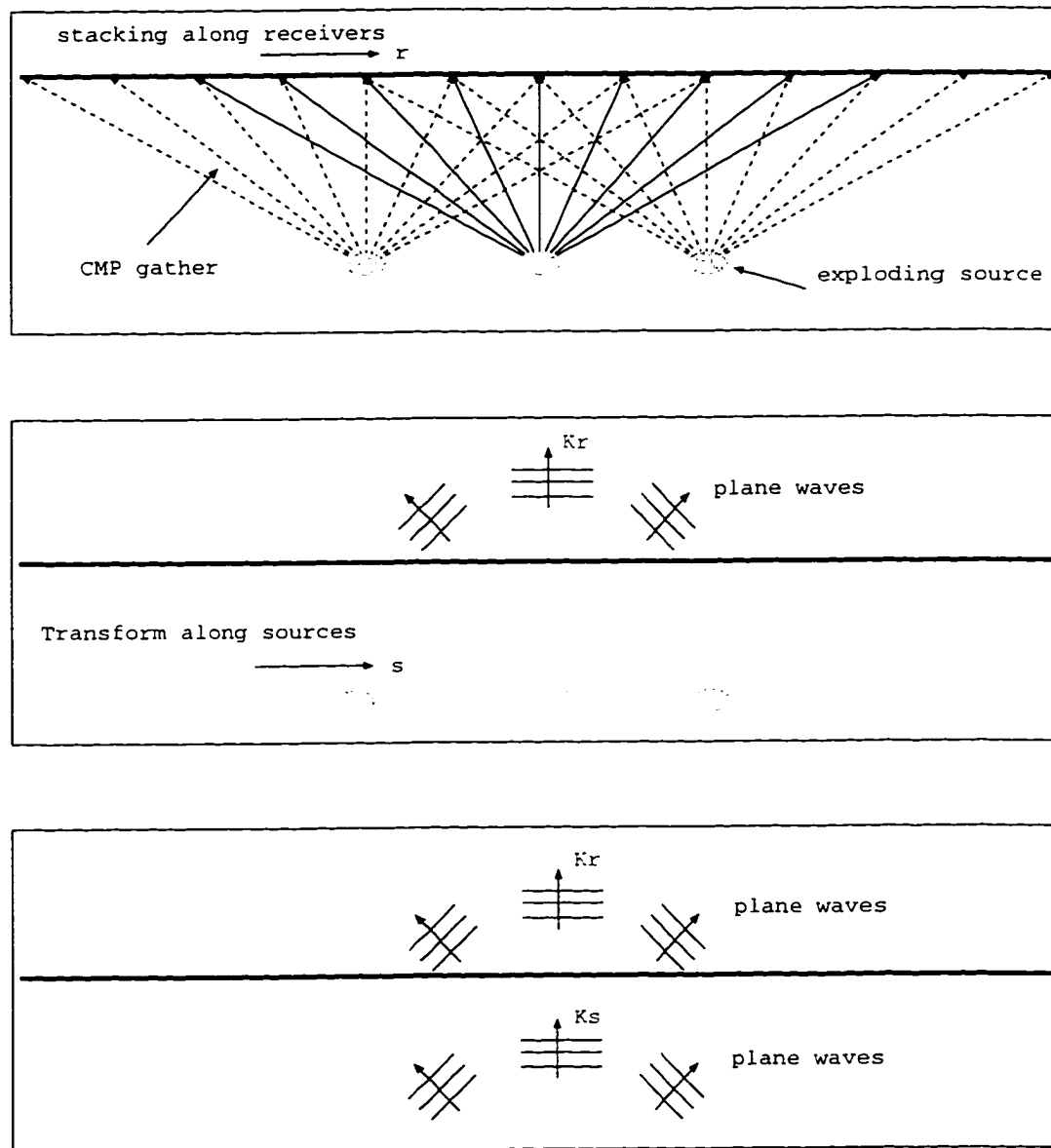Figure 5.12: The middle point (CMP) stacking geometry and exploding source gather: the top panel displays the middle point gathers and the stacking is equivalent to the plane wave decomposition; the middle panel shows that the exploding sources are synthesized as plane waves; and the bottom panel depicts the plane waves at receiver location and exploding source location in the fashion of the crosswell diffraction tomography.

taken along the exploding source to synthesize the plane waves,[5] i.e..

$$U(\mathbf{k}_s, \mathbf{k}_r) = \int U(\mathbf{s}, \mathbf{r}, \omega) e^{i(\mathbf{k}_r \cdot r + \bar{k} \cdot \mathbf{s})} d\mathbf{r} d\mathbf{s}.$$

The operation is shown in the middle panel of the figure 5.12. As in the case of crosswell diffraction tomographic inversion, the correlation function is obtained by inverting the spatial power spectrum of the wavefield.

The variation of k_r is provided using either the variation of the stacking velocity or the variation of the temporal frequency, or the combination of two. The spatial wavenumber coverage is shown in figure 5.13 Using the model of the exploding source. the crosswell diffraction tomography is used to invert the stacked data. The procedure is outline in figure 5.14

In the following example, a stacked profile of 3-D surface seismic surveys from west Texas is inverted. Figure 5.15 is the stacked profile and figure 5.16 is the inverted velocity profile.

---

[5] For an incoming plane wave, the outgoing spherical wave, under the far field approximation. the total field $\phi(\mathbf{x}, \mathbf{k})$ can be expressed as

$$\phi(\mathbf{x}, \mathbf{k}) = exp(i\mathbf{k} \cdot \mathbf{x}) - \frac{e^{i|\mathbf{k}||\mathbf{x}|}}{4\pi|\mathbf{x}|} T(\mathbf{k}', \mathbf{k})$$

where $\mathbf{k}$ and $\mathbf{k}' = |\mathbf{k}|\mathbf{x}/|x|$ are the incident and scattering wave vector respectively; and

$$T(\mathbf{k}', \mathbf{k}) = \int m(\mathbf{x}')e^{-i\mathbf{k}' \cdot \mathbf{x}'} \phi(\mathbf{x}', \mathbf{k})d\mathbf{x}'.$$

Applying the Born approximation, $\phi(\mathbf{x}', \mathbf{k}) = exp(i\mathbf{k} \cdot \mathbf{x}')$,

$$T(\mathbf{k}', \mathbf{k}) = \int m(\mathbf{x}')e^{i(\mathbf{k}-\mathbf{k}')\mathbf{x}'} d\mathbf{x}' = M(\mathbf{k} - \mathbf{k}')$$

where M is the Fourier transform of $\mathbf{m}$.
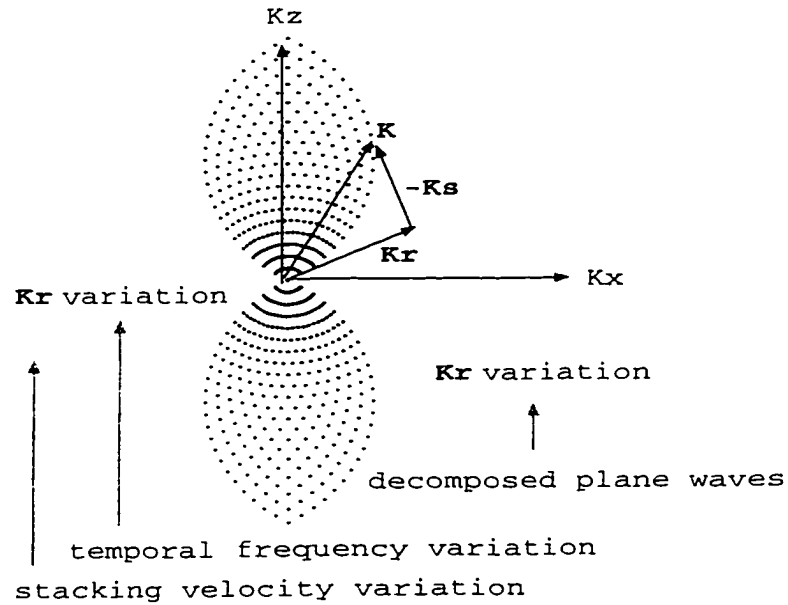
Figure 5.13: The spatial wavenumber coverage of the middle point gathers: the variation of the wavenumber k_r is provided using the variation of the variation of the temporal frequency. The coverage is in the fashion of the crosswell diffraction tomography.
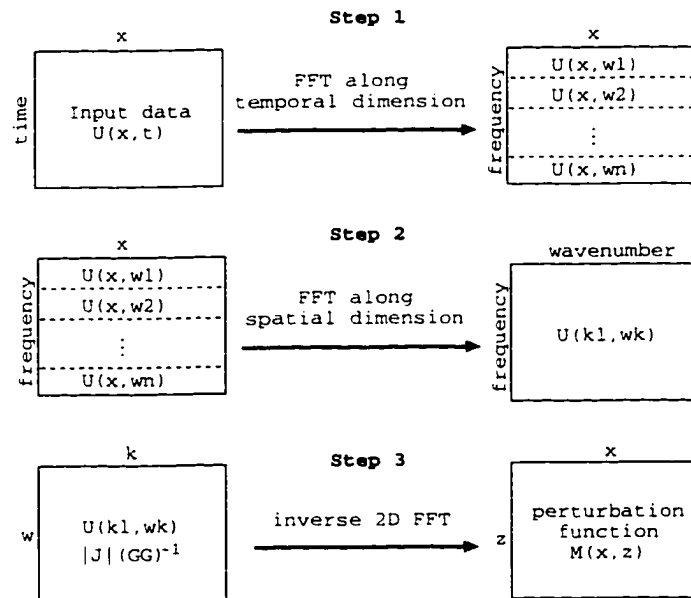
Figure 5.14: The flow chart of stacked data inversion.
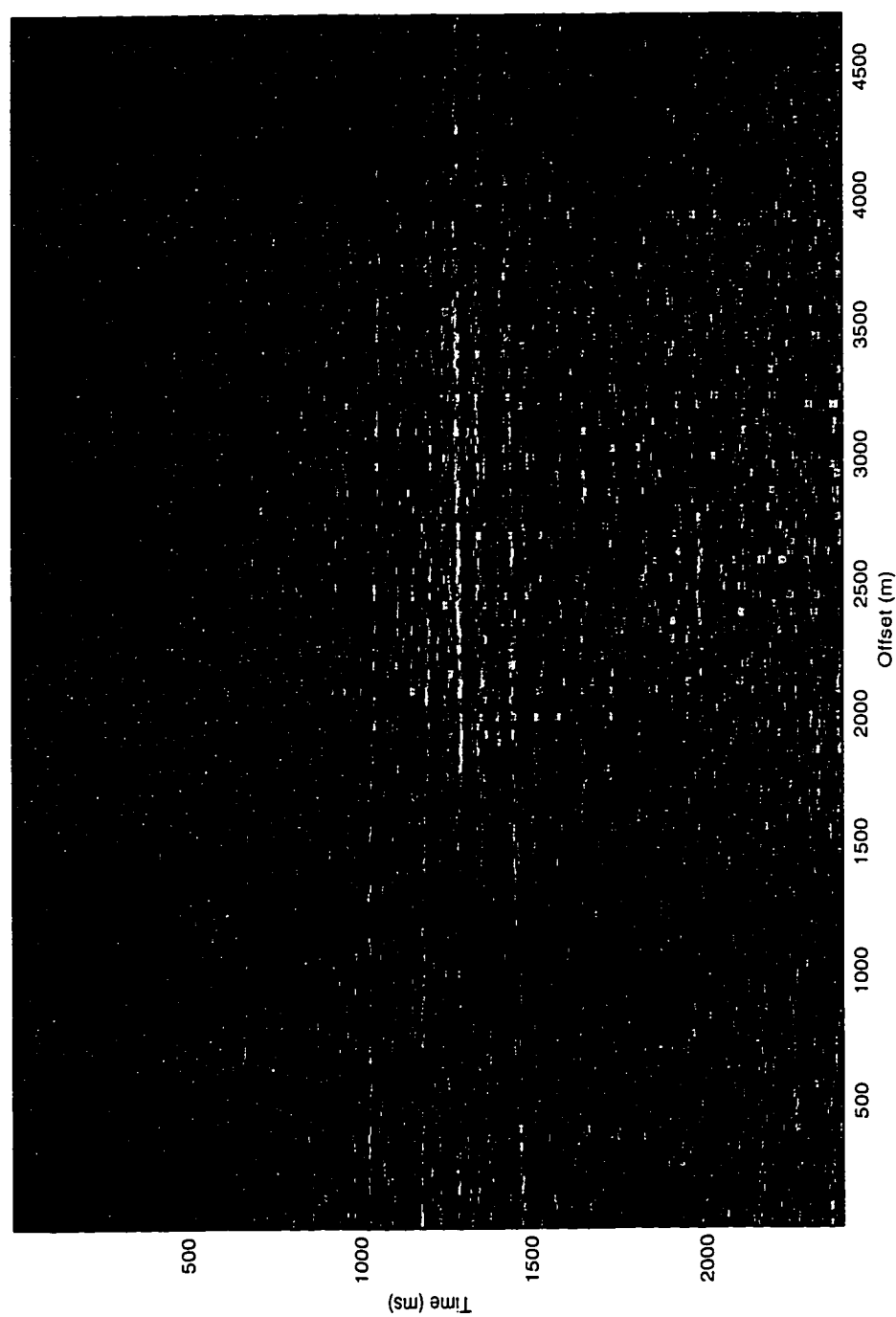
Figure 5.15: A profile of 3-D surface seismic survey from west Texas.
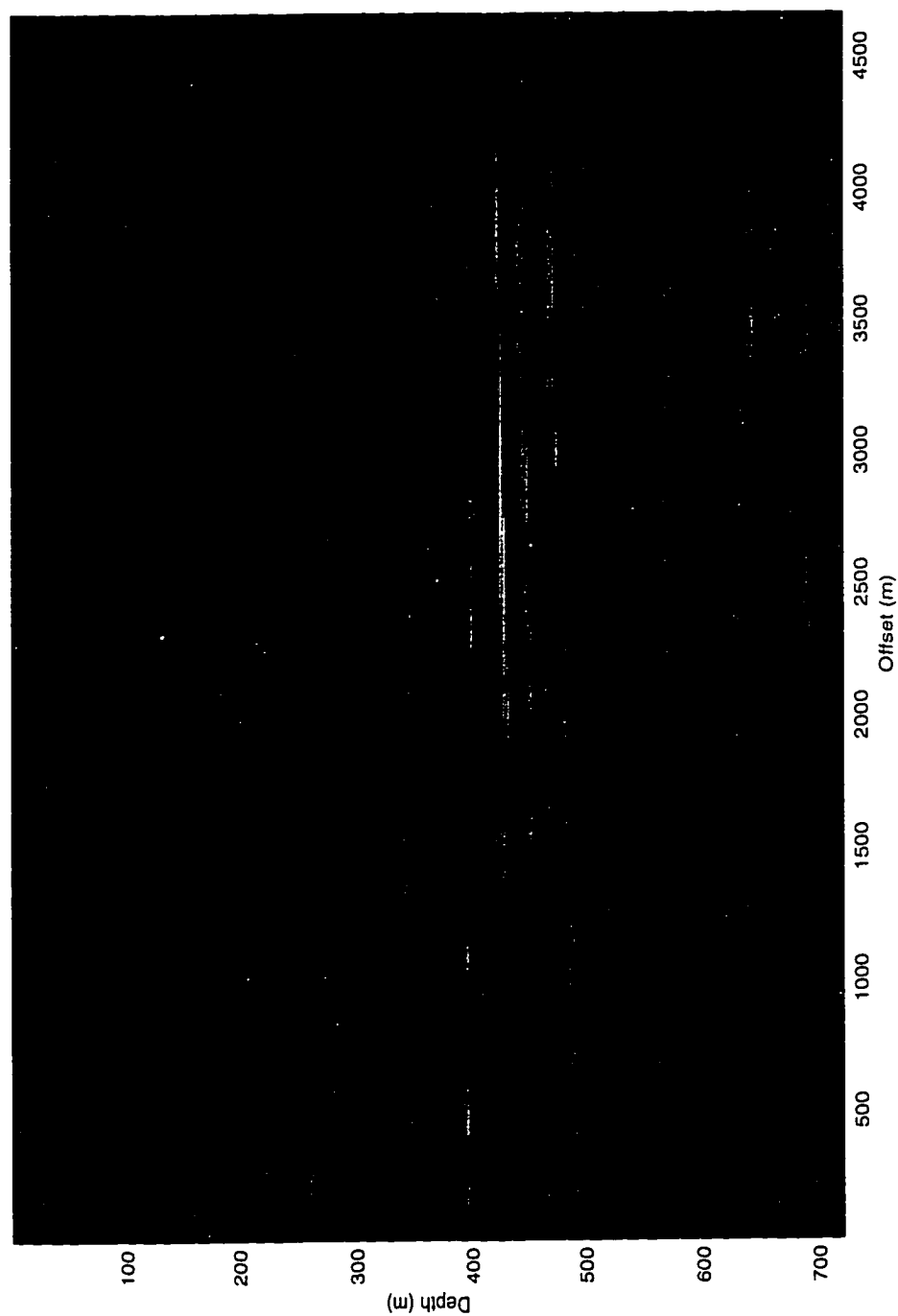
Figure 5.16: The inversion of the stacked surface seismic profile from west Texas.

The correlation of the inverted velocity inhomogeneity is shown in figure 5.17. One can see that the degree of the horizontal correlation is much higher than that of vertical and the orientation of the correlation is slightly tilted. These reflect the nature of weak horizontal variation and modestly dip in the zero offset time section and inversion. Notice the multiple scales of the inhomogeneity are also reflected in the vertical variation of the correlation.
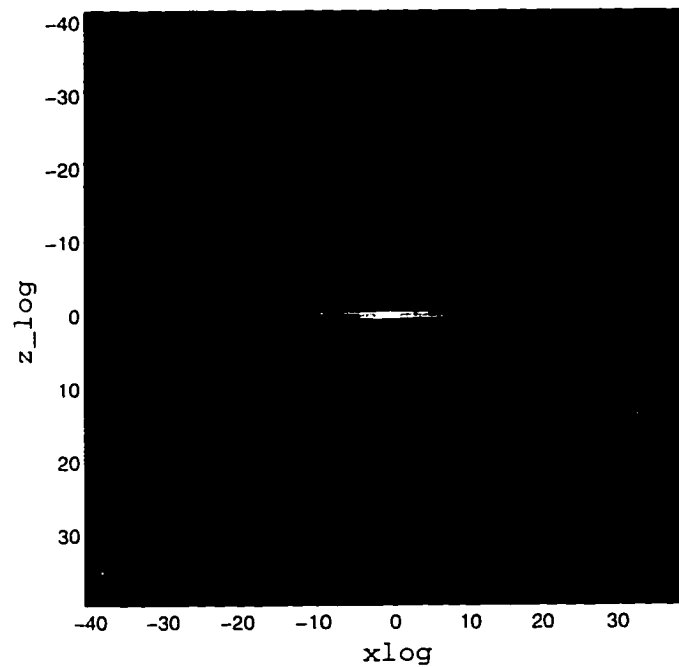
Figure 5.17: The inverted correlation function of surface seismic data: the vertical variations reflect the multi-scales of the inhomogeneity in vertical direction.

5.3.3   Case of the inhomogeneous background

If there is a trend or large scale variations in the medium, then the mean or background is no longer constant. As a result, the strength and scale of the inhomogeneity can be strong and large. The Born approximation is broken down and and the covariance is no longer the appropriate to model the spatial correlation structure anyway. Unfortunately, this happens very often in practice. To overcome the difficulties due to strong scattering, we apply the asymptotic technique as discussed in Chapter 5, and decompose the variation of the inhomogeneity into large scale and small scale components, as figure 5.18 indicates. Assuming that the large scale variation is known,
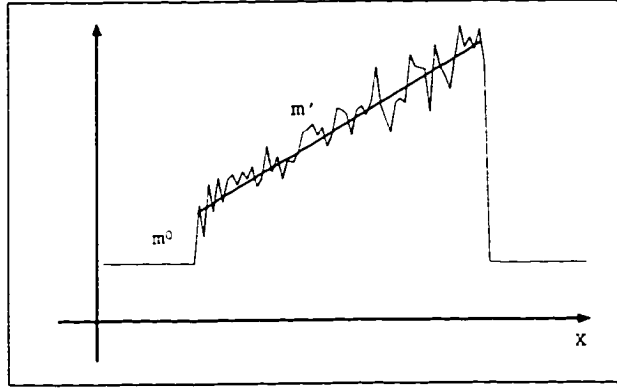

Figure 5.18: Illustration of the decomposed slowness profile with the prior knowledge m_0 and additional variations m'. m_0 may or may not be a homogeneous reference background.

we treat the smaller scale inhomogeneity as random perturbations to the variable background. In this section, we consider the influence of variable background upon the second moment of the wave field, and the asymptotic inversion of the correlation function.

The scattered field U, see the Chapter 2, can be written as

$$U(\mathbf{s}, \mathbf{r}) \sim - \int_V m(\mathbf{x}) A(\mathbf{x}, \mathbf{s}, \mathbf{r}) e^{i\phi(\mathbf{x}, \mathbf{s}, \mathbf{r})} d\mathbf{x}, \qquad (5.8)$$

where $A(\mathbf{x}, \mathbf{s}, \mathbf{r})$ and $\phi(\mathbf{x}, \mathbf{s}, \mathbf{r})$ are the amplitude and phase of the background field. Taking the Fourier transform along the source and receiver arrays and utilizing the

asymptotic Fourier transform outlined in Appendix C. one obtains

$$U(\mathbf{k}_s, \mathbf{k}_r) \sim \int_V m(\mathbf{x}) A(\mathbf{x}, \mathbf{k}_s, \mathbf{k}_r) e^{i\phi(\mathbf{x}, \mathbf{k}_s, \mathbf{k}_r)} d\mathbf{x}.$$

The second moment of $U(\mathbf{k}_s, \mathbf{k}_r)$ can be written as:

$$|U(\mathbf{k}_s, \mathbf{k}_r)|^2 \sim \int_V \int_V m(\mathbf{x}) m(\mathbf{y}) A(\mathbf{x}, \mathbf{k}_s, \mathbf{k}_r) A(\mathbf{y}, \mathbf{k}_s, \mathbf{k}_r) e^{i(\phi(\mathbf{x}, \mathbf{k}_s, \mathbf{k}_r) - \phi(\mathbf{y}, \mathbf{k}_s, \mathbf{k}_r))} d\mathbf{x} d\mathbf{y}.$$

Expand the phase function $\phi(\mathbf{x}, \mathbf{k}_s, \mathbf{k}_r)$ in the vicinity of $\mathbf{y}$. i.e.,

$$\phi(\mathbf{x}, \mathbf{k}_s, \mathbf{k}_r) - \phi(\mathbf{y}, \mathbf{k}_s, \mathbf{k}_r) = \phi_{,j}(\mathbf{y}, \mathbf{k}_s, \mathbf{k}_r)(x_j - y_j).$$

Letting $\xi_j = x_j - y_j$ be relative coordinates, expanding the amplitude and wavenumber $\phi_{,j}$ at ξ, and considering only the leading term. i.e.

$$A(\mathbf{x}) \sim A(\xi), \quad A(\mathbf{y}) \sim A(\xi), \quad \phi_{,j}(\mathbf{y}, \mathbf{k}_s, \mathbf{k}_r) \sim \phi_{,j}(\xi, \mathbf{k}_s, \mathbf{k}_r).$$

one obtains an expression of the power spectrum of the wavefield,

$$|U(\mathbf{k}_s, \mathbf{k}_r)|^2 \sim \int_V R(\xi) |A(\xi, \mathbf{k}_s, \mathbf{k}_r)|^2 e^{ik_j \xi_j} d\xi, \tag{5.9}$$

where $R(\xi) = \int m(\mathbf{y} + \xi) m(\mathbf{y}) d\mathbf{y}$ is the correlation function and depends only on the relative coordinates, and $k_j = \phi_{,j}(\xi, \mathbf{k}_s, \mathbf{k}_r)$. The approximation is justified because a smooth variable background is assumed.

Utilizing the results of Chapter 5, we can invert the correlation function $R(\xi)$. i.e..

$$R(\xi) \sim \int_{\Omega_k} |U(\mathbf{k}_s, \mathbf{k}_r)|^2 \frac{e^{-ik_j \xi_j}}{|A(\xi, \mathbf{k}_s, \mathbf{k}_r)|^2} |J(\mathbf{k}; \mathbf{k}_s, \mathbf{k}_r)| d\mathbf{k}_s d\mathbf{k}_r, \tag{5.10}$$

where Ω_k is the support of $\mathbf{k}_s$, and $\mathbf{k}_r$.

We demonstrated the technique discussed above with the field data from the McElroy far offset data set in figure 5.19 which shows the reconstruction of the perturbation function $m(\mathbf{x})$ using the asymptotic inversion without any data processing.

Even though some desired features seems to be clear in the tomogram, the distortion and noise are significant, because of data quality, many types of conversions, limited aperture, and etc. It is difficult to interpret the tomogram with this distortion and noise. The correlation of the perturbation function, on the other hand, may be useful in certain circumstance, since the incoherent noise and signals play less role when we perform inversion using the power spectrum instead of wave field itself. The right panel in figure 5.19 shows the inverted correlation function of the perturbation function. One can see that the orientation tilted slightly orientation towards to north-east which is consistent with the results from other techniques such as reflection mapping (TomSeis internal report, 1996).
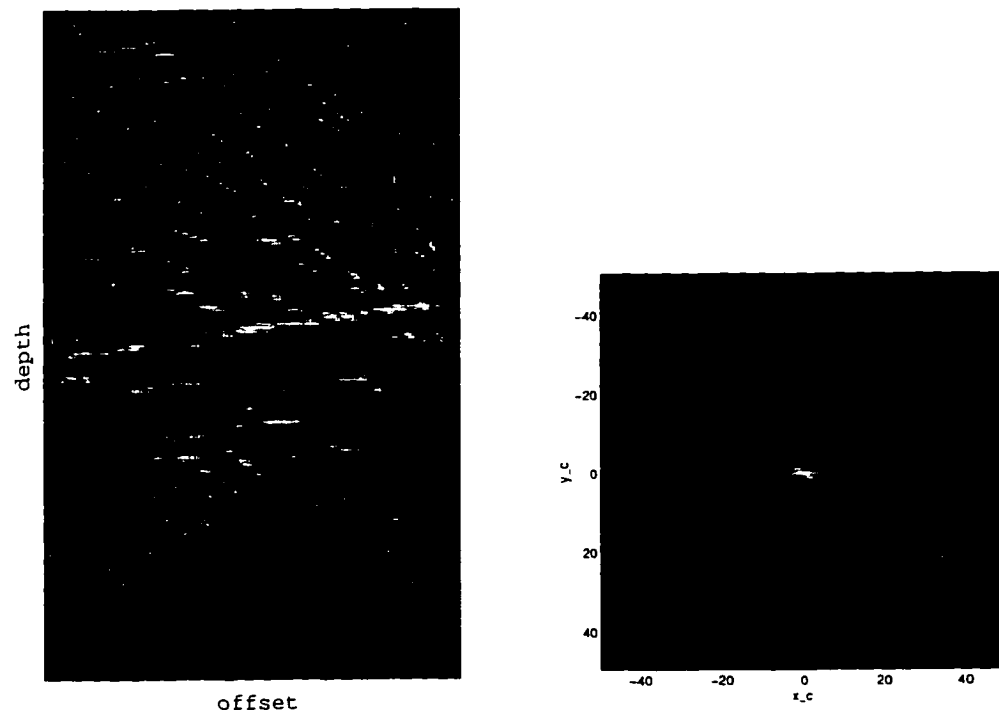

Figure 5.19: McElroy Far offset inversion: the left panel is the diffraction tomogram of velocity inhomogeneity recovered from the data set without any processing; the right panel is the inverted correlation function. the correlation length unit is $5ft$.

5.3.4 Case of the random elastic media

In this section we consider elastic random media. The elastic scattered field U_{l}, under the Born approximation can be written as the summation of the scattered fields from p-p, p-s, s-p, and s-s scattering (Beylkin and Burridge, 1987), i.e.,

$$U_{jk} = U_{jk}^{pp} + U_{jk}^{ps} + U_{jk}^{sp} + U_{jk}^{ss},$$

where

$$U_{jk}^{pp} \sim \int_V \omega^2 \rho^0 \left\{ \frac{\lambda'}{\lambda^0 + 2\mu^0} + \frac{\rho'}{\rho^0} \cos\theta^{pp} + \frac{2\mu'}{\lambda^0 + 2\mu^0} \cos^2\theta^{pp} \right\} \tilde{A}_j^p \hat{A}_k^p e^{i\Phi^{pp}} d\mathbf{x}.$$

$$U_{jk}^{ps} \sim \int_V \omega^2 \rho^0 \left\{ \frac{\rho'}{\rho^0} \cos\theta^{ps} + \frac{c_s \mu'}{c_p \mu^0} \sin 2\theta^{ps} \right\} \tilde{A}_j^p \hat{A}_{kl}^p \hat{\beta}_l^{ps} e^{-i\Phi^{ps}} d\mathbf{x},$$

$$U_{jk}^{sp} \sim -\int_V \omega^2 \rho^0 \left\{ \frac{\rho'}{\rho^0} \cos\theta^{sp} + \frac{c_s \mu'}{c_p \mu^0} \sin 2\theta^{sp} \right\} \tilde{A}_{jp}^p \tilde{\beta}_p^{sp} \hat{A}_k^p e^{i\Phi^{sp}} d\mathbf{x}.$$

$$U_{jk}^{ssH} \sim \int_V \omega^2 \rho^0 \left\{ \frac{\rho'}{\rho^0} \cos\theta^{ss} + \frac{\mu'}{\mu^0} \cos 2\theta^{ss} \right\} \tilde{A}_{jp}^s \tilde{\beta}_p^{ss} \hat{A}_{kl}^s \hat{\beta}_l^{ss} e^{-i\Phi^{ss}} d\mathbf{x}.$$

and

$$U_{jk}^{ssV} \sim \int_V \omega^2 \rho^0 \left\{ \frac{\rho'}{\rho^0} + \frac{\mu'}{\mu^0} \cos\theta^{ss} \right\} \tilde{A}_{jp}^s \tilde{\gamma}_p^{ss} \hat{A}_{kl}^s \hat{\gamma}_l^{ss} e^{-i\Phi^{ss}} d\mathbf{x},$$

given that the ϕ is the total phase from source to image point to receive, e.g., and $\Phi^{pp} = \tilde{\phi}(\mathbf{x}, \mathbf{s})^{pp} + \hat{\phi}(\mathbf{r}, \mathbf{x})^{pp}$; ρ', λ' and μ' are the density and elastic constants perturbations against the background ρ^0, λ^0 and μ^0 respectively. Notice θ^{pp}, θ^{ps}, θ^{sp}. and θ^{ss} are polarization angles. for example,

$$cos\theta^{pp} = \tilde{\alpha}_j^p \hat{\alpha}_j^p, \quad cos\theta^{ps} = \tilde{\alpha}_j^p \hat{\alpha}_j^s, \quad cos\theta^{sp} = \tilde{\alpha}_j^s \hat{\alpha}_j^p, \quad cos\theta^{ss} = \tilde{\alpha}_j^s \hat{\alpha}_j^s.$$

where

$$\tilde{\alpha}_j^p = \tilde{\phi}_{,j}^p, \quad \tilde{\alpha}_j^s = \tilde{\phi}_{,j}^s, \quad \hat{\alpha}_j^p = \hat{\phi}_{,j}^p, \quad \hat{\alpha}_j^s = \hat{\phi}_{,j}^s,$$

γ^{ps} is in the direction of $\bar{\alpha}^p \times \hat{\alpha}^s$, and β^{ps} is orthogonal to both $\hat{\alpha}^s$ and γ^{ps}. We can denote any of the above scattered fields in a general form (see Chapter 5):

$$U_{jk}(\mathbf{r}, \mathbf{s}) \sim \int \sum_{l=1,2,3} m_l(\mathbf{x}) w_l(\cos\theta(\mathbf{x}, \mathbf{r}, \mathbf{s})) A_{jk}(\mathbf{x}, \mathbf{r}, \mathbf{s}) e^{i\phi(\mathbf{x}, \mathbf{r}, \mathbf{s})} d\mathbf{x}. \qquad (5.11)$$

In the case of the p-p scattering, $U_{jk}(\mathbf{r}, \mathbf{s}) = U_{jk}^{pp}(\mathbf{r}, \mathbf{s})$, $A_{jk} = \bar{A}_j^p \hat{A}_k^p$, and $\tau(\mathbf{x}, \mathbf{r}, \mathbf{s}) = \tau^{pp}(\mathbf{x}, \mathbf{r}, \mathbf{s})$, and the perturbation function and polarization factor are:

$$m_l(\mathbf{x}) \subset \{ \frac{\lambda'}{\lambda^0 + 2\mu^0}, \frac{\rho'}{\rho^0}, \frac{2\mu'}{\lambda^0 + 2\mu^0} \}, \quad w_l(\cos\theta) \subset \{ 1, \cos\theta, \cos^2\theta \}.$$

As in the case of scalar waves, we take the Fourier transform of U_{jk} along the source and receiver, i.e.,

$$U_{jk}(\mathbf{k}_s, \mathbf{k}_r) \sim \int \sum_{l=1,2,3} m_l(\mathbf{x}) w_l(\cos\theta(\mathbf{x}, \mathbf{k}_s, \mathbf{k}_r)) A_{jk}(\mathbf{x}, \mathbf{k}_s, \mathbf{k}_r) e^{i\phi(\mathbf{x}, \mathbf{k}_s, \mathbf{k}_r)} d\mathbf{x}. \qquad (5.12)$$

The power spectrum of the scattered field becomes

$$|U_{jk}(\mathbf{k}_s, \mathbf{k}_r)|^2 \sim \int_V \sum_n R_n(\mathbf{x}) W_n(\cos\theta) |A_{jk}(\xi, \mathbf{k}_s, \mathbf{k}_r)|^2 e^{ik_j \xi_j} d\xi,$$

where the correlation function R_n and polarization factor W_n are defined as

$$R_n(\xi) \subset \{ n_{11}, n_{22}, n_{33}, n_{12}, n_{13}, n_{23} \}$$

and

$$W_n(\xi) \subset \{ w_{11}, w_{22}, w_{33}, w_{12}, w_{13}, w_{23} \}$$

with

$$n_{11} = <m_1(\mathbf{y}+\xi)m_1(\mathbf{y})>, \quad n_{22} = <m_2(\mathbf{y}+\xi)m_2(\mathbf{y})>.$$

$$n_{33} = <m_3(\mathbf{y}+\xi)m_3(\mathbf{y})>, \quad n_{12} = 2 <m_1(\mathbf{y}+\xi)m_2(\mathbf{y})>.$$

$$n_{13} = 2 <m_1(\mathbf{y}+\xi)m_3(\mathbf{y})>, \quad n_{23} = 2 <m_2(\mathbf{y}+\xi)m_3(\mathbf{y})> .$$

Notice that $n_{ij}(\xi)$ is the correlation of the elastic parameters which depends only on the relative coordinates ξ. Utilizing the results of Chapter 5, one can invert the correlation function of the elastic parameters as:

$$\sum_n R_n(\xi)W_nW_m \sim \int_\Omega \frac{W_m|U|^2}{|A_{jk}(\xi, \mathbf{k}_s, \mathbf{k}_r)|^2} e^{-\imath k_j \xi_j} |J(\mathbf{k}; \mathbf{k}_s, \mathbf{k}_r)| d\mathbf{k}_s d\mathbf{k}_r. \tag{5.13}$$

The individual correlation function can be solved from this system. The statistical properties of the medium are characterized by means of correlation function, of the elastic parameter R_n. In this study, we do not explore the physical meaning of the cross correlations between different elastic parameters. In the fracture characterization applications, we can assume that $\rho' = 0$ then $\sum_n R_n(\xi)W_n$ has only one term for s-s scattering, just like the case of the scalar wave.

Figure 5.20 shows the spatial distribution function, shared by μ', and λ'.[6] The

Figure 5.20: The correlation functions of the model. (a), (b), (c) and (d) corresponding to fractures are oriented in 0, 45, 90 and 135 degrees respectively.

---

[6]If the deviation of ρ', λ', and μ' from their average values is not small, the scattered field will be small only if the region in which these deviations occur is small. This is the situation of a thin layer scatterer which is considered as the elements of fractures.

horizontal and vertical autocorrelation lengths are 12.5 and $1.25m$ respectively. This model may corresponded to oriented fractured rock. The corresponding p-wave velocity is $3500m/s$, the s-wave velocity is $2121m/s$ and the density is $2.6g/cm^3$. The wave length for the p-wave is $10m$ and the crosswell near offset is $20~\lambda$.

Figure 5.21 shows the spectrum of the field calculated according to the Born approximation described above and one can see that the backscattered energy is stronger as the dip of the orientation increases.
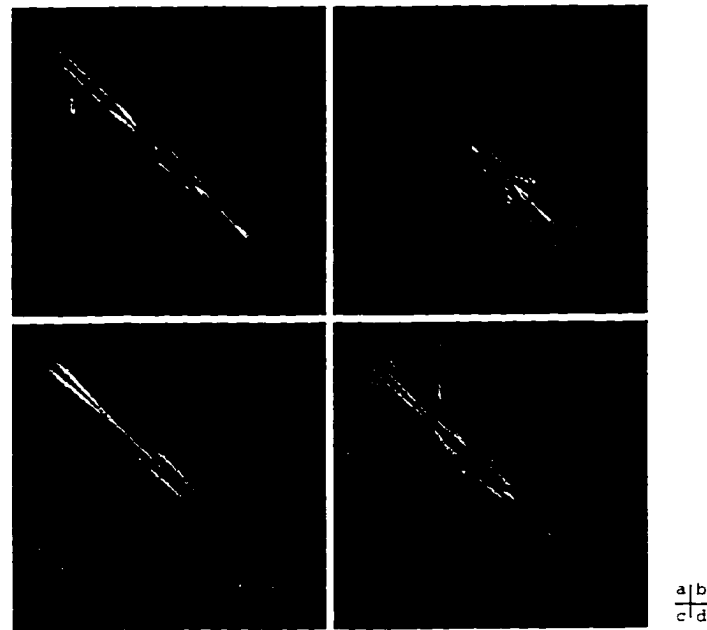
Figure 5.21: The spectra calculated using the Born approximation. The axis of each panel is source vs. receiver. As indicated, the stronger amplitude along the diagonal corresponding to in line scattering.

In Figure 5.22, we show the inverted correlation function of the medium. We can see that the retrieved correlation functions match the model well for 0°, 45°, and 135° orientations. At 90°, the retrieved correlation function is severe distorted compared to the original model. The reasons are that crosswell geometry has the poorer resolution in the horizontal direction due to a limited aperture is used for both generating data and inversion.
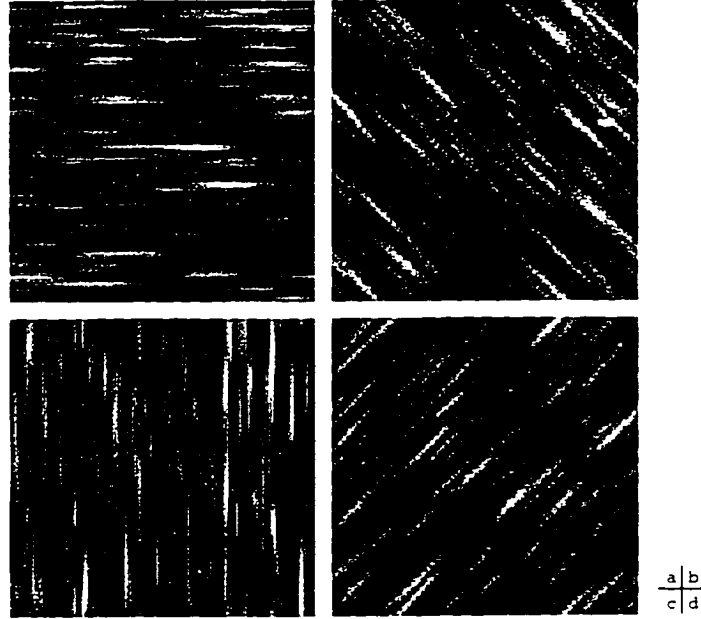
Figure 5.22: Inverted correlation functions from synthetic simulations: (a), (b), (c) and (d) corresponding to fractures are oriented in 0, 45, 90 and 135 degree respectively.
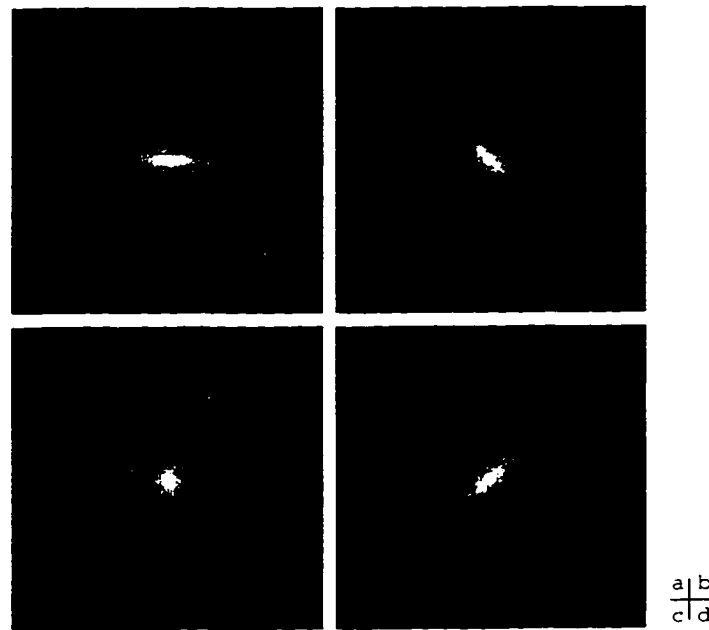
For the McElroy near offset data, the first S-arrival and earlier arrivals are eliminated and the amplitude is normalized to the zero offset. (Harris and Wang, 1996). From a receiver gather of the McElroy near offset data set which is shown in figure 5.23, one can see that there are many chaotic ss reflection/scattering features in the seismogram.

Figure 5.24 shows the temporal power spectra of the processed data set at two distinct frequencies. We average the above two power spectra and invert the correlation function using the technique discussed above. In figure 5.25 and figure 5.26, the inverted correlation and variogram are showed.

One can see that the correlation obtained is strongly "anisotropic", i.e., the horizontal and vertical correlation lengths are quite different. This is expected since the other studies suggest the geology structure at the McElroy set is basically one dimensional. Note that the correlation function recovered here is the 'raw' image, not of a particular elastic parameter but of the combination of the elastic parameters. Since we assume $\rho' = 0$, the correlation function is about the perturbation of the elastic
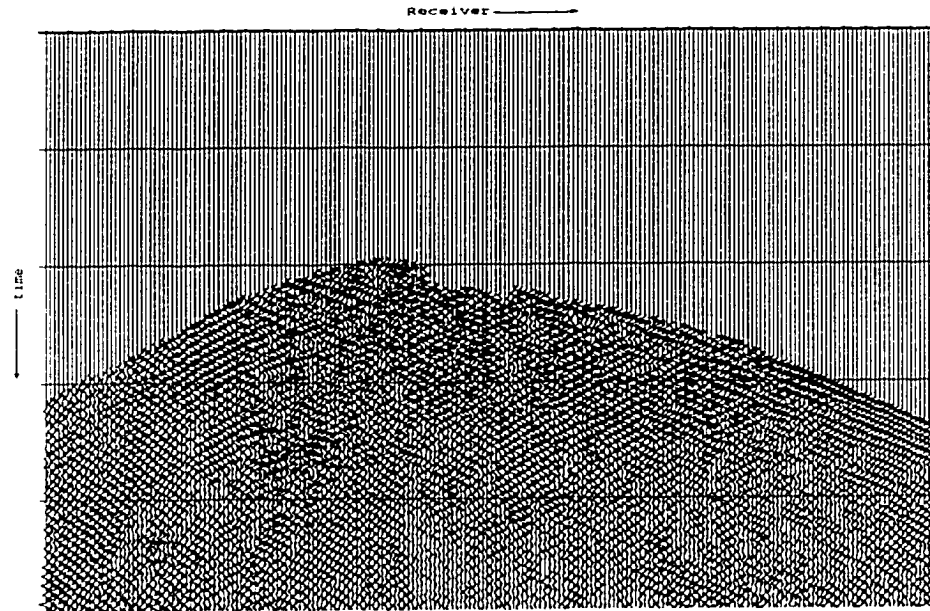
Figure 5.23: The wave field from McElroy near-offset data set. The first S-arrival and earlier arrival have been eliminated.
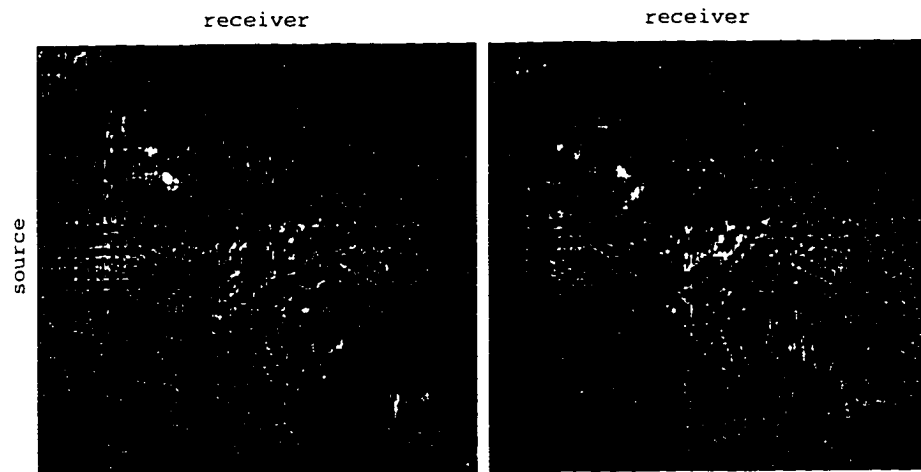
Figure 5.24: The power spectra of the wave field at two distinct frequencies: (a) and (b) are the spectrum at 1100 Hz and 1200 Hz, respectively.
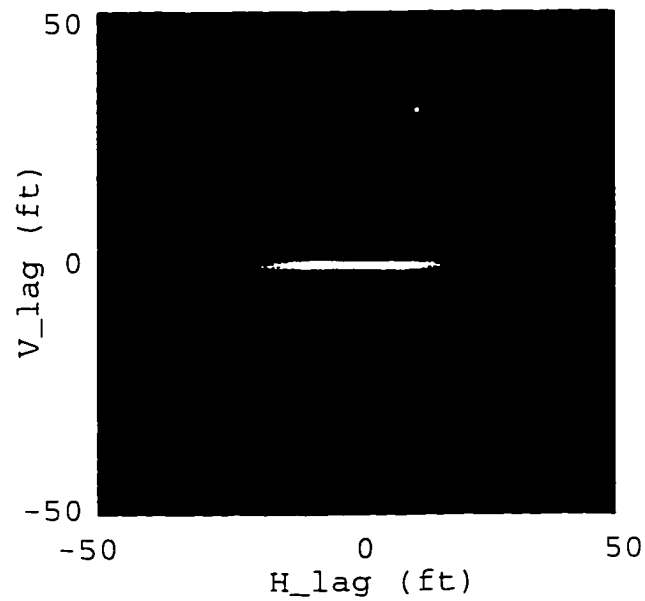
Figure 5.25: Inverted correlation functions from the McElroy near-offset McElroy near-offset data set: the image represents the inverted autocorrelation function of the shear modulus variation, assuming the density variation can be neglected.
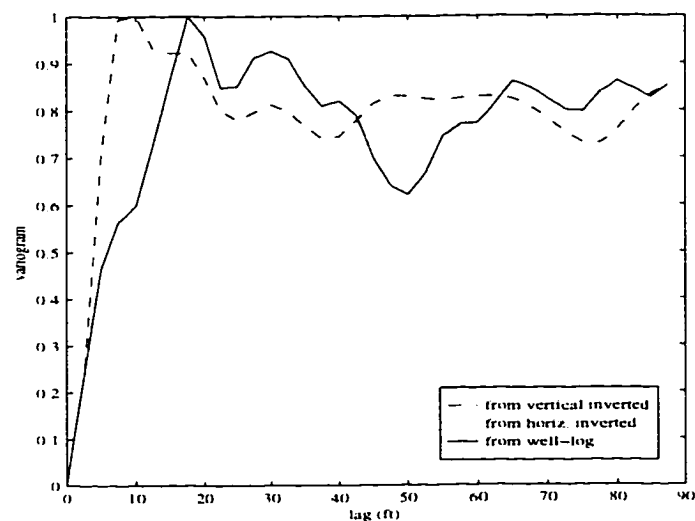
Figure 5.26: The variogram converted from the correlation of the well-log and from the inverted correlation functions.

constant μ'. In the figure 5.26, the correlation from the well-log and the inverted correlation function are converted into variograms. One can see that the multiple scale or "periodicity" of the inhomogeneity in the vertical direction.

5.4   Application to reservoir simulation

Deterministic interpolation techniques do not take into account a model of the spatial process. Advanced geostatistical techniques such as kriging and simulations allow you to quantify soft or qualitative information and to make predictions at unsampled locations. The variogram[7] (or its equivalent, the covariance) function is an essential tool for any geostatistical analysis. It is either assumed known or considered available through a sufficiently reliable estimate. The random medium inversion discussed above provides spatial correlation structures. One one applications to the inverted correlation structure is to construct the variogram or correlogram for geostatistical simulations.

There are a variety of advanced simulation techniques, in the following we show some realizations by using the sequential Gaussian simulation technique discussed in Deutsch and Journel (1992). The variogram parameters is derived from figure 5.26. The simulation is conditioned by well logs to reduce the probability range of the velocity distribution. Figure 5.27 shows six realizations. Figure 5.28 shows the averages of 10 realizations.

The potential of Diffraction tomography is not only for imaging inhomogeneity of a wavelength scale but also for estimating the statistical properties. The average of the velocity realizations in figure 5.28 shows higher resolution and the scale of the inhomogeneity is up to well-log scale. Notice that the simulations in figure 5.27 and figure 5.28 is used to illustrate the concept and the results here may not be optimal.

---

[7]The variogram is related to the covariance in the following manner:

$$\gamma(h) = covariance(0) - covariance(h)$$

where h is called the lag distance. Variogram can be can be derived from covariance and vice versa. provided that the covariance exist.

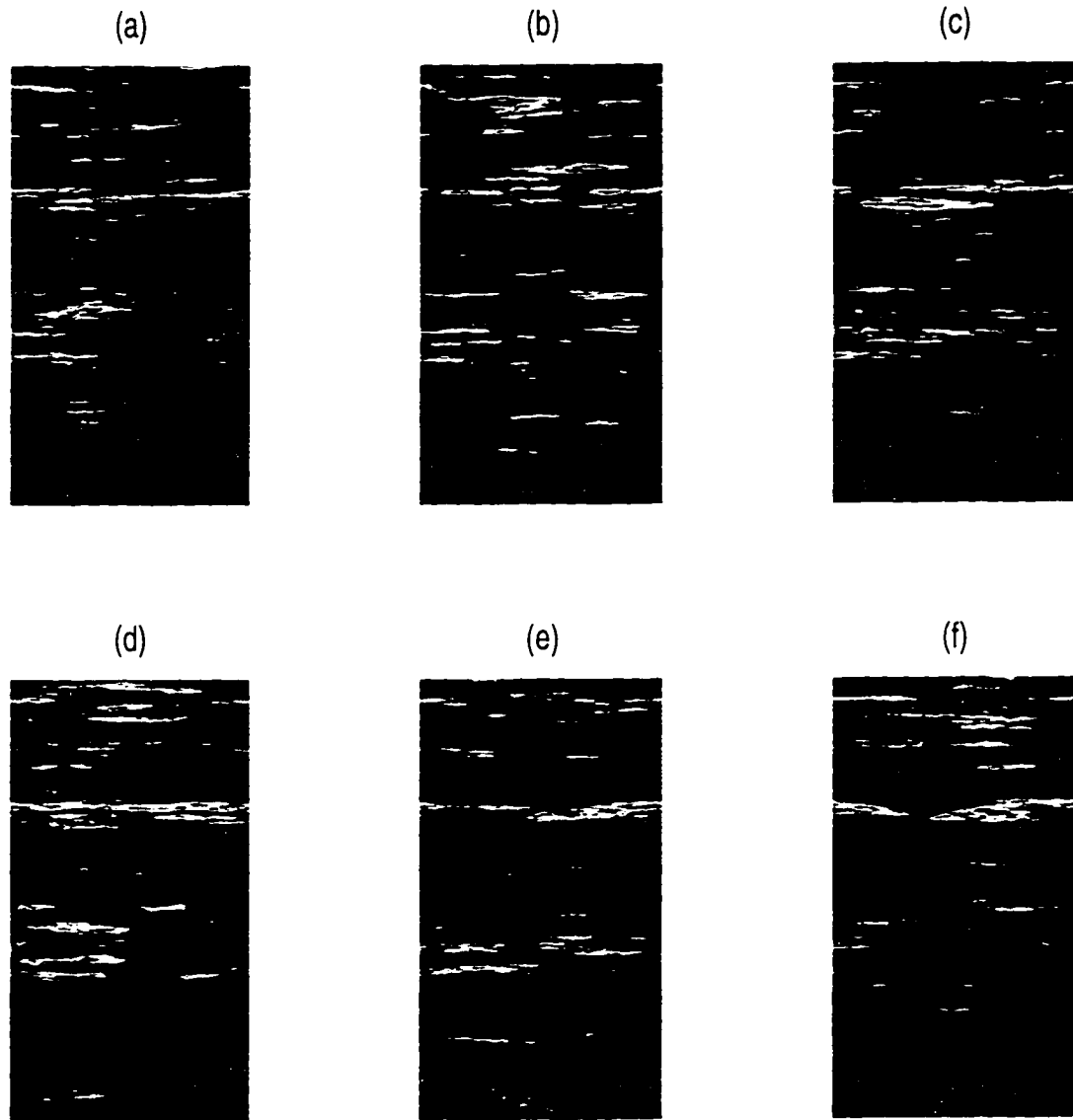Figure 5.27: Realization of sequential Gaussian simulation: the variogram parameters is derived from inverted correlation function from McElroy near offset data. The simulation is conditioned by well logs.
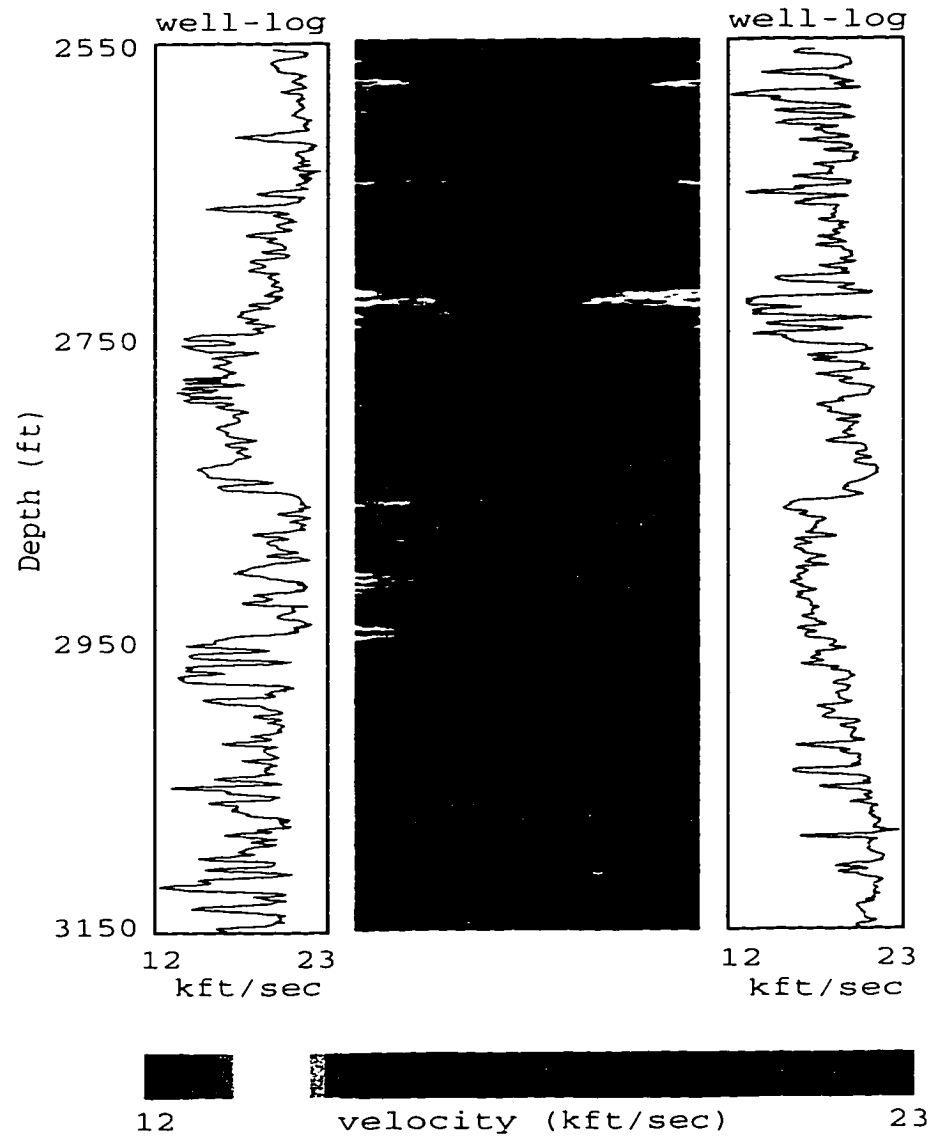
Figure 5.28: Average of 10 velocity realizations using the sequential Gaussian simulation in which the information about inhomogeneity is up to well-log scale. (a)-(f) are different realizations.

In practice, simulations are conditioned by more than one kind of information to narrow the probability distribution and this is beyond the scope of this thesis.

5.5 Conclusions

The methods of the random medium inversion discussed in this chapter complement the tomographic inversions discussed in previous chapters, when media and wavefield are highly irregular. The resolved statistical quantities, such as the auto-correlation and cross-correlation of the random medium, can be used directly to characterize the fracture scales as well as orientation, and reservoir simulations.

The random medium inversion is limited to the linear case, i.e., the Born approximation is used and only second-order statistics involved. It is possible to calculate higher-order statistics, especially when nonlinear terms of scattered fields have to be taken into consideration. A usefulness of the high order statistics is that the phase relations between frequency components are preserved which provide critical information for imaging.

Appendix A

Diffraction tomography

A.1 Born approximation

The reduced scalar wave equation is:

$$(\nabla^2 + k^2 n^2(\mathbf{r}))\psi(\mathbf{r}) = 0, \tag{A.1}$$

where $n(\mathbf{r})$ is the index of refraction, and $\psi(\mathbf{r})$ is the scalar wave field. Let ϵ be a small number and $n^2(\mathbf{r}) = n_0^2(\mathbf{r}) + \epsilon o(\mathbf{r})$, where $n_0(\mathbf{r})$ is the background refraction index, and $o(\mathbf{r})$ is a small perturbation to the background, then the equation (A.1) can be rearranged as

$$(\nabla^2 + k^2 n_0^2)\psi(\mathbf{r}) = -\epsilon k^2 o(\mathbf{r})\psi(\mathbf{r}). \tag{A.2}$$

The solution to equation (A.2) can be expressed as an integral equation:

$$\psi(\mathbf{r}) = \psi_0(\mathbf{r}) - \epsilon k^2 \int dr' G(\mathbf{r}, \mathbf{r}') o(r')\psi(\mathbf{r}'). \tag{A.3}$$

where ψ_0 is the incident fields, and $G(\mathbf{r}, \mathbf{r}')$ is the Green's function which satisfies

$$(\nabla^2 + k^2 n_0^2)G(\mathbf{r}, \mathbf{r}') = -\delta(\mathbf{r} - \mathbf{r}'). \tag{A.4}$$

142

Let $\mathcal{T}(k)$ be the linear operator:

$$(\mathcal{T}f)(\mathbf{r}) = k^2 \int d\mathbf{r}' G(\mathbf{r} - \mathbf{r}')o(\mathbf{r}')f(\mathbf{r}'). \tag{A.5}$$

The integral equation (A.3) can be rewritten as

$$(\mathcal{I} - \epsilon\mathcal{T}(k))\psi(\mathbf{r}) = \psi_0(\mathbf{r}), \tag{A.6}$$

whose solution is given formally by

$$\psi(\mathbf{r}) = (\mathcal{I} - \epsilon\mathcal{T}(k))^{-1}\psi_0(\mathbf{r}). \tag{A.7}$$

If we define the normal $\epsilon\|\mathcal{T}(k)\| = \sup_f \frac{(\mathcal{T}f)(\mathbf{r})\|}{\|f(\mathbf{r})\|} < 1$, then $(\mathcal{I} - \epsilon\mathcal{T}(k))^{-1}$ can be expanded to

$$(\mathcal{I} - \mathcal{T}(k))^{-1} = \mathcal{I} + \sum_{n=1}^{\infty} \epsilon^n \mathcal{T}^n(k), \tag{A.8}$$

and therefore,

$$\psi(\mathbf{r}) = \sum_{n=0}^{\infty} \epsilon^n \psi_n(\mathbf{r}), \tag{A.9}$$

where $\psi_n(\mathbf{r}) = \mathcal{T}_n(k)\psi_0(\mathbf{r})$ are waves scattered n times. The expansion (A.9) can be truncated to get approximations to wave field ψ:

$$\psi_B^N(\mathbf{r}) = \sum_{n=0}^{N} \epsilon^n \psi_n(\mathbf{r}). \tag{A.10}$$

The first Born approximation is for $N = 1$ and the corresponding error is given by

$$E_B^N(\mathbf{r}) = \sum_{N+1}^{\infty} \epsilon^n \psi_n(\mathbf{r}) = \epsilon^{N+1}\mathcal{T}^{N+1}(k)\psi(\mathbf{r}).$$

or relatively

$$\frac{||E_B^N(\mathbf{r})||}{||\psi(\mathbf{r})||} \leq \epsilon^{N+1} ||\mathcal{T}(k)||^{N+1}. \tag{A.11}$$

For example, assuming a homogeneous background, $n_0(\mathbf{r}) = 1$. $\epsilon = 1$. and $|o(\mathbf{r})| \leq M$ for all $\mathbf{r}$, then

$$||\mathcal{T}(k)|| = \frac{1}{2} M k^2 D^2 = 2\pi^2 M (\frac{D}{\lambda})^2, \tag{A.12}$$

where D is the diameter of the scattering volume (Kelley, 1958). Thus. the Born series converges if $2\pi^2 M (D/\lambda)^2 < 1$. The relative error of the first Born approximation can be characterized by $M^2 (D/\lambda)^4$.

A.2 Rytov approximation

Born approximation creates a linear relation between the perturbation function and complex amplitude. The phase and amplitude is not separated. Rytov approximation creates a linear relation between the perturbation function and complex phase. in which the phase and amplitude is separated. This natural separation arrives from its relation to forward scattered energy: traveltime delays accumulate through a velocity perturbation. Let the total field be an exponential form, i.e..

$$\psi(\mathbf{r}) = e^{S(\mathbf{r})}. \tag{A.13}$$

where $S(\mathbf{r})$ is complex phase function. Let $S = S^i + S^{sc}$. where S^i and S^{sc} are complex phases associated with the incident field and scattered field, respectively. Substituting (A.13) into (A.2) one obtains

$$\nabla^2 (\psi_0 S^{sc}) + k_0^2 (\psi_0 S^{sc}) = -\psi_0 (k_0^2 n(\mathbf{r}) + |\nabla S^{sc}|^2). \tag{A.14}$$

The solution to (A.14) can be written as

$$\psi_0(\mathbf{r})S^{sc}(\mathbf{r}) = -\int \psi_0(\mathbf{r}')(k_0^2 n(\mathbf{r}') + |\nabla S^{sc}(\mathbf{r}')|^2)G(\mathbf{r}, \mathbf{r}')d\mathbf{r}'. \qquad (A.15)$$

The Rytov approximation says that

$$\psi_0(\mathbf{r})S^{sc}(\mathbf{r}) = -k_0^2 \int n(\mathbf{r}')\psi_0(\mathbf{r}')G(\mathbf{r}, \mathbf{r}')d\mathbf{r}'. \qquad (A.16)$$

A.3 Diffraction tomography of scalar waves

Using the first Born approximation $\psi = \psi_0 = G$, equation (A.3) can be approximated as

$$U(\mathbf{r}_s, r_g) = -k_0^2 \int o(\mathbf{r}')G(\mathbf{r}', \mathbf{r}_g)G(\mathbf{r}_g, \mathbf{r}')d\mathbf{r}'. \qquad (A.17)$$

where $U = \psi - \psi_0$, and $\mathbf{r}_s$ and $\mathbf{r}_g$ are the distances from the origin to the considered source and receiver respectively. The relation (A.17) is linear and can be reformulated as the Fourier transform. The object function $o(\mathbf{r}')$ can be reconstructed via the inverse Fourier transform.

A.3.1 Two-dimensional reconstruction

For two dimensional problems, the Green's function is the zero order Hankel function of the first kind, i.e.

$$G(\mathbf{r}, \mathbf{r}') = -\frac{i}{4}H_0^{(1)}(k_0\sqrt{|\mathbf{r} - \mathbf{r}'|}), \qquad (A.18)$$

where $|\mathbf{r} - \mathbf{r}'| = \sqrt{(x - x')^2 + (z - z')^2}$. Figure A.1 shows the observation system of the crosswell survey. Taking Fourier transform of (A.17) along the source array and receiver array with respect to z_s and z_g respectively of expression (A.17), as indicated
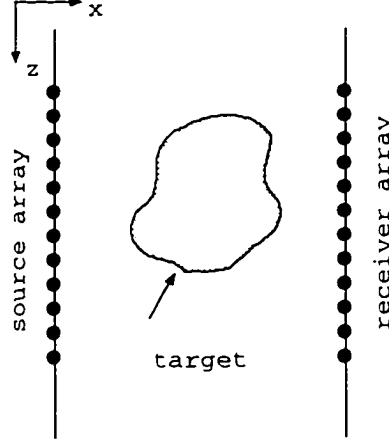
Figure A.1: 2-dimensional geometry of source and receiver arrays

in Figure A.1, one obtains (Harris, 1987, Wu, 1987):

$$U(x_s, k_{zs}, x_g, k_{zg}) = \frac{k_0^2}{4\gamma_s\gamma_g}e^{i\gamma_s x_s - i\gamma_g x_g}\int o(x, z)e^{-i(\gamma_s - \gamma_g)x - i(k_{zs} + k_{zg})z}dxdz. \qquad (A.19)$$

where k_{zs}, k_{zg} are the wave numbers along source array and receiver array: $\gamma_s = \sqrt{k_0^2 - k_{zs}^2}$ and $\gamma_g = \sqrt{k_0^2 - k_{zg}^2}$. If we let

$$k_x = \gamma_s - \gamma_g; k_z = k_s + k_g, \qquad (A.20)$$

the object function $o(x, z)$ can be reconstructed, i.e.,

$$o(x, z) = \int U(\mathbf{k}_s, k_g)\frac{4\gamma_s\gamma_g}{k_0^2}e^{-i\gamma_s x_s + i\gamma_g x_g}e^{-i(k_x x + k_z z)}J(k_x, k_z|k_s, k_g)dk_{zs}dk_{zg}. \qquad (A.21)$$

where $J(k_x, k_z|k_s, k_g)$ is the Jacobian transformation form k_x, k_z to k_s, k_g which depends on a specific geometry of source/receiver array.

In Figure A.2 - A.4 (Harris, 1993), we shown the wavenumber coverage of the crosswell, surface seismic and vertical seismic observation geometry, respectively. Figure A.5 shows an image of point targets at four locations, for a crosswell experiment with 128 source and receivers. The pixel spacing in the image is $\lambda/4$. The point target scattered data were generated by the method of moment. As expected, the resolution
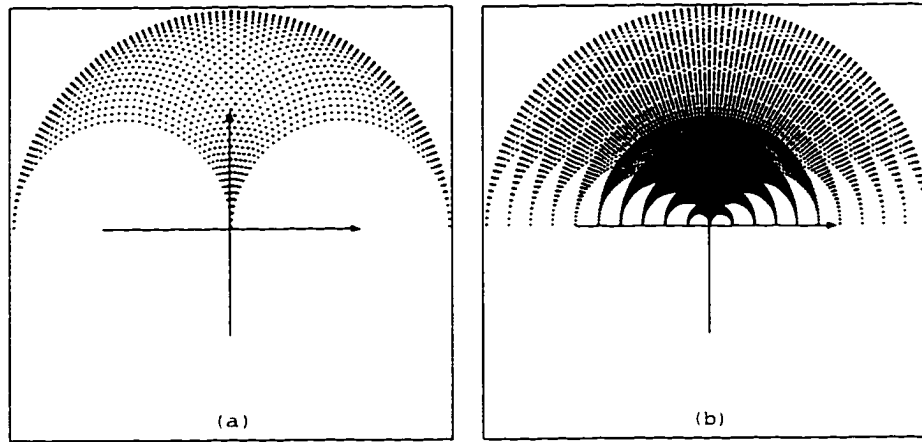
Figure A.2: Fourier coverage for surface seismic profiling: (a) is multi-view at a single frequency and (b) is multi-view and multi-frequency.
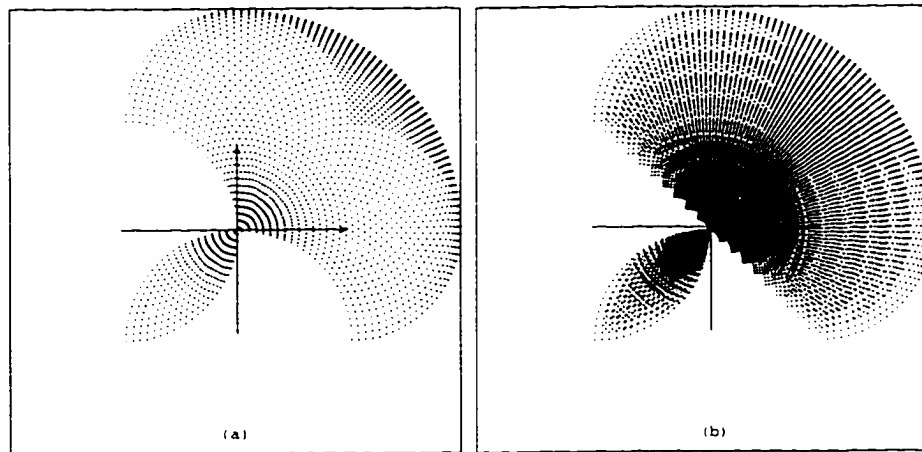
Figure A.3: Fourier coverage for vertical seismic profiling: (a) is multi-view at a single frequency and (b) is multi-view and multi-frequency.
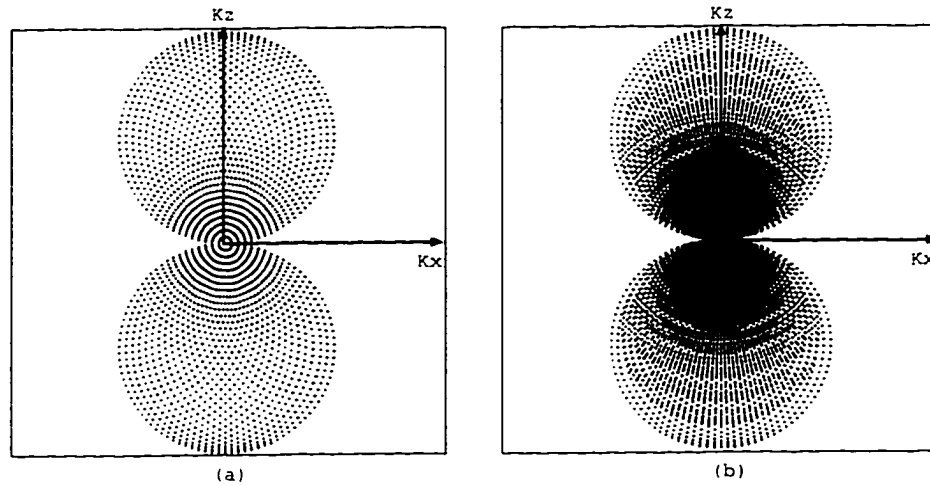
Figure A.4: Fourier coverage for crosswell seismic profiling: (a) is multi-view at a single frequency and (b) is multi-view and multi-frequency.

is significantly poorer in the horizontal direction because of poor coverage in K_r. In general, the resolution is approximately 1λ in x and 0.5λ in z, independent of target location.
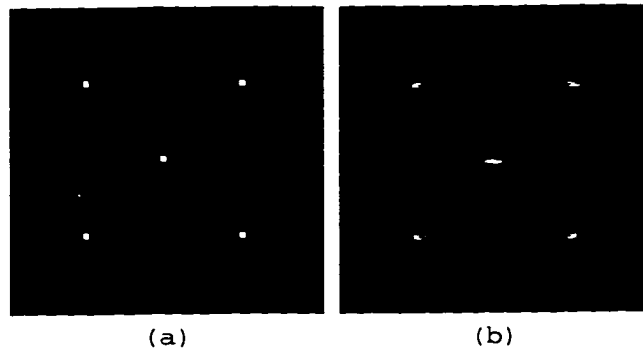
Figure A.5: Reconstruction using the Born approximation where the background velocity is 3500 m/s, velocity of diffractor is 5000 m/s, and temporal frequency is 500 Hz. (a) and (b) are the model and reconstruction from crosswell synthetic data, respectively.

A.3.2   Three-dimensional reconstruction

For three dimensional problems, the Green's function can be written as

$$G(\mathbf{r}, \mathbf{r'}) = -\frac{1}{4\pi} \frac{e^{-ik_0|\mathbf{r}-\mathbf{r'}|}}{|\mathbf{r} - \mathbf{r'}|}, \tag{A.22}$$

where $|\mathbf{r} - \mathbf{r'}| = \sqrt{(x - x')^2 + (y - y')^2 + (z - z')^2}$. Taking Fourier transform along the source array and receiver array of expression (A.17), with respect to z_s an z_g. respectively, one has

$$U(x_s, y_s, k_s, x_g, y_g, k_g) = \frac{-k_0^2}{16\pi} \int o(x, y, z) e^{-i(k_s+k_g)z} \tag{A.23}$$

$$H_0^{(1)}(\gamma_s R_s) H_0^{(1)}(\gamma_g R_g) dx dy dz.$$

where $R_s = \sqrt{(x - x_s)^2 + (y - y_s)^2}$ and $R_g = \sqrt{(x_g - x)^2 + (y_g - y)^2}$. By taking the Fourier transform of (A.24) along the source array and receiver array with respect to y_s and y_g one obtains (see figure A.6).

$$U(x_s, k_{ys}, k_{zs}, x_g, k_{yg}, k_{zg}) = \frac{-k_0^2(k_{ys}k_{yg} - k_{xs}k_{xg})}{16\pi k_{xs}k_{xg}} e^{-ik_{xg}x_g + ik_{xs}x_s} \tag{A.24}$$

$$\int o(x, y, z) e^{-i(k_{zs}+k_{zg})z - i(k_{ys}+k_{yg})y - i(k_{xs}-k_{xg})x} dx dy dz.$$

where $k_{xs} = \sqrt{\gamma_s^2 - k_{ys}^2}$ and $k_{xg} = \sqrt{\gamma_g^2 - k_{yg}^2}$. The objection function can be reconstructed via the inverse Fourier transform, as discussed in the two dimensional case described above.
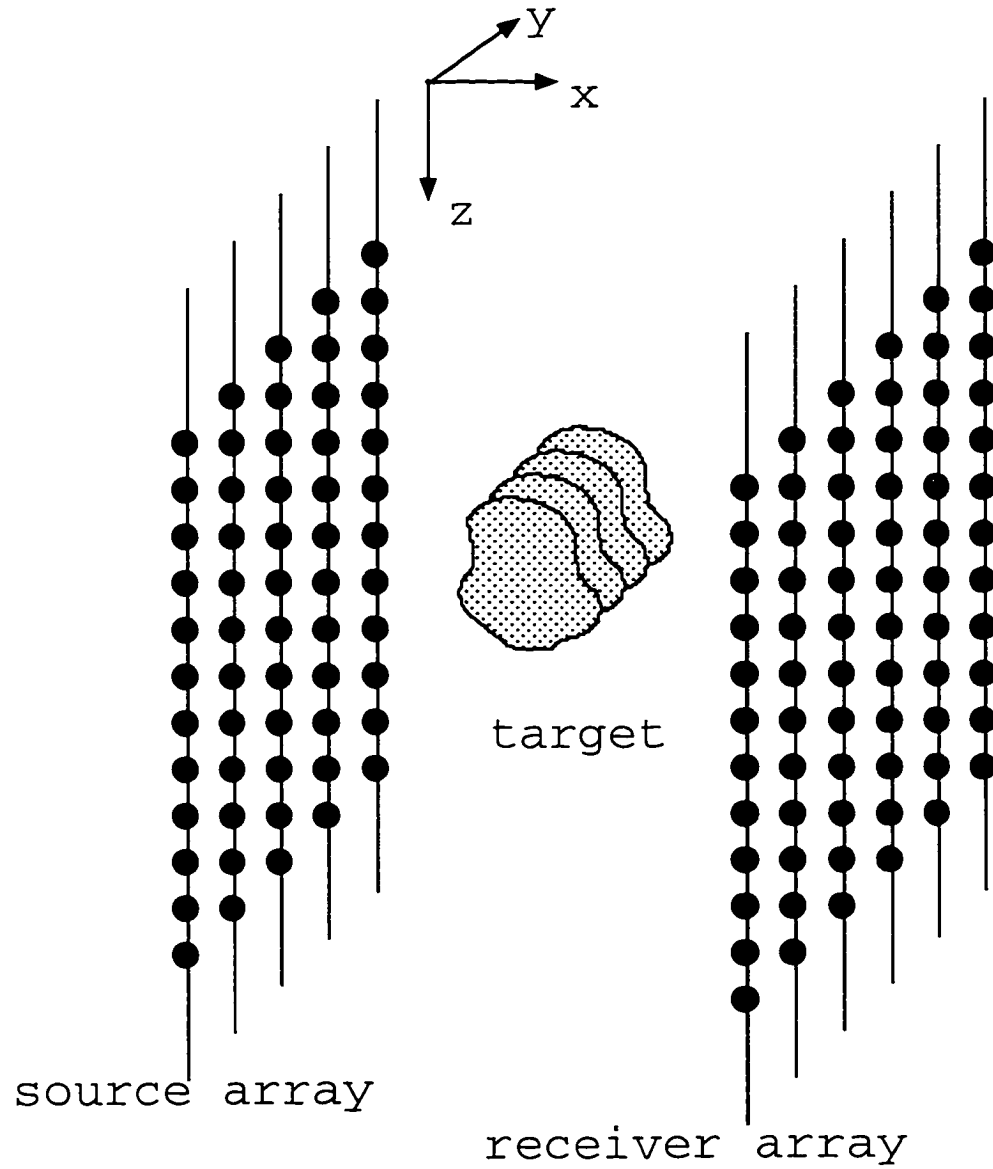
Figure A.6: 3-dimensional geometry of source and receiver arrays

Two dimensional tensor Green's function and its spectrum

To apply diffraction tomography with the Born approximation to elastic waves, one has to consider the tensor Green's function and its spectrum. Tensor Green's functions satisfy:

$$\omega^2 \rho G_{ij} - (\lambda + \mu)G_{kj,ki} - \mu G_{ij,kk} = \delta_{ij}\delta(\mathbf{r} - r'), \qquad (A.25)$$

For SH wave fields, similar to the scalar wave, the solution to equation A.25 is the zero order Hankel function and it spectrum is

$$G_{yy}(\mathbf{x}, k_s) = \frac{i}{2\mu_0\gamma_s}e^{i(\gamma_s x_s - k\hat{s}\cdot\mathbf{x})}.$$

For P-SV waves, the solution to equation A.25 is

$$\underset{\sim}{\mathbf{G}}(r, r') = \frac{i}{2\rho\omega^2}[\begin{vmatrix} \partial_x^2 & \partial_x\partial_z \\ \partial_x\partial_z & \partial_z^2 \end{vmatrix} H_0^{(1)}(k_\alpha|r - r'|) + \begin{vmatrix} \partial_z^2 & -\partial_x\partial_z \\ -\partial_x\partial_z & \partial_x^2 \end{vmatrix} H_0^{(1)}(k_\beta|r - r'|)].$$

and its spectrum maybe written as

$$\underset{\sim}{\mathbf{G}}(r, k_z) = \frac{i}{2\rho\omega^2}[\begin{vmatrix} (k_x^\alpha)^2 & k_x^\alpha k_z \\ k_x^\alpha k_z & k_z^2 \end{vmatrix} \frac{e^{i(k^\alpha x' - k_\alpha\hat{r}'\cdot r)}}{k_x^\alpha} + \begin{vmatrix} k_z^2 & -k_x^\alpha k_z \\ -k_x^\alpha k_z & (k_x^\beta)^2 \end{vmatrix} \frac{e^{i(k^\beta x' - k_\beta\hat{r}'\cdot r)}}{k_x^\beta}].$$

Appendix B

Pseudo-differential operators

Let $\mathcal{R}^n$ be the usual Euclidean space. On $\mathcal{R}^n$, the simplest differential operators are ∂_j or $D_j = -i\partial_j$. The most general linear partial differential operator of order m on $\mathcal{R}^n$ may be written as

$$\sum_{\alpha_1+\alpha_2+\ldots+\alpha_n \leq m} a_{\alpha_1,\alpha_2,\ldots,\alpha_n}(x) D_1^{\alpha_1} D_2^{\alpha_2} \ldots D_n^{\alpha_n}, \tag{B.1}$$

where $\alpha_1, \alpha_2, \ldots, \alpha_n$ are nonnegative integers and $a_{\alpha_1,\alpha_2,\ldots,\alpha_n}(x)$ is an infinitely differentiable complex-valued function on $\mathcal{R}^n$. To simplify the expression (B.1), we let

$$\alpha = (\alpha_1, \alpha_2, \ldots, \alpha_n),$$
$$|\alpha| = \sum_{j=1}^n \alpha_j,$$
$$D^\alpha = D_1^{\alpha_1} D_2^{\alpha_2} \ldots D_n^{\alpha_n},$$

and the differential operator (B.1) can be rewritten as

$$\sum_{|\alpha| \leq m} a_\alpha(x) D^\alpha. \tag{B.2}$$

For each fixed x in $\mathcal{R}^n$, the operator (B.2) is a polynomial in $D_1, D_2, \ldots, D_n$. Therefore it is natural to denote the operator (B.2) by $P(x, D)$. If D in (B.2) is replaced by a

152

point $\xi = (\xi_1, \xi_2, ..., \xi_n)$ in $\mathcal{R}^n$, then a polynomial

$$\sum_{|\alpha| \le m} a_\alpha(x) \xi^\alpha$$

is obtained, where $\xi^\alpha = \xi_1^{\alpha_1} \xi_2^{\alpha_2} ... \xi_n^{\alpha_n}$. This polynomial is denoted by $P(x, \xi)$ which is called the *symbol* of the operator $P(x, D)$. The partial differential operator $P(x, D)$ can be represented in terms of its symbol by means of the Fourier transform. Defining the Fourier transform operation as "$\wedge$" and the inverse Fourier transform operation as "$\vee$", one has

$$
\begin{aligned}
(P(x, D)\phi)(x) &= \sum_{|\alpha| \le m} a_\alpha(x)(D^\alpha \phi)(x) \\
&= \sum_{|\alpha| \le m} a_\alpha(x)\left(\widehat{D^\alpha \phi}\right)^\vee(x) \\
&= \sum_{|\alpha| \le m} a_\alpha(x)(\xi^\alpha \hat{\phi})^\vee(x) \\
&= \sum_{|\alpha| \le m} a_\alpha(x)(2\pi)^{-n/2} \int \xi^\alpha \hat{\phi}(\xi) e^{\iota x \cdot \xi} d\xi \\
&= (2\pi)^{-n/2} \int P(x, \xi)\hat{\phi}(\xi) e^{\iota x \cdot \xi} d\xi.
\end{aligned}
$$

This representation suggests that one can get operators more general than partial differential operators if the symbol $P(x, \xi)$ is replaced by more general symbols $\sigma(x, \xi)$ which are no longer polynomials in ξ. The operators so obtained are called pseudodifferential operators (Treves, 1980). Given such symbols, the oscillatory integral

$$P(x, D)\phi(x) =: \frac{1}{(2\pi)^n} \int d\xi p(x, \xi) e^{\iota x \xi} \hat{\phi}(\xi) \tag{B.3}$$

defines a map from smooth function of bounded support to smooth functions. i.e.. smooth operators yield small results when applied to oscillatory functions. Therefore the importance of pseudodifferential operators for the theory of wave imaging lies in their ability to describe the behavior of high frequency approximation.

Appendix C

Asymptotic Fourier transform

The Fourier transform takes the function $f(\mathbf{x}) = A(\mathbf{x})exp(i\Phi(\mathbf{x}))$. defined over $\mathbf{x}$, to the function $\hat{f}(\mathbf{k})$, defined over the dual space $\mathbf{k}$, i.e.,

$$\hat{f}(\mathbf{k}) = \mathcal{F}[f(\mathbf{x})] = c \int_{-\infty}^{\infty} A(\mathbf{x}) e^{i[\Phi(\mathbf{x}) - \mathbf{k} \cdot \mathbf{x}]} dx. \tag{C.1}$$

where $c = (1/2\pi)^{m/2}$ and m is the dimension. Assume that the phase. for a given $\mathbf{k}$. $[\Phi(\mathbf{x}) - \mathbf{k} \cdot \mathbf{x}]$ has an isolated non-degenerate stationary point $\mathbf{x}^s$. A point $\mathbf{x}^s$ is a stationary point of the function $\Phi(\mathbf{x}) - \mathbf{k} \cdot \mathbf{x}$ with respect to $\mathbf{x}$ if $\Phi_{,j}(\mathbf{x}^s) = k_j$ for a given $\mathbf{k}$. Expanding the phase about the point x^s,

$$\Phi(\mathbf{x}) - \mathbf{k} \cdot \mathbf{x} = \Phi(\mathbf{x}^s) - \mathbf{k} \cdot \mathbf{x}^s + \frac{1}{2}\Phi_{,ij}(\mathbf{x}^s)(x_i - x_i^s)(x_j - x_j^s). \tag{C.2}$$

Obviously only two terms have been retained. Performing a rotation and scale of the variable x_i to the variable y_i in the vicinity of $\mathbf{x}^s$, i.e., $\Phi_{,ij}(\mathbf{x}^s)(x_i - x_i^s)(x_j - x_j^s) = \gamma_i y_i^2$. where $\gamma_i = \pm 1$, one has

$$\Phi(\mathbf{x}) - \mathbf{k} \cdot \mathbf{x} = \Phi(\mathbf{x}^s) - \mathbf{k} \cdot \mathbf{x}^s + \frac{1}{2}\gamma_i y_i^2. \tag{C.3}$$

154

Consequently, the Fourier transform integral (C.1) may be approximated by

$$\hat{f}(\mathbf{k}) \approx A(\mathbf{x}^s)e^{i[\Phi(\mathbf{x}^s)-\mathbf{k}\cdot\mathbf{x}^s]}\int_{-\infty}^{\infty} e^{i\frac{1}{2}\gamma_i y_i^2}|J(\mathbf{x}^s, y)|dy. \tag{C.4}$$

where J is the Jacobian transformation between coordinates $\mathbf{x}$ and $\mathbf{y}$ in the vicinity of $\mathbf{x}^s$. Note that (C.4) represents a zero-order approximation of Parseval's theorem. When there are no stationary points within the support of A, (C.4) is asymptotically null. When there are several roots, each one contributes to an asymptotic expansion through the same process as when there is only one stationary point. This assumes the critical points are isolated. If any of the stationary points were "near" to one another, the above process would be inadequate and a uniform expansion would be necessary. After the remaining integral in (C.4) is evaluated, the asymptotic Fourier transform of $f(\mathbf{x})$ is obtained:

$$\hat{f(\mathbf{k})} \approx cA(\mathbf{x}_s)|J(\mathbf{x}^s, \mathbf{k})|e^{i[\Phi(\mathbf{x}^s)-\mathbf{k}\cdot\mathbf{x}^s]}e^{-iInd(\gamma_i)\pi/2}. \tag{C.5}$$

where the index $Ind(\gamma_i)$ is the number of negative γ_i, which describes whether the function $\Psi(\mathbf{k})$ has a local minimum or maximum (Ziolkowski, 1984). Physically, the ray may have touched a different number of caustics in the $\mathbf{x}$ and $\mathbf{k}$ domains and this information is contained in the index $Ind(\gamma)$. As the operator being applied to a function of the form $f(\mathbf{x}) = A(\mathbf{x})exp(i\Phi(\mathbf{x}))$ over $\mathbf{x}$ to the function $\hat{f}(\mathbf{k}) = B(\mathbf{k})exp(i\Psi(\mathbf{k}))$ over $\mathbf{k}$, its phase $\Psi(\mathbf{k})$ is defined by

$$\Psi(\mathbf{k}) = \Phi(\mathbf{x}^s) - \mathbf{k}\cdot\mathbf{x}^s, \tag{C.6}$$

which is the Legendre transformation (Maslov,1988), and the amplitude $B(\mathbf{k})$ is defined by

$$B(\mathbf{k}) = A(\mathbf{x}^s)|J(\mathbf{x}^s, \mathbf{k})|e^{-iInd(\gamma)\pi/2}. \tag{C.7}$$

In general, a wave and its Fourier transform are very different and there is no way to define wave as a function of both k and x. But asymptotically, real space and

Fourier space can be superimposed. An eikonal wave has a local Fourier transform that is supported on the Lagrangian submanifold. The Fourier transform of an eikonal wave is another eikonal wave whose phase function is the Legendre transform of the original phase function.

Bibliography

Aki, K., and Richards, P.G., 1980, Quantitative Seismology: Freeman and Company.

Backus, G.E. and Gilbert, J.F., 1968, The resolving power of gross earth data: Geophys. J. Roy. Astron. Soc., 16, 169–205.

Berryman, Jim, 1994, Tomographic resolution without singular value decomposition: Mathematical Methods in Geophysical Imaging II, Proc. SPIE, Volume 2301, pp. 2-13.

Beydoun, W.B. and Mendes, M., 1989, Elastic ray-Born migration/inversion: Geophysical Journal, 97, 151-160.

Beylkin, G., and Burridge, R., 1990, Linearized inverse scattering problems in acoustics and elasticity: Wave Motions, 12, p.15-52.

Born, Max and Wolf, Emil, 1970, Principles of optics; electromagnetic theory of propagation: 4th ed. Oxford, New York, Pergamon Press.

Bregman, N.D., Bailey, R.C. and Chapman, C.H., 1989a, Crosshole seismic tomography: Geophysics, 54, 200-215.

Bregman, N.D., Chapman, C.H. and Bailey, R.C., 1989b, Traveltime and amplitude analysis in seismic tomography: J. geophys. Res., 94, 7577-7587.

Burridge, Robert, 1976, Some mathematical topics in seismology: New York: Courant Institute of Mathematical Sciences, New York University

Cerveny, V., Klimes, L. and Psencik, I., 1984, Paraxial ray approximation in computation of seismic wavefields in inhomogeneous media: Geophysical Journal of the Royal astr. Soc., 79, 89-104.

Chernov, Lev Aleksandrovich, 1960, Wave Propagation in a Random Medium: New York, McGraw-Hill.

Chew, Weng Cho, 1990, Waves and fields in inhomogeneous media: New York, Van

Nostrand Reinhold

Colton, David L., 1983, Integral equation methods in scattering theory: New York, Wiley

Claerbout, J. F., 1985, Imaging the earth's interior: Blackwell Scientific Publications.

Devaney, A. J., 1982, A filtered backpropagation algorithm for diffraction tomography: Ultrasonic Imaging, vol 4, pp 336-360

Devaney, A. J., 1984, Geophysical diffraction tomography: IEEE Trans. Geosci. Remote Sensing GE-22, 3-13

Devaney, A.J., 1989, The limited-view problem in diffraction tomography: Inverse Problems, vol.5, no.4, p. 501-21.

Devaney, A. J., Zhong, D., 1991, Geophysical diffraction tomography in a layered background: Wave Motion, 14, 243-265

Devaney, A.J., 1987, Inverse scattering; theory and applications: International symposium digest: antennas and propagation.

Deutsch, Clayton V., Journel G. Andre, 1992, Geostatistical software library and user's guide: New York: Oxford: Oxford University Press.

Dickens, T. A., 1994, Study of diffraction tomography for layered backgrounds: Geophysics, 59, 694-706.

Dines, K.A. and Lytle, R.J., 1979, Computerized geophysical tomography: Proc. Inst. Electr. Electron. Eng., 67, 471-480.

Eisler, T. J., R. New and D. Calderone, 1982, Resolution and Variance in Acoustic Tomography: J. Acoust. Soc. Am., vol. 72, pp. 1965-1977.

Farra, V., 1989, Ray perturbation theory for heterogeneous hexagonal anisotropic media: Geophs. J. Int., 99, 377-390.

Gazdag, J. and Sguazzero, P., 1984, Migration of seismic data: Proceedings of the IEEE, 72:1302-1315.

Habashy, T.M., et al., 1992, Beyond the Born and Rytov approximations: a nonlinear approach to electromagnetic scattering: Journal of Geophysical research, vol.98, no.B2, p. 1759-75.

Harris, J. M., Nolen-Hoeksema, R. C., Rector, J. W., Lazaratos, S. K. and Van Schaack, M. A., 1995, High-resolution crosswell imaging of a west Texas carbonate reservoir: Part 1 Project summary and interpretation: Geophysics, 60, 667-681.

Harris, J. M., 1987, Diffraction tomography imaging with arrays of source and detectors: IEEE Trans. Geoscience Remote Sensing, vol. Ge-25, No. 4, 448-455.

Harris, J. M., 1993, Spatial bandwidth limitations of seismic geotomography: STP report, Stanford University.

Harris, J. M. and Wang, G. Y., 1996, Diffraction tomography for inhomogeneities in layered background medium: Geophysics, 61, 570-583.

Hoenders, B. J., The uniqueness of inverse problems: in Inverse problems in optics, edited by Baltes, H. P., Spinger-Verlag, New York, 1978.

Huan, L., Wu, R., 1992, Multifrequency backscattering tomography: Extension to the case of vertical varying background: 62nd Ann. Internat. Mtg., Soc. Expl. Geophys., Expanded Abstract, 766-769

Ikelle, L.T. and Yung, S.K., 1993, 2D random media with ellipsoidal autocorrelation functions: Geophysics vol.58, no.9, p. 1359-72.

Ishimaru, A. 1978, Wave propagation and scattering in random media: Academic Press New York.

Kak, A.C., and Slaney, M., 1988, Principles of Computerized Tomographic Imaging: IEEE Press, New York.

Keller, J. B., 1958, Corrected Bohr-Sommerfeld quantum conditions for non-separable systems: Ann. Physics 4, p.180-188.

Keller, J. B., 1962, Geometrical theory of diffraction: J. Opt. Soc. Am. 52(2), p.116-130.

Kendall, J. M. and Thomson, C. J., 1993, Maslov ray summation, pseudo-caustics, Lagrangian equivalence and transient seismic waveforms: Geophysical Journal International vol.113, no.1, p.186-214.

Kravtsov, Y. A. and Orlov, Yu. I., 1990, Geometrical optics of inhomogeneous media: Berlin; Springer-Verlag.

Kravtsov, Y. A. and Orlov, Yu. I., 1993, Caustics, catastrophes and wave field: Berlin; Springer-Verlag.

Lazaratos, S. K., 1993, Crosswell reflection imaging: Ph.D. thesis, Stanford University

Lumley, David, 1996, Seismic time-lapse monitoring of subsurface fluid flow: Ph.D. thesis, Stanford University

Maslov, V. P P., 1988, Asymptotics of operator and pseudo-differential equations:

Consultants Bureau.

Miller, D. E. Oristaglio. M. and Beylkin, G. 1987, A new slant on seismic imaging: Migration and integral geometry: Geophysics, 52, 943-964.

Miller, J. C., 1986, Hamiltonian perturbation theory for acoustic rays in a range dependent sound channel: J. Acoust. Soc. Am., vol. 79, pp. 338-346.

Mueller, R. K. et al., 1979, Reconstructive tomography and applications to ultrasonics: Proc. IEEE, vol 76. no. 4

Muller, G., et al., 1992, Seismic-wave traveltimes in random media: Geophysical Journal International vol.110, no.1, p. 29-41.

Mukerji, Tapan, 1995, Waves and scales in heterogeneous rocks: Ph.D. thesis. Stanford University

Pai, D. M., 1990, Crosshole seismics using vertical eigenstates: Geophysics, 55, 815-820.

Papoulis,A., 1984. Probability, random variables, and stochastic process: 2nd ed. New York: McGraw-Hill.

Pratt, R. G. 1989, Combining wave equation imaging with travltime tomography to form high resolution images from crosshole data: Geophysics. 56. 208-224.

Rayleigh, J. W. S., 1917, On the reflection of light from a regularly stratified medium: The collected optics papers of Lord Rayleigh, part B, Optical Society of America.

Rytov, S. M., Kravtsov, Y. A. and Tatarskii, V. I. 1987, Principles of statistical radiophysics: Springer, New York.

Shapiro,, S. A. and Kneib, G. 1993, Seismic attenuation by scattering: theory and numerical results: Geophy. J. Int. 114, 373-391.

Song, Z. M., Williamson, P. R. and Pratt, R. G., 1995, Frequency-domain acoustic-wave modeling and inversion of crosshole data, Part II: inversion method. synthetic experiments and real-data results: Geophysics, 60, 796-809.

Tarantola, A., 1984, Inversion of seismic reflection data in the acoustic approximation: Geophysics, 49, 1259-1266.

Thompson, D.R, Rodi, W. and Toksoz, M.N., 1994, Nonlinear seismic diffraction tomography using minimum structure constraints: Journal of the Acoustical Society of America (Jan. 1994) vol.95, no.1, p. 324-30.

Treves. F. 1980, Introduction to pseudodifferential and Fourier integral operators:

Plenum, New York.

Vainberg B. R., 1988, Asymptotic methods in equations of mathematical physics: Gordon and Breach science publishers.

Wang, Guan, 1995, Diffraction tomography of strongly scattering medium Part I: using phase extrapolation: STP report, Stanford University.

Williamson, P.R., 1993a, Anisotropic crosshole tomography in layered media. Part I: Introduction and methods: Journal of Seismic Exploration. 2, 107-121.

Williamson, P.R., 1993b, Anisotropic crosshole tomography in layered media. Part II: Applications, results and conclusions: Journal of Seismic Exploration. 2. 223-238.

Woodward, M.J., 1992, Wave equation tomography: Geophysics. 57. 15-26.

Wolf, Emil, 1969, Three-dimensional structure determination of semitransparent object from holographic data: Optics Comm., 1, 153.

Wu, R. S. and Toksoz, M. N., 1987, Diffraction tomography and multi-source holography applied to seismic imaging: Geophysics 52, 11-25.

Ziolkowski, R. W., 1984, Asymptotic evaluation of high-frequency fields near a caustic: An introduction to Maslov's method: Radio Science, vol. 19, 4 p.1001-1025.